Low-frequency noise in narrow- and wide-gap III-V compound semiconductor devices

by

Le Phuong Son

submitted to
Japan Advanced Institute of Science and Technology
in partial fulfilment of the requirements
for degree of
Doctor of Philosophy

Supervisor: Professor Toshi-kazu SUZUKI, Ph.D.

School of Materials Science
Japan Advanced Institute of Science and Technology

September, 2014

Abstract

III-V compound semiconductors, which have many advantages over silicon, are important materials for electronic and optical devices. For example, InAs, which has a narrow energy gap E_g and a very high electron mobility μ, is a potential material for high-speed device applications. In contrast to InAs, GaN, which has a wide E_g and a moderate μ, is a promising material for high-power device applications. Although III-V compound semiconductor devices have been studied for a long time, their low-frequency noise (LFN) characterization still remains many issues.

In this work, we fabricated two-terminal (2T) devices from InAs films obtained by separation-bonding method on low dielectric constant flexible substrates (low-k FS) (InAs/FS) or by direct growth on GaAs(001) (InAs/GaAs). In addition, from $Al_{0.27}Ga_{0.73}N$/GaN heterostructures, we fabricated GaN devices, ungated 2T devices as well as heterojunction field-effect transistors (HFETs), with Schottky structures and metal-insulator-semiconductor (MIS) structures in which an AlN insulator was sputtering-deposited on the AlGaN. Before the AlN deposition, two types of the AlGaN surface treatment were used with and without a cleaning by Semicoclean (an ammonium-based solution, ABS). Using these devices, LFN in InAs and GaN devices were systematically investigated by using a measurement system established in our laboratory.

The InAs and GaN devices show low-frequency current noise spectra, exhibiting that the noise power spectrum density S_I satisfies $S_I/I^2 \simeq K/f$ with the current I and a constant factor K depending on the device characteristics. The InAs devices exhibit $K \propto 1/LW$, where L and W are device length and width, indicating a negligible contribution of the electrode contacts. The Hooge parameter defined as $\alpha = KN = Kn_sLW$, where n_s is conducting channel sheet electron concentration, is inversely proportional to μn_s. For InAs/FS with thickness $d \gtrsim 20$ nm, where μ weakly changes, $\alpha \propto {n_s}^{-1}$ is observed and attributed to the electron-number fluctuation $(\delta N)^2 \sim LWD_i k_B T$, where the interface state density $D_i \sim 10^{12}$ cm^{-2}eV^{-1} is obtained from the data, being consistent with the Coulomb-scattering mobility. For InAs/FS with $d \lesssim 20$ nm and InAs/GaAs(001), where n_s weakly changes, $\alpha \propto \mu^{-1}$ is observed, which can be related to the mobility fluctuation due to fluctuations in the InAs film thickness.

The ungated 2T GaN devices show $K \simeq$ constant for small L, indicating a significant contribution of the electrode contacts. Using resistance-in-series model, we obtained $K_cW \simeq 1.9 \times 10^{-12}$ cm for one contact, which is common for the MIS and Schottky devices because of the same Ohmic process, and a Hooge parameter of the ungated region $\alpha_{ug} \simeq 2.2 \times 10^{-4}$, 4.1×10^{-4}, and 5.0×10^{-4} for the MIS devices with cleaning by ABS (w ABS), MIS devices w/o ABS, and Schottky devices, respectively. The smaller α_{ug} in the MIS devices can be attributed to the lower electron mobility due to additional scattering mechanisms caused by the AlN insulator deposition, where the mobility fluctuation dominates α_{ug} according to the Hooge theory. From the ungated-device characterization, LFN behavior in the intrinsic gated region was extracted for the HFETs. For the MIS-HFETs with the small $n_s \lesssim 5 \times 10^{11}$ cm^{-2}, $\alpha \propto {n_s}^{-1}$, also observed for Schottky-HFETs with $n_s \lesssim 10^{12}$ cm^{-2}, and is attributed to the carrier-number fluctuation due to

electron traps with density $D_0 \sim 10^{11}$ cm^{-2}eV^{-1} in the AlGaN. On the other hand, for 5×10^{11} cm^{-2} $\lesssim n_{\rm s} \lesssim 1\times10^{12}$ cm^{-2}, the MIS-HFETs show $\alpha \propto {n_{\rm s}}^{-\xi}$ with $\xi \sim$ 2-3, which is not observed for Schottky-HFETs, and tentatively attributed to the mobility fluctuation specific for the MIS-HFETs. Moreover, $\alpha \propto {n_{\rm s}}^3$ for both MIS- and Schottky-HFETs with $n_{\rm s} \gtrsim 2 \times 10^{12}$ cm^{-2}, can be attributed to the fluctuation in the intrinsic gate voltage, which is enhanced for large gate voltage and large $n_{\rm s}$ by the fluctuation of the voltage across the extrinsic source resistance.

In summary, LFN in narrow- and wide-gap III-V compound semiconductors were systematically investigated for InAs (narrow-gap) and GaN (wide-gap) devices. We clarified detailed behaviors of the Hooge parameter depending on the devices.

Keywords

III-V compound semiconductors, InAs, AlGaN/GaN, low-frequency noise, Hooge parameter.

Acknowledgments

I would like to express my sincere gratitude to Professor Toshi-kazu Suzuki, whose patience and talent made me become better day after day. Suzuki sensei is the person who makes me believe that there always exist great people even I may meet many sorrowful things in my life.

I also would like to acknowledge Professor Hiroshi Mizuta for his instruction in sub-theme research, Professor Shyoji Yamada and Associate Professor Masashi Akabori for their support during my course.

I would like to be grateful of my friends, especially Suzuki laboratory members, for their support and encouragement, their kindness and friendship helped me overcome difficulties in my abroad life to live better.

I would like to thank Japan Advanced Institute of Science and Technology (JAIST) for a scholarship and useful supports during my course.

Finally, and most deeply, I would like to express my deep gratitude to my family members, in particular my wife with her great love, who not only give me the life meaning, but also are always beside me in any situations.

Contents

Chapter 1

Introduction

1.1 More than Moore (MtM)

In spite of a short history: the first study on 1874, the first device in laboratory on 1947, and the first commercial product in 1960s; semiconductors have made the human history have a huge leap, maybe the greatest evolution in its whole history! Electronic products, in which semiconductors play the most important role, became indispensable for the mankind, from scientific works to daily life. Semiconductors are becoming more important day after day with a big contribution, which is continuously increasing, to the world total product as shown in Fig. 1.1. We note that the semiconductor industry, a subset of the electronic industry, is growing at the highest rate and seems to surpass other industries such as automobiles or steel to become the most important industry of the world! Moreover, semiconductors are important pioneers in the advanced technologies, that are necessary for not only the industries but also scientific works, opening up new frontiers for the mankind. No science, no life. No semiconductors, no advanced science!

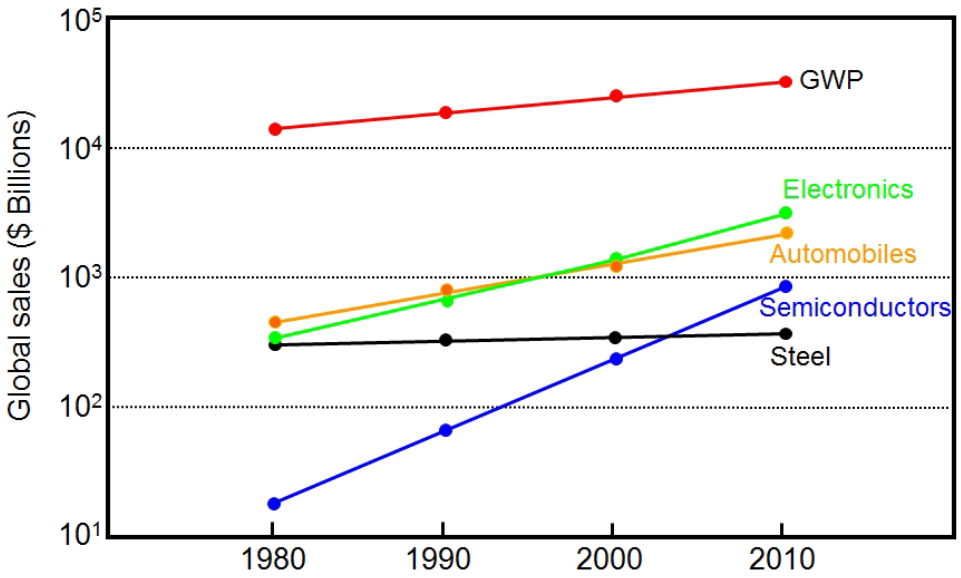

Figure 1.1: Gross world product (GWP) for some years with contribution from main industries [1].

In order to get such important roles, semiconductors have been having a dramatically quick development in both scientific researches and industrial applications. The Moore's law, which has been proven to be accurate, stated that: "Over the history of computing hardware, the number of transistors on integrated circuits doubles approximately every two years" [2]. Figure 1.2 shows the evolution of the density and minimum feature size of transistors, the main component of an electronic device, from the time of the first integrated circuit to recent years. We realize that the minimum feature size of the transistor is being continuously scaled down and will reach to order of 20 nm in near future.

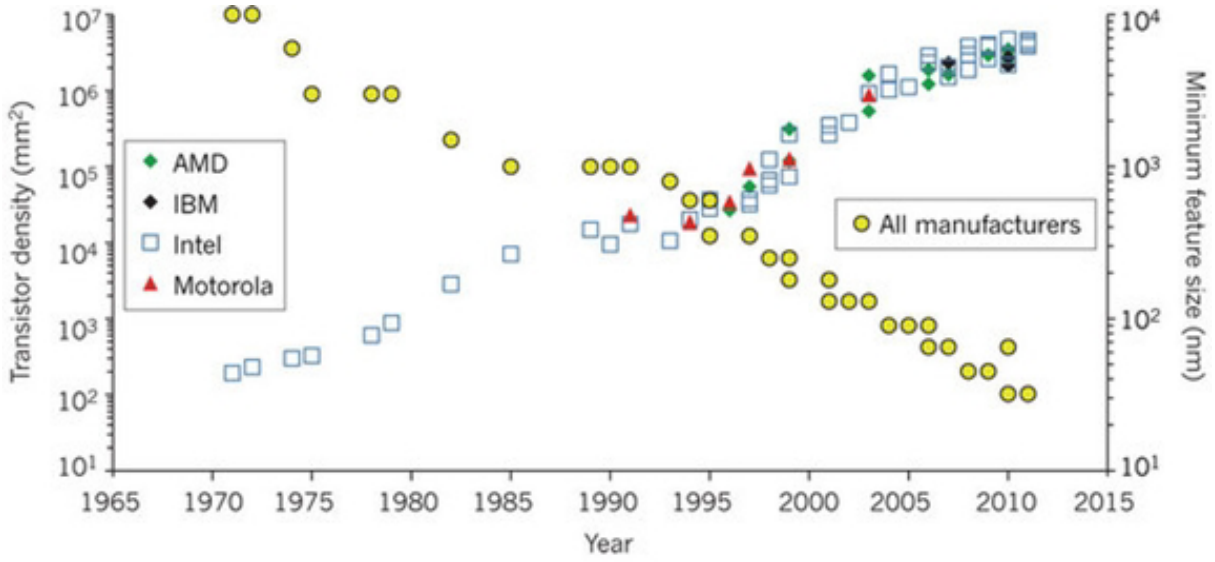

Figure 1.2: The evolution of the transistor density and minimun feature size [3].

However, the decrease of device size will lead to many problematic issues such as limits of bias voltages, effects of short conduction channels and etc... These problems are inherent in the device size scaling down and will harmfully affect the device performances. Hence, there exists a critical domain for the semiconductor devices whose developments are being based on the Complementary Metal-Oxide-Semiconductor (CMOS) technology. But the human evolution cannot stop! We have to find out new materials and technologies to go beyond CMOS and/or to go to other trenchs independent of the Moore's law.

Figure 1.3 shows two present main development tendencies for the semiconductor devices: More-Moore Miniaturization and More-than-Moore (MtM) Diversification. The first, which obeys the Moore's law, is More-Moore or Miniaturization: The decrease of physical feature sizes of the digital components such as transistors increases the device density, improving the performances. The second, which does not obey the Moore's law, is More-than-Moore or Diversification: The integration of new functions into devices, which does not need the scaling-down of the feature sizes, increases the device functionalities, improving the performances. For comparison, the More-Moore approach means that the device density increase leads to the device performance improvement (for that purpose, people try to reduce the device feature size - progresses made by the miniaturization), while the MtM approach means that the new values added to the final products make the device performance development (for that purpose, people try to add new functions to the device - progresses made by the functional diversification).

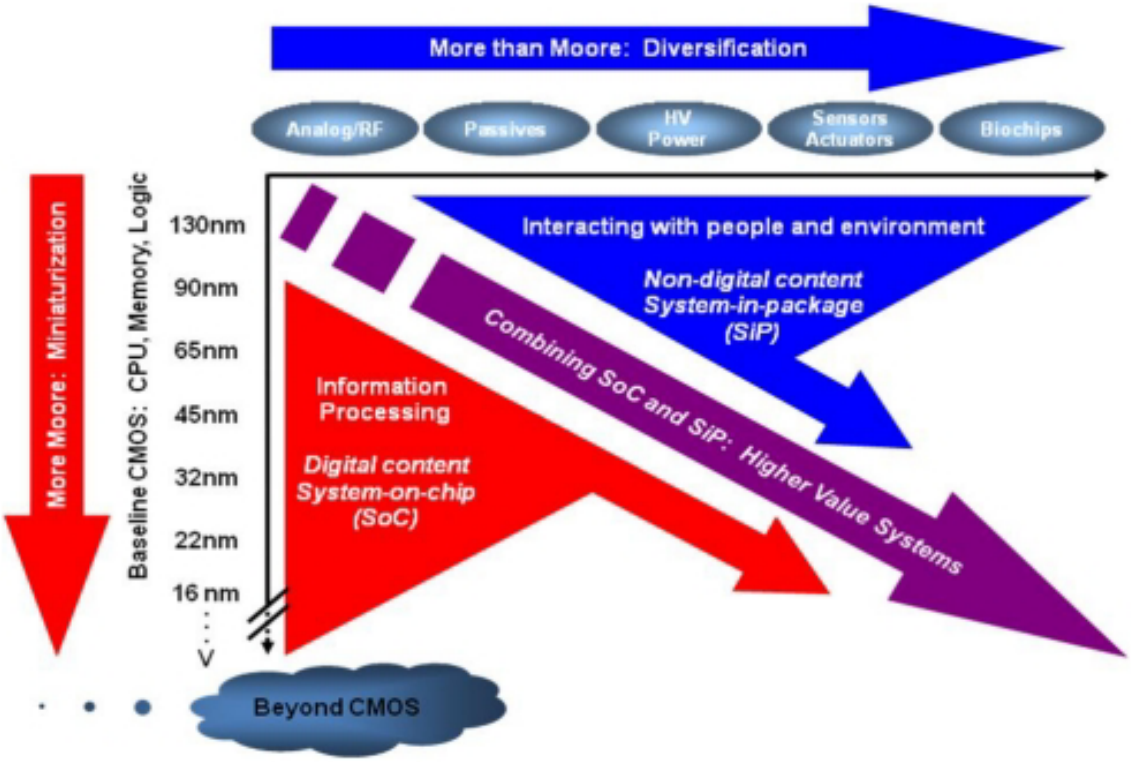

Figure 1.3: More Moore and More-than-Moore [4].

At the present time, the technologies for both these tendencies are simultaneously developed, and those for the More-Moore Miniaturization are playing the main role. However, developments according to the More-Moore will reach to the ultimate limitation due to the requirements of device physical properties, which will meet the troubles in ultra-small scale, e.g., short-channel effects in field-effect transistors (the key component of the CMOS technologies). As a result, developments according to MtM functional diversification will become more favorable.

The More-Moore technologies develop the digital contents such as logic and memory. On the other hand, the MtM technologies improve the non-digital contents such as analog/RF and power. The MtM technologies will lead the device developments from the digital contents to the nondigital contents, from the system board level into the package (System-in-Package, SiP) to that onto the chip (System-on-Chip, SoC), and from the information processing to the interacting with people and environment. Therefore, the MtM technologies cover a wide range of fields due to their advantages of various functionalities. For example, the MtM technologies present in microelectromechanical systems (MEMS) applications (sensors, actuators,...), radio frequency CMOS applications (Bluetooth, GPS and Wi-Fi,...), CMOS image sensors in digital cameras, high voltage drivers for power LED lights, and so on. These applications add new values to computing and memory devices made by the More-Moore technologies. Due to the increasing importance of the MtM technologies, the electronic semiconductor industry circle should be reconsidered. The virtuous circle, which makes the successes of the digital electronic industry, should be extended to include the contribution of MtM technologies, as shown in Fig. 1.4.

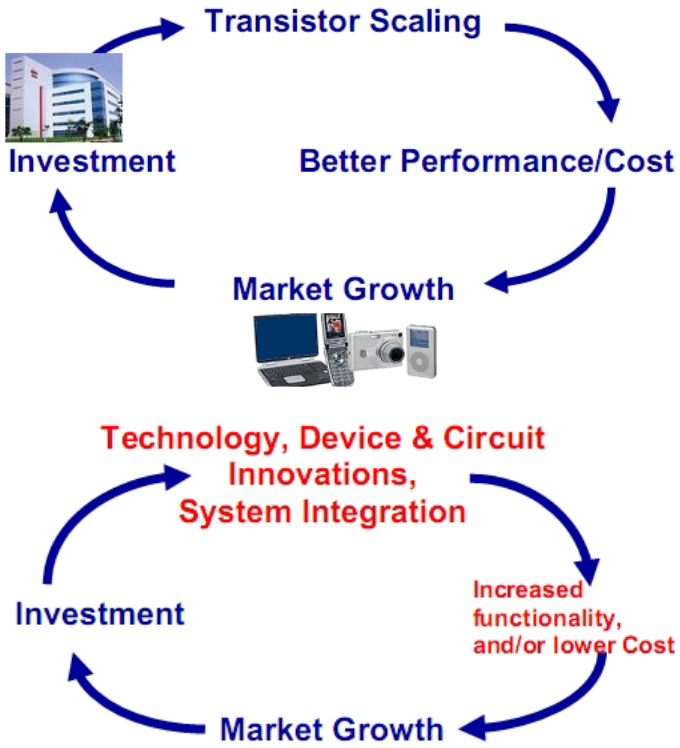

Figure 1.4: The virtuous circle of the semiconductor industry with only More Moore miniaturization (above) and with including More-than-Moore diversification (below) [5].

1.2 Compound semiconductors for More than Moore

In order to achieve the More-than-Moore functional diversification, compound semiconductors, which have many advantageous properties over silicon (the conventional semiconductor) such as direct band gaps and others shown in Table 1.1, should be employed. Compound semiconductors have been applied to the high-speed devices and the optical devices that cannot be achieved with the Si due to their advantageous properties such as high electron mobility and direct energy band structure. For example, Metal-Semiconductor Field-Effect-Transistors (MES-FETs) [6], High Electron Mobility Transistors (HEMTs) [7], Heterojunction Bipolar Transistors (HBTs) [8], Light Emitting Diodes (LEDs) and Laser Diodes (LDs) [9–11], and heterostructure lasers [12], etc... have been realized by using the compound semiconductors, exhibiting many advanced performances.

Parameter	Si	GaAs	$In_{0.53}Ga_{0.47}As$	InAs	GaN
Energy gap [eV]	1.12	1.42	0.72	0.35	3.39
Wavelength [μm]	1.1	0.9	1.7	3.4	0.36
Electron effective mass m_n^*/m_0	0.98^l,0.19^t	0.063	0.041	0.023	0.22
Electron mobility [cm^2/V.s]	600	4600	7800	16000	1350
Electron peak velocity [10^7cm/s]	1.0	2.2	2.7	4.0	2.7
Breakdown field [10^5 V/cm]	3	4	2	0.4	30

Table 1.1: Some main properties of typical semiconductors.

The Table 1.1 shows some basic properties of some typical semiconductors, in which we can realize the advantages of III-V compounds over the silicon. Due to the application purpose, which properties should be favored.

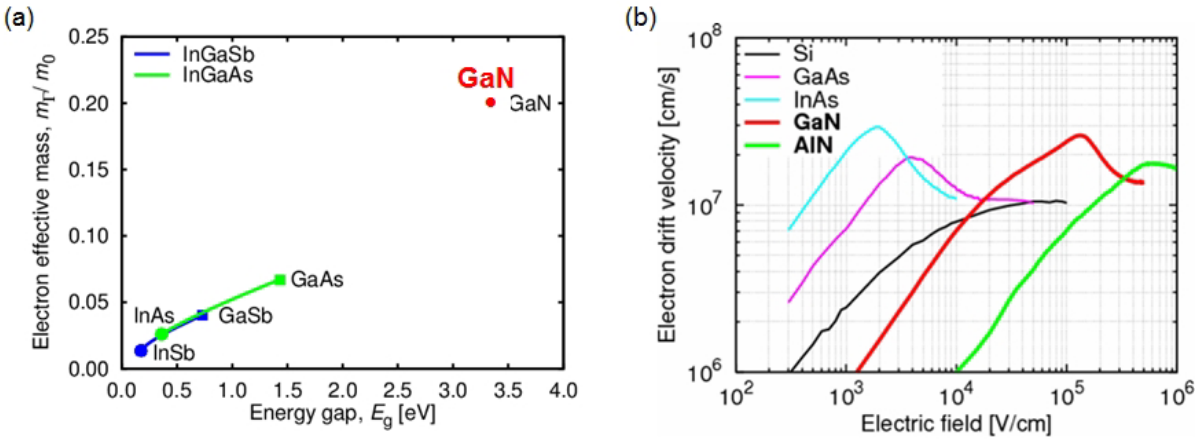

Figure 1.5: (a) The effective mass ratio m_Γ/m_0 as a function of the energy gap, and (b) the electron drift velocity as functions of the electric field for some compound semiconductors.

Figure 1.5 shows the electron effective mass ratio m_Γ/m_0 as a function of the energy gap E_g, and the electron drift velocity as functions of the electric field for some compound semiconductors. We realize that the narrow gap compound semiconductors (NGCS) such as InAs have a small effective mass m^*, leading to a high electron mobility μ because

$$\mu = \frac{e\tau}{m^*}, \tag{1.1}$$

and a high electron saturation velocity $v_{\rm sat}$ due to

$$v_{\rm sat} = \sqrt{\frac{\hbar\omega_{\rm op}}{m^*}}, \tag{1.2}$$

where τ and $\omega_{\rm op}$ are the momentum relaxation time and optical phonon energy. Hence the NGCS can be used for high-speed device applications. In contrast, the wide gap compound semiconductors (WGCS) such as GaN have a large effective mass m^*, leading to not a high electron mobility, but they have a high breakdown field $E_{\rm b}$, which is usually related to the energy gap by

$$E_{\rm b} = {E_{\rm g}}^n, \ n \simeq 1-3, \tag{1.3}$$

where $E_{\rm g}$ is energy gap. Therefore the WGCS can be used for high-power, high-frequency device applications. However, there exists a proportion between the electron effective mass and the energy gap,

$$m^* \propto E_{\rm g}, \tag{1.4}$$

the high electron mobility and the large energy gap are difficult to be obtained simultaneously. Hence, we can realize that there is a trade-off between the high-speed and high-power in general, it seems impossible to satisfy both these requirements simultaneously. Therefore, both NGCS and WGCS are important for future device applications,

and which should be employed depending on the application purpose. Figure 1.6 show the energy gap E_g in relation to the lattice constant a, from which we can realize the tendency of an inverse proportion

$$E_g \propto \frac{1}{a}. \tag{1.5}$$

Equation 1.5 is important for heterogeneous integration, which will be discussed in next paragraph, where the lattice-match between the substrate and the grown device layer will decide the material quality, and also properties.

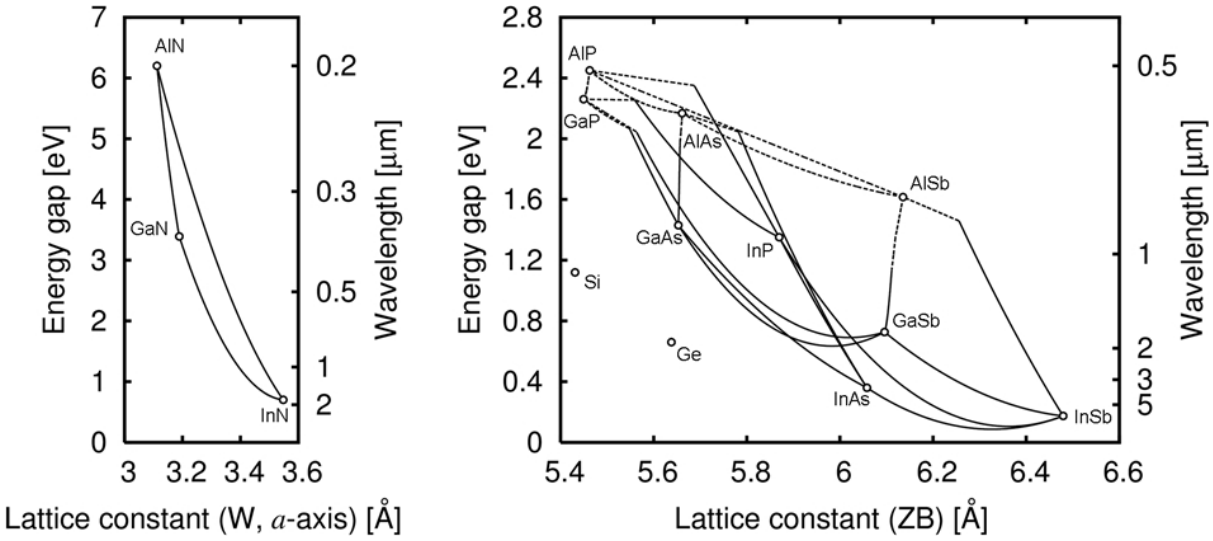

Figure 1.6: The energy gap and corresponding wavelength as functions of the lattice constant for some III-V compound semiconductors [13, 14].

To obtain compound semiconductors devices, heterogeneous integration is important. Various devices can be realized by various materials integrated on any foreign host substrate, as shown in Fig. 1.7, for example, compound semiconductor electronic devices integrated on Si-platform, electronic and optical integrated circuits on Si-platform, integrated circuits on plastic, ceramic or low-k flexible substrates (FS) and so on. The heterogeneous integration can be achieved by two main approaches: direct growth method by which the device materials are directly grown on substrates, and separation-bonding method by which the device materials are firstly grown on a substrate, then separated, e.g., by epitaxial lift-off [15], and bonded on any foreign substrates. The schematic of heterogeneous integration methods is shown in Fig. 1.8(b). As we can easily realize, the heterogeneous integration can give various choices for the materials, but it also induces non-ideal interfaces between the device semiconductor layer and the substrate due to the dissimilarities in used materials. One of most serious issues is the difference in lattice constants, which can induce serious defects not only at the interface but also in the grown device layers. Hence the first method, direct growth, is suitable for lattice-matched or small lattice-mismatched (LMM) systems such as InGaAs on GaAs or AlGaN on GaN, while the second method, separation-bonding, is suitable for large LMM systems such as InAs-based ones. According to the formation method, there exists a trade-off between the accessibility and the device layer quality, due to the dissimilarities between the device

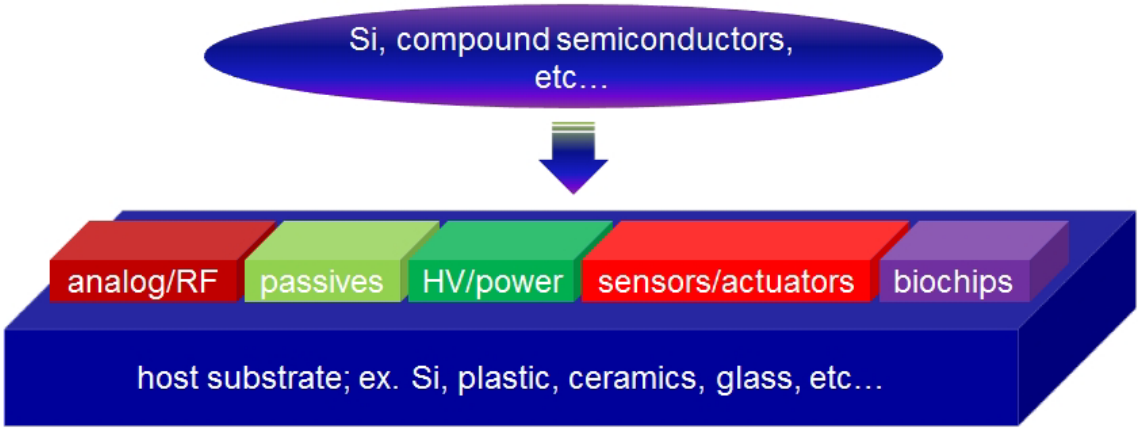

Figure 1.7: Functional diversification achieved by integration of different material devices on dissimilar material host-substrates.

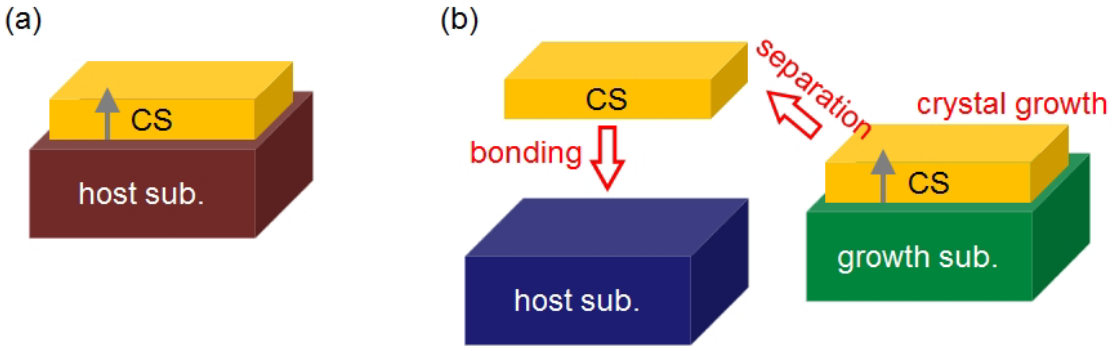

Figure 1.8: Schematic of heterogeneous integration methods: (a) Direct growth: the CS is directly grown on the host substrates. (b) Separation and bonding: the CS is firstly grown on substrates, then separated from the grown substrates and finally bonded on the host substrates.

material and the substrate. By considering to the demands of the applications, which should be favored, the accessibility or the material quality. The heterogeneous integration is hence a promising technology to realize the compound semiconductors. However, the heterointerfaces between the device layer and the substrate are always in concern because the interfaces give significant influence on the device performances. In particular, the device noise characteristics are strongly influenced by the semiconductor materials themselves, and also their interfaces through interface states. The interface states can trap/detrap electrons, leading to fluctuation in the carrier-number and also the mobility. These fluctuations give the noise to the signals (current or voltage) in the devices. Because the noise is an important parameter for the device operation, e.g., setting a lower limit for the device meaningful signals, the noise characteristics should be extensively studied to obtain deep insights into the device physics and improve the device performances.

1.3 Low-frequency noise in semiconductor devices

1.3.1 Noise, low-frequency noise, and $1/f$ noise

Noise is the fluctuations of a quantity around its mean value. In science and engineering, noise is a fundamental problem, which should be carefully considered, because the noise directly affects the device/instrument performances by limiting the measurement accuracy and the magnitude of detectable signals. The signal-to-noise ratio (SNR) is an important factor for any electronic devices and circuits used for signal processing, the lower SNR is desired for the higher reliability. In an electronic circuit, currents and voltages are not ideally constant, but randomly fluctuate around the mean values due to fluctuations in the physical processes governing the carrier transport. These fluctuations give the noise, being inherent in the device physics: The voltage/current applied to the devices does not fluctuate, but the voltage/current in the devices fluctuates due to fluctuations in the device physical processes, giving voltage/current noise. True noise in an electronic device/circuit differs from external disturbances (see Appendix A): The disturbance can be completely removed by a good measurement system setting, while the noise can only reduced partially (but not totally) by prober device/circuit designs.

Noise is a random process, and usually determined by the power spectral density (PSD) $S(f)$ as a function of frequency f. A physical quantity x cannot be ideally constant, but usually a function of time t with fluctuations around its mean value, $x(t) = \langle x \rangle + \delta x(t)$. The fluctuation of the quantity x is hence defined as

$$[\delta x(t)]^2 = \langle (x - \langle x \rangle)^2 \rangle = \langle x^2 \rangle - \langle x \rangle^2, \tag{1.6}$$

where $\langle x \rangle$ is averaging of $x = x(t)$. The fluctuation given by Eq. (1.6) is in time domain, and will be converted to the frequency domain by a Fourier transformation. According to the Wiener-Khintchine theorem, the PSD of the quantity x, which is defined as fluctuation in a unit bandwidth of frequency, is given by [16]

$$S_x(f) = 2 \int_{-\infty}^{+\infty} \mathrm{d}(t_1 - t_2) e^{j\omega(t_1 - t_2)} \psi_x(t_1 - t_2), \tag{1.7}$$

here, $\psi_x(t_1 - t_2)$ is the correlation function determined by

$$\begin{aligned} \psi_x(t_1 - t_2) &= \langle \delta x(t_1) \delta x(t_2) \rangle = \lim_{N \to \infty} \frac{1}{N} \sum_{i=1}^{N} \delta x_i(t_1) \delta x_i(t_2), \\ &= \overline{\delta x(t_1) \delta x(t_2)} = \lim_{t_m \to \infty} \frac{1}{t_m} \int_{-t_m/2}^{+t_m/2} \mathrm{d}t \delta x(t_1 + t) \delta x(t_2 + t), \end{aligned} \tag{1.8}$$

where x can be the resistance R, current I, or voltage V, etc... In the Eq. (1.8), we used the argodic assumption, which states that the number averaging gives the same result as the time averaging. If we chose $t_1 = t,\ t_2 = 0,$ and $\omega = 2\pi f$, the PSD and the correlation function become

$$S_x(f) = 2 \int_{-\infty}^{+\infty} \psi_x(t) e^{2j\pi f t} \mathrm{d}t, \tag{1.9}$$

$$\psi_x(t) = \langle \delta x(0) \delta x(t) \rangle. \tag{1.10}$$

We will consider the properties of the PSD and the correlation function as follows. First, the correlation function is an even function, because we can rewrite the later equation of Eq. (1.8) as

$$\psi_x(t) = \frac{1}{2T}\int_{-T}^{+T} \delta x(\tau)\delta x(\tau+t)\mathrm{d}\tau, \text{ then} \tag{1.11}$$

$$\begin{aligned}
\psi_x(-t) &= \frac{1}{2T}\int_{-T}^{+T} \delta x(\tau)\delta x(\tau-t)\mathrm{d}\tau & (1.12)\\
&= \frac{1}{2T}\int_{-T}^{+T} \delta x(s+t)\delta x(s)\mathrm{d}s, \text{ by setting } \tau - t = s & (1.13)\\
&= \psi_x(t). & (1.14)
\end{aligned}$$

Second, even though the negative frequency is not available (a meaningless concept), $S_x(-f)$ is formally defined by Eq. (1.9), as a result, $S_x(f)$ is also an even function, since

$$\begin{aligned}
S_x(-f) &= 2\int_{-\infty}^{+\infty} \psi_x(t)e^{-2j\pi ft}\mathrm{d}t & (1.15)\\
&= -2\int_{+\infty}^{-\infty} \psi_x(-s)e^{2j\pi fs}\mathrm{d}s, \text{ by setting } -t = s & (1.16)\\
&= 2\int_{-\infty}^{+\infty} \psi_x(s)e^{2j\pi fs}\mathrm{d}s, \text{ since an even function } \psi_x(t) & (1.17)\\
&= S_x(f). & (1.18)
\end{aligned}$$

Third, the Fourier transformation of Eq. (1.9) will give the correlation function

$$\begin{aligned}
\psi_x(t) &= \frac{1}{2}\int_{-\infty}^{+\infty} S_x(f)e^{-2j\pi ft}\mathrm{d}f & (1.19)\\
&= \int_{0}^{+\infty} S_x(f)e^{-2j\pi ft}\mathrm{d}f, \text{ and} & (1.20)
\end{aligned}$$

$$\begin{aligned}
\psi_x(0) &= \int_{0}^{+\infty} S_x(f)\mathrm{d}f & (1.21)\\
&= \langle[\delta x(0)]^2\rangle = (\delta x)^2, & (1.22)
\end{aligned}$$

where $(\delta x)^2$ is considered as the observable fluctuation, which can be experimentally obtained through measurements of the fluctuation (or noise) spectrum density $S_x(f)$.

Due to the dependence of PSD on the frequency f, noise can be classified as (1) thermal noise whose PSD is independent of f (in other words, Nyquist, Johnson, or white noise) caused by thermal motion of carriers; (2) shot noise caused by the discrete nature of carriers; (3) generation-recombination (g-r) noise whose PSD depending on f by a Lorentzian function, caused by capture and emission of traps; (4) $1/f$ noise whose PSD is inversely proportional to the frequency, and etc... The low-frequency noise is the noise at low frequencies, meaning time-domain fluctuations with long time averaging. There is no above limit of the low-frequency domain, however, the experimental above limit is

usually up to 10 kHz, or less, the frequencies below this limit are consider "low". Owing to a domination of g-r noise and $1/f$ noise (increasing while others unchanged with a decrease in f) at the low frequencies, these two noise sources play the most important roles in the noise consideration of devices/circuits. In particular, the $1/f$ noise is always to increase with a a decrease in frequency, then will become the most important noise source at very low frequencies. Hence, the terminology "low-frequency noise" is usually understood to indicate the $1/f$ noise. $1/f$ noise (also called flicker noise or excess noise) is a low-frequency noise whose PSD is approximately proportional to the frequency inverse as the form [17, 18], for example,

$$S_I(f) = \frac{K.I^{\eta}}{f^{\gamma}}, \tag{1.23}$$

where I is the current, K is a constant, η is the current exponent and usually equal 2, γ is the proportional constant being usually around 1. This formula can also be applied to resistance R, or voltage V whenever we replace I by R or V.

The $1/f$ noise is observed not only for physical processes, but also other ones including those in the nature. Here, we limit our concerns to $1/f$ noise in physical processes. As mentioned above, there is also many kinds of noise in physical quantities, and these noises usually exist together. Hence, the low-frequency noise, which is observed experimentally, is the summation of these noises, and the spectrum will have following characteristics: $1/f^{\gamma}$ ($\gamma \simeq 1$) behavior at low frequencies due to the $1/f$ noise, flat behavior at high frequencies due to white noise and/or measurement background noise, and some bumps at specific frequencies due to g-r noise, as schematically shown in Fig.1.9.

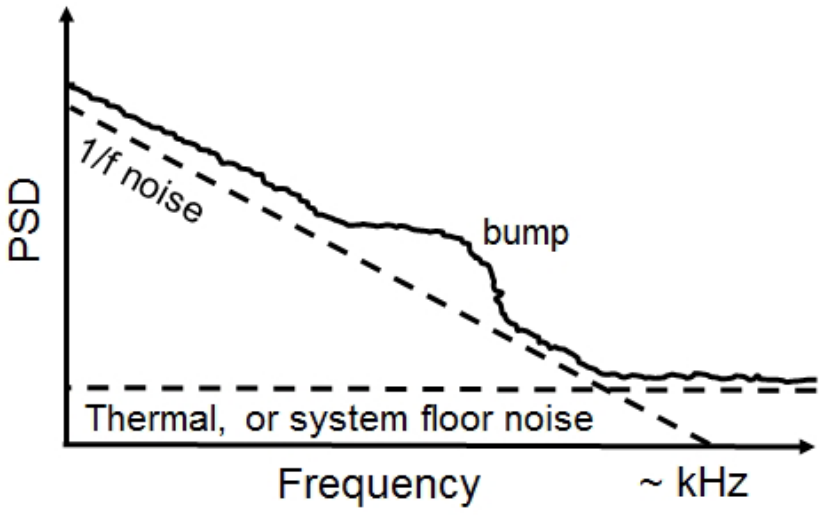

Figure 1.9: Noise power spectrum density (PSD) as a function of the frequency f

Since the white noise is independent of the frequency, we tentatively separate $1/f$ noise and g-r noise from the white noise, whose PSD depends on the frequency f, and call them as the low-frequency noise. Because the white noise is independent of the frequency, the low-frequency noise will become important when the frequency decreases, or in other words, when the working time of the devices increases. We hence can conclude that, for the device operation, the low-frequency noise plays a key role, and dominates other

noise sources. While the white noise is clearly clarified [19, 20], the low-frequency noise including $1/f$ and bump characteristics remains as controversies [17, 21–23] even it has been discovered for a long time [24, 25]. For example, the simple question of how low of the $1/f$ behavior is still remains. The observed lowest frequency for $1/f$ behavior is in order of 10^{-7} Hz [21], but we cannot conclude it is the minimum, and someone says that the lowest frequency for the $1/f$ behavior corresponds to the universe age, order of 10^9 years! If so, the total fluctuation will be infinite! But, according to Eq. (1.6) and (1.23), we can calculate the total fluctuations for the I as an example [26]

$$\frac{(\delta I)^2}{I^2} = \int_{f_\ell}^{f_h} \frac{S_I}{I^2} \mathrm{d}f = \int_{f_\ell}^{f_h} \frac{K}{f} \mathrm{d}f = K \ln \frac{f_h}{f_\ell}, \tag{1.24}$$

where f_ℓ and f_h is the below and above limits of the $1/f$ behavior. For example, if $f_\ell = 10^{-16}$ Hz (corresponding to a time of 10^9 years) and $f_\ell = 10^{20}$ Hz (corresponding to electromagnetic wave has wavelength of the Compton value $\sim 2 \times 10^{-12}$ m)

$$\frac{(\delta I)^2}{I^2} = K \ln \frac{f_h}{f_\ell} \simeq 83K, \tag{1.25}$$

this value is only 12 times higher than the total relative fluctuations in the frequency range of 1-100 Hz! Hence, we should not care about the limits of the $1/f$ behaviors, but we have to consider the K, which can be rapidly increased by scaling down of the device size [23]. Because $1/f$ noise plays an important role, the $1/f$ noise terminology usually has a meaning of the low-frequency noise. In this work, we use the low-frequency noise with the meaning of the $1/f$ noise.

Since noise is a nature of electronic devices/circuits, understanding of the noise mechanisms is useful for not only the devices/circuits optimization, but also science/technology developments. Moreover, the SNR becomes larger when the device size reduced [27], the noise understanding becomes more important as electronic devices/circuits are scaling down according to the Moore's law (More-Moore technologies). Furthermore, the noise is also important for the MtM technologies, e.g, phase noise affects the performances of RF, analog, mixed-signals... In accompany with the science/technology developments, the SNR is increasing continuously [28], the $1/f$ noise hence becomes a major concern especially for nano-device technologies [29]. Therefore, understanding and overcoming the $1/f$ noise problems are important challenges for the future of electronic devices/circuits. Furthermore, the $1/f$ noise is very sensitive to traps/defects in the device and is strongly related to physical processes such as trapping/detrapping phenomena, electron scattering mechanisms, and etc... The $1/f$ noise hence can be used as information-carrying signals to evaluate the material/device quality/reliability and get insights into the physics of the system [30]. The noise is the signal [31]!

1.3.2 Low-frequency noise models

The current density $\mathbf{j}$ flowing in a conductor is given by

$$\mathbf{j} = \sigma \mathbf{E} = (q n_\mathrm{e} \mu_\mathrm{e} + q n_\mathrm{h} \mu_\mathrm{h}) \mathbf{E}, \tag{1.26}$$

where σ is the conductivity, $\mathbf{E}$ is the applied electric field, q is the free carrier charge, $n_{\rm e}$ ($n_{\rm h}$) and $\mu_{\rm e}$ ($\mu_{\rm h}$) are concentration and mobility of electrons (holes). Since the current I

$$I \propto N\mu = \sum_{i=1}^{N} \mu_i, \tag{1.27}$$

where N is the total carrier number, μ_i is the ith carrier mobility, and μ is the average mobility, fluctuations in the current ΔI can be attributed to fluctuations in the mobility $\Delta\mu$ and/or those in the carrier-number ΔN. This is also the main controversy in the origin of $1/f$ noise [23]: fluctuations in the mobility or the carrier-number? There have been many efforts contributed to clarify the origin of the low-frequency noise ($1/f$ noise) for a long time, the controversy still remains but all agreed that the $1/f$ noise is fluctuations in the conductivity.

F. N. Hooge, in an effort to systematically collect data on $1/f$ noise, has empirically proposed a formula for the resistance fluctuations [32] on 1969

$$\frac{S_R(f)}{R^2} = \frac{\alpha_{\rm H}}{Nf}, \tag{1.28}$$

with $\alpha_{\rm H} \simeq 2\times10^{-3}$ was proposed as a universal constant. According to Eq. (1.28), the $1/f$ noise PSD is independent of other parameters excepting the carrier-number N, however, there were many researches showed the general invalidity of Eq. (1.28). Hence, a modified version of Eq. (1.28) can be considered in a more general form [18]

$$S_x(f) = \big(\frac{\mu}{\mu_{\rm ph}}\big)^2 \frac{\alpha_{\rm H}}{Nf} x^2, \tag{1.29}$$

where $\mu_{\rm ph}$ is the mobility due to phonon scattering, x can be resistance R, voltage V or current I, and the Hooge parameter $\alpha_{\rm H}$ is not a universal constant now. The Hooge proposal did not rely on any theoretical consideration, it does not prove anything. However, the origin of the $1/f$ noise according to the Hooge model is usually attributed to the fluctuations in the mobility due to the phonon scattering, and considered as a bulk effect. A strong evidence usually attributed to such a conclusion is the relation $\alpha_{\rm H} \propto \mu^2$ [17, 33].

On other efforts, McWhorter considered the carrier-number fluctuation as the noise source due to trapping/detrapping of carriers in traps located at a distance from the semiconductor/oxide interfaces [18, 34]. The noise caused by trapping/detrapping processes usually has the Lorentzian form [35]

$$S_n(f) = \langle(\Delta n)^2\rangle \frac{4\tau}{1+(2\pi f\tau)^2}, \tag{1.30}$$

where f is frequency, τ is the life time of a fluctuation Δn in the number of free carriers. The $1/f$ behavior of the noise spectra is due to a superposition of Loretzian spectra [35]

$$S(f) \propto \int_0^\infty g(\tau) \frac{4\tau\overline{(\Delta n)^2}}{1+(2\pi f\tau)^2}, \tag{1.31}$$

where $g(\tau)$ is a statistical weight. With an assumption of non-uniform traps distribution with $g(\tau) \propto 1/\tau$, the noise spectrum can be obtained as [16, 18, 35]

$$S(f) \propto \begin{cases} constant & \text{for } 2\pi f \ll 1/\tau_1, \\ 1/f & \text{for } 1/\tau_1 < 2\pi f < 1/\tau_2, \\ 1/f^2 & \text{for } 2\pi f \gg 1/\tau_2 \end{cases} \tag{1.32}$$

where, τ_1 and τ_2 the time constants decided by the smallest and largest distances of tunneling, respectively. The McWhorter model is different from Hooge model not only in the frequency dependence of PSD but also in the origin of noise source. According to the McWhorter model, the $1/f$ noise is due to fluctuations of carrier number coming from the generation-recombination processes of electron owing to the traps that can be from the interface or surface states. Both models dealt with the low-frequency noise, and tried to describe the $1/f$ noise. However, spectrum of PSD given by McWhorter model shows the difference from that given by Hooge model when the frequency exceeds to the very high or low range at which the PSD spectrum is similar to that of white noise.

We realized by using Eq. (1.27) that the Hooge model or McWhorter model is not always true because of various noise mechanisms. In addition to these models, there have been other models proposed to explained the $1/f$ noise such as temperature fluctuation model by Voss and Clarke [36] or by Dutta and Horn [21, 37], quantum mechanic model by Handel [38], and so on. Even there were many researches on $1/f$ noise, there is no clear evidence for a unified noise source up to now. $1/f$ noise seems coming from mobility fluctuations in some cases but from carrier number fluctuations in other ones. Moreover, $1/f$ noise also depends on the device dimensions as well as materials [23]. Furthermore, there have been many observations of low-frequency noise showing the spectra given by Eq. (1.32) rather than $1/f$ noise, suggested many difficult and obscure noise sources. However, studies on low-frequency noise as well as $1/f$ noise helps us understand more deeply the devices/circuits physics and know how to improve the device performances. Furthermore, noise is also a signal [31], and can be use as a diagnostic tool to evaluate the quality and reliability of electronic devices/circuits [30].

1.3.3 Low-frequency noise study on semiconductor devices

Low-frequency noise including $1/f$ noise in semiconductor devices has been studied for a long time due to its important role in the device performances. The studies have covered a variety of semiconductor devices, from the semiconductor films [39–42] to p-n junctions [43], metal-oxide-semiconductor transistors [44–47], and commercial devices [48, 49] by theoretical works [38, 50–54] and experimental works [55, 56]. The studies were due not only to characterization of the device low-frequency noise, but also to characterization of the other device properties such as interfaces in the device structure or material quality by using low-frequency noise as a diagnostic tool [57, 58].

Even there is evidence to conclude the noise sources in some specific cases, the distinguishing between the noise origins is not an easy task because there is also a correlation between the quantities characterizing the transport properties related to the noise generation. In general, there exists a controversy about the noise origin: bulk or surface noise [59], mobility or carrier-number fluctuations [23]? The bulk noise means the noise originated from fluctuations inside the device materials, while surface noise means the noise originated from semiconductor surface. The bulk noise is usually related to the fluctuations in the mobility, while the surface noise is often attributed to the fluctuations in the carrier number. However, the bulk (surface) noise does not mean the mobility (carrier-number) origin of the noise. The mobility fluctuations can be caused by fluctuations in phonon scattering, which was firstly proposed by Hooge [32] without fundamental theory. In this case, the noise is bulk noise. The mobility fluctuations also by other scatterings such as Coulomb scattering due to surface charges [60, 61], and the noise is surface noise.

In contrast, the carrier-number fluctuations are always considered as surface effects in which the surface/interface states make the free carrier number in the conducting channel fluctuated, for example, through tunneling of the free charges into the traps near the interfaces [62], or random walk of electrons in the interfaces [63]. For improving device performances, the identification of the noise origin is very important, however, there is no conclusive model about this issue up to now. For the metal-oxide-semiconductor field-effect transistors (MOS-FETs), the most important semiconductor device, the experimental results suggest that $1/f$ in n-MOS-FETs is dominated by carrier-number fluctuations while in p-MOS-FETs the noise is due to mobility fluctuations [23].

In order to study the low-frequency noise in metal-insulator-semiconductor field-effect transistors (MIS-FETs), with MOS-FETs are the MIS-FETs using an oxide as the gate insulator, clarification of the dependence of the noise parameters on the gate voltage is an effective approach, and usually to be used. Although the gate voltage is an important information for the device operation, it is only a transition parameter for the noise study. The changing in the gate voltage makes the transport properties such as mobility μ and sheet electron concentration n_{s} changed, hence the noise characteristics changed also. It should be reminded that the observed current or voltage noise, which is experimentally measured and analyzed for the noise characterization, is not originated by the current or the voltage itself. The observed current or voltage noise is just a transform of the fluctuations in resistance/conductance [17]. For the noise of the current following the Ohm's law (the flowing current proportional to the bias voltage), there exists a relation between the noise as follows (the proof in Appendix D.1)

$$\frac{S_I}{I^2} = \frac{S_V}{V^2} = \frac{S_R}{R^2} = \frac{S_G}{G^2}, \tag{1.33}$$

where I, V, R, and G are the current, voltage, resistance, and conductance; and S_I, S_V, S_R, and S_G are the noise power spectrum density of the current, voltage, resistance, and conductance, respectively. In conventional measurements, the current or voltage is only necessary to transform the already existing conductivity/resistivity fluctuations into current/voltage fluctuations that can be measured [17]. Hence, it is more explicit to interpreter the noise parameters in terms of transport properties carrying the current, which are the mobility μ and carrier concentration n (usually the sheet carrier concentration n_{s}). By analyzing the dependence of the noise parameters on the transport properties, we can take insights into the physics of the noise phenomena. For example, whenever the noise satisfies Eq. (1.33), we can defined an effective Hooge parameter α by

$$\frac{S_I}{I^2} = \frac{\alpha}{Nf}, \tag{1.34}$$

where the carrier number $N = LWn_s$ with conducting channel length L and width W, α usually exhibits a dependence on μ and/or n_{s}. In general, α is not a constant, but depends strongly on material quality and scattering mechanisms. Hence, it can be used as a crude evaluation for the material quality as well as for the device performances. The dependence of α on μ like

$$\alpha \propto \mu^2 \tag{1.35}$$

is usually considered as an evidence for mobility fluctuations [17, 33]. On the other hand, the dependence of α on n_s like

$$\alpha \propto {n_s}^{\xi}, \tag{1.36}$$

with ξ can be a variable, depending on the noise model [64], where $\xi = -1$ is usually interpreted as evidence of the carrier-number fluctuations [23, 64]. However, the noise origin as well as the noise generation mechanism are still in controversy because the noise, in particular low-frequency noise, does not exhibit a unique behavior. Moreover, there may be a correlation between μ and n_s, which should be considered in the explanation of the noise characterization. Therefore, the study on the device low-frequency noise characteristics is still a challenge, which asks for much more efforts.

1.4 Research motivation

Although low-frequency noise in semiconductor devices has been being studied for a long time (more than one century), there is no conclusive theory for such important field of the physics. The noise origin is still a big controversy. Hence, this work aims to take insights into the low-frequency noise mechanisms of the semiconductor devices because understanding of the noise characteristics is essential for improving the device performances.

In addition, III-V compound semiconductors have many advantages, which are important to improve the device performances that cannot be achieved by silicon-based devices, adding new values to the devices according to the More-than-Moore diversification. This work aims to take insights into the physics of some important III-V compound semiconductors such as InAs - an important narrow gap semiconductor, which is potential for high-speed, low-power consumption device applications, and GaN - an important wide gap semiconductor, which is promising for high-power, high-frequency and high-temperature applications, with main focuses on the device low-frequency noise characteristics.

Due to potential of InAs, it has been attracting much research attention, but there were only a few studies devoted to low-frequency noise characterization of InAs-based devices [65–70]. In particular, InAs thin film systems are important due to its very high electron mobility. The InAs thin films can be obtained by heterostructure growth on GaAs(001) or heterogeneous integration on foreign host substrate, for example, InAs bonded on low-dielectric-constant flexible substrates (low-k FS) [71] by epitaxial lift-off (ELO) and Van-der-Walls bonding (VWB) techniques [72], the latter is a potential approach to obtain high electron mobility InAs thin films [71] but holding many challenges because of complicated methods. Even low-mobility thin films were obtained, InAs/GaAs(001) has its advantages due to simple growth method. Therefore, both InAs film systems obtained by direct growth or by heterogeneous integration are important for the device applications. Despite of the importance of the InAs films, there is no report on their low-frequency noise characteristics.

In comparison to InAs-based devices, GaN-based devices are more mature. Although low-frequency noise in the GaN-based devices has been studied for a long time, the previous studies mainly focused on Schottky heterojunction field-effect transistors (Schottky-HFETs) [73–90] and MIS-HFETs with the oxide gate insulators [91–100] with a few exception of SiN gate insulator [101]. Moreover, in many previous studies for FETs, it is difficult to identify the contribution from the intrinsic gated region and extrinsic ungated region. Therefore, it is important to obtain insights into low-frequency noise in GaN-based MIS-HFETs with nitride insulators such as AlN, comparing with the Schottky devices, and clarifying the contribution from the intrinsic and extrinsic regions.

In this work, we investigate low-frequency noise characteristics of the devices fabricated from InAs films bonded on low-k flexible substrate (InAs/FS) in comparison with those of devices fabricated from InAs films grown on GaAs(001) substrate (InAs/GaAs). Accompanying with low-frequency noise characterization, we also measure electron transport properties of the InAs films with intention of finding relations between low-frequency noise characteristics and transport mechanisms. In addition, we systematically investigate low-frequency noise characteristics in AlN/ AlGaN/GaN MIS devices, i.e., AlN/AlGaN/ GaN MIS-HFETs as well as AlN/AlGaN/GaN ungated two-terminal devices, with the AlN insulator deposited by RF sputtering on the AlGaN. In comparison, we also investigate low-frequency noise characteristics in AlGaN/GaN Schottky devices, i.e., AlGaN/GaN Schottky-HFETs as well as AlGaN/GaN Schottky ungated two-terminal devices. In combination with investigation of low-frequency noise in the ungated two-terminal devices, we extract low-frequency noise behaviors of the intrinsic gated region in the HFETs, and clarify the dependence of noise behaviors on the transport properties under the gate, which depend on the device operation conditions, i.e., the current and bias voltages.

From the characterization, we aim to take deep insights into the low-frequency noise characteristics of the III-V compound semiconductors with devices fabricated from the InAs films or GaN heterostructures as examples. Furthermore, by clarifying the low-frequency noise characteristics, we also aim to take insights into the device physics with a further goal of making contribution in order to improve the device performances.

1.5 Thesis organization

The thesis includes five chapters. The content of each chapter is summarized as follows.

Chapter 1 is used for introduction about the More-than-Moore tendency in the development of the semiconductor devices, and the history and background of the research on the noise, in particular the low-frequency noise, in semiconductor devices. The motivation and organization of the thesis research are also explained.

Chapter 2 discusses about configuration and characterization of low-frequency noise measurement systems. In addition, the measurement specifications are also discussed in details.

Chapter 3 is used to characterize the low-frequency noise in the InAs devices, including the device fabrication process, measurements of electron transport properties and characterization of the device low-frequency noise. The chapter also discusses a low-frequency noise model by a general calculation with Burgess theorem to obtain general expressions for the current noise parameters without specific assumptions.

Chapter 4 is devoted to low-frequency noise investigation of AlGaN/GaN devices, including the device fabrication process, device DC characterization and low-frequency noise characterization. After a brief presentation about the device fabrication process, the DC characteristics are discussed and compared between AlN/AlGaN/GaN MIS devices and AlGaN/GaN Schottky devices. And, the investigation of low-frequency noise in ungated two-terminal devices and HFETs, including the MIS structures and the Schottky structures, completes the chapter.

Chapter 5 concludes this work, and discusses the future perspectives of the work.

Chapter 2

Low-frequency noise measurement system

2.1 Low-frequency noise measurement system configuration

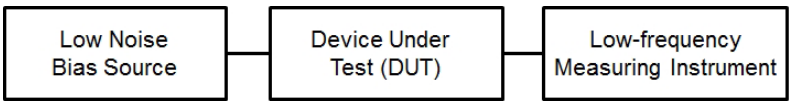

Figure 2.1: The configuration of low-frequency noise measurement systems.

A measurement system for low-frequency fluctuations (or noise) usually consists of three main components with a configuration described in Fig. 2.1 The low-noise bias source is used to bias the measured devices, and usually to be a battery or a battery and a combination of a source measurement unit (SMU) and a low-pass filter (LPF). The purpose of using a battery instead of power supply sources is to avoid the noise from AC power supplies, for instance, a peak at about 50 or 60 Hz is sometimes observed in the measured spectra with a connection of the bias sources to AC power supplies. For measurements with three-terminal (3T) devices, we usually use a combination of a SMU and a LPF to bias third terminal (usually the gate of transistors). The LPF plays a role of suppressing low-frequency noise from the SMU, preventing the SMU noise from affecting the device signals. The LPF hence has to have a cut-off frequency lower than the lower limit of the measured frequency range to stop every SMU signals having frequencies in the measuring range. The frequency range for low-frequency noise measurements is usually from 1 Hz to about 10 kHz, hence, the LPF cut-off frequency should be less than 0.1 Hz. Due to the presence of the LPF, all low-frequency signals from the bias sources cannot enter the DUT. In addition, the LPF must not give additional noise to the device signals, it hence has to have a low-noise nature during measurements to prevent from adding its low-frequency noise to the signals. For that purpose, the LPF should include only the passive components without amplification functions. In addition, the low-frequency measuring instrument is used to detect and analyze the signals from the devices, and usually to be a combination of a low-noise current pre-amplifier (LNA) and a signal dynamic analyzer

(DSA), in which the LNA is used to amplify the device small signals before they enter the analyzer. The LNA hence has to be a low noise instrument to ensure that its noise does not modify the device signals. Furthermore, the LNA should have a long-time internal battery, which will be used as a power supply during measurements to prevent from using AC external power supplies because the AC sources may give external noise such as peaks or spikes at about 50/60 Hz. Owing to its function, the signal analyzer has to own fast Fourier transform function to convert the signal from time domain to frequency domain, and a background noise lower than the device signals after amplified by the LNA to ensure that the measured noise would not dominated by the analyzer background noise.

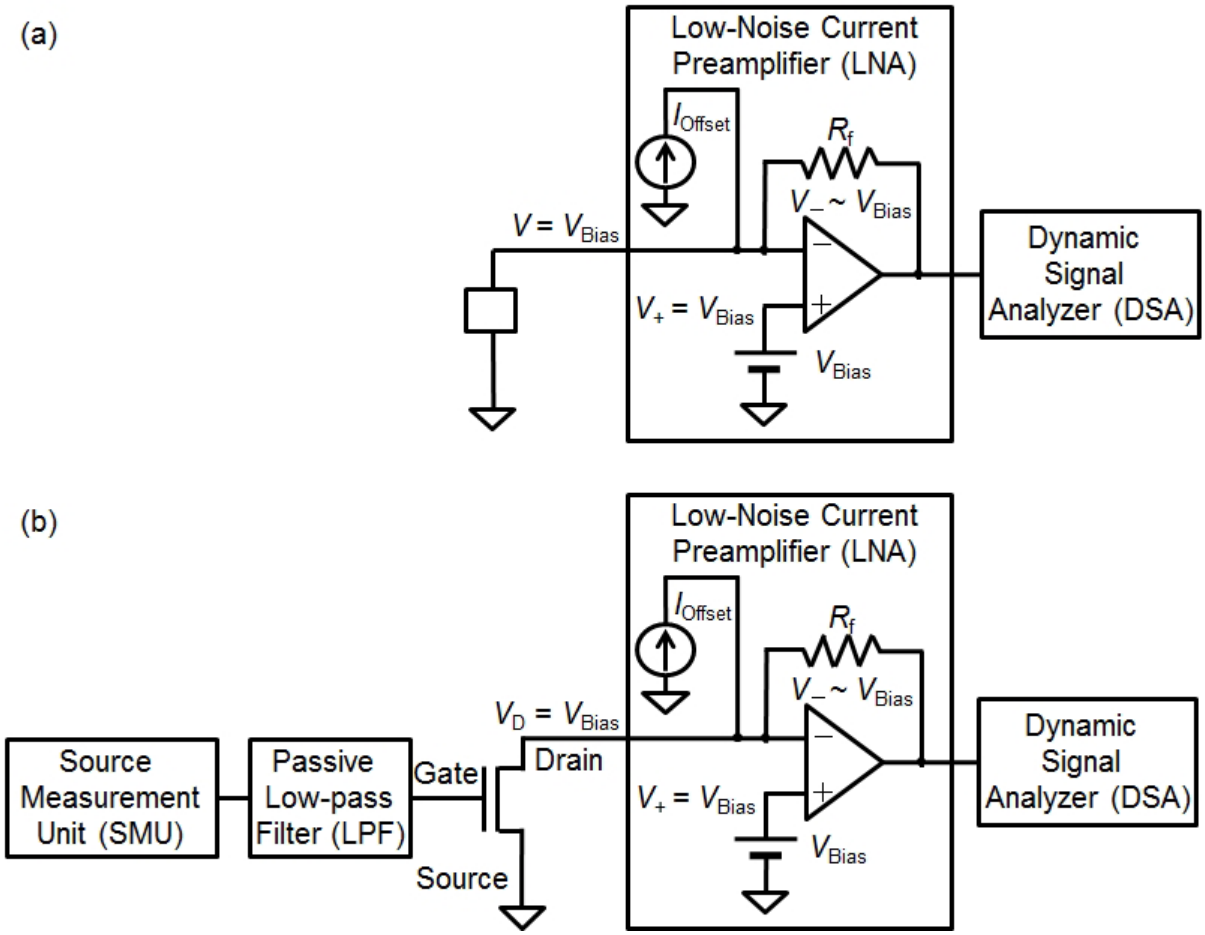

Figure 2.2: Low-frequency noise measurement system for (a) 2T DUTs and (b) 3T DUTs.

In order to measure device-under-test (DUT) with two terminals (2T) such as diodes, or three terminals (3T) such as transistors, we established a low-frequency noise measurement system with different configurations as described in Fig. 2.2. The difference between two configurations comes from the low-noise bias source. For 2T-DUT measuring system, the devices will be biased directly by using power supply batteries of the LNA. The biasing by using LNA input is based on the virtual ground, which is a nature of op-amp components inside the LNA. On the other hand, the 3T-DUT measuring system uses battery of the LNA, and one more combination of a SMU and a LPF for biasing measured devices. In this usage, the LNA battery is usually used to bias the second terminal of the 3T DUTs, for example, the drain of a field-effect transistor (FET), while the SMU will

be used for biasing the third terminal, for instance, the gate of a FET.

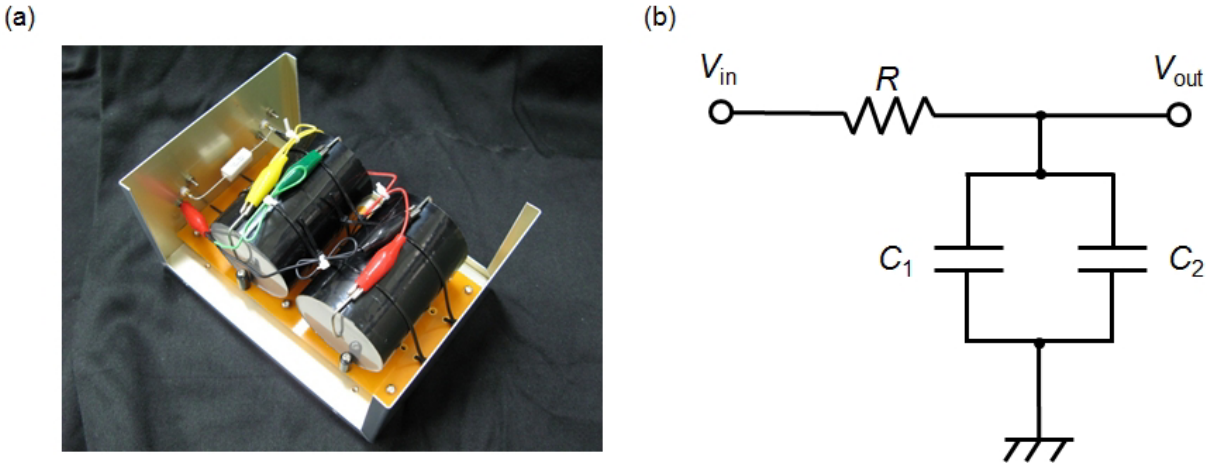

Figure 2.3: (a) Low-pass filter and (b) its circuit.

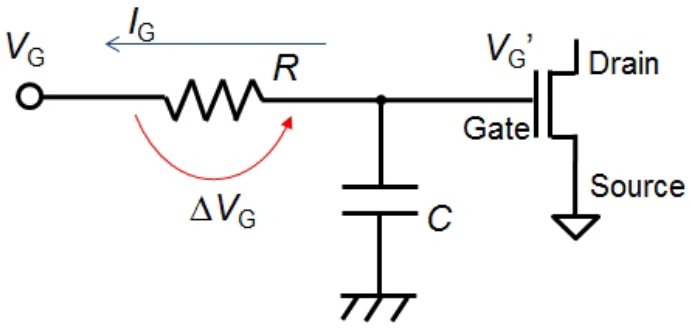

Figure 2.4: A circuit of the LPF and the gate of an FET in series connection.

Due to the simpleness of the battery bias source, we will devote our discussion on the low-noise bias sources to the source used for biasing the third terminal in the 3T-DUT measuring system. In our 3T-DUT measuring system, the low-noise bias source includes a battery of the LNA of Standford Research System, SR570 model, and a combination of a source measurement unit (SMU) of Agilent Technologies, 4155C and a LPF, where the combination is used for biasing the third terminal. Due to an important role of the LPF, the details of the LPF will be discussed. The LPF, which was made by our laboratory, includes a cement resistor of 10 kΩ and two film capacitors of 150 μF. An image of the LPF is shown in Fig. 2.3(a), and its circuit is schematically shown in Fig. 2.3(b). The reasons of choosing a resistance and capacitors with the above values are discussed as follows. Because the LPF is connected to the gate of FETs, the connection circuit is as in Fig. 2.4. When we apply a voltage V_G to bias the gate, there exits a gate leakage current. Although the gate current is very small, it is not zero. Hence, a voltage drop ΔV_G on the resistance R appears, and decreases the actual voltage applied on the gate. The higher R the higher ΔV_G. To reduce the voltage drop, the resistance is not so large. But we cannot choose a too small resistance because there exists a trade-off between the resistance and the capacitance due to a higher limit of the LPF cut-off frequency. The cut-off frequency

of the LPF is given by

$$f_{\mathrm{T}} = \frac{1}{2\pi RC} \leq 0.1 \text{ Hz}, \tag{2.1}$$

hence the small R leads to the large C. The large C gives a risk of the capacitor, for example, large leakage. Therefore, R cannot be arbitrarily small. In our measurements, we will use AlGaN/GaN Schottky heterojunction FETs, which usually have gate leakage currents in order of 10^{-6} A (for reverse biases) [102], and gate bias voltages in order of 1 V. The small drop voltage condition is

$$\Delta V_{\mathrm{G}} = I_{\mathrm{G}} R \ll V_{\mathrm{G}}, \tag{2.2}$$

$$R \ll \frac{V_{\mathrm{G}}}{I_{\mathrm{G}}} \sim 1 \text{ M}\Omega. \tag{2.3}$$

Hence, we chose $R \sim 10$ kΩ. According to Eq. (2.1), the value of the capacitance is $C \sim 300$ μF. This resistance is quite large, it may have its own noise signal. However, we do not need to care for the resistance noise, also for any noise source before the LPF, because the LPF will stop all such noise sources. We next discuss on the LPF characteristics. The cut-off frequency of the LPF is calculated using the LPF circuit shown in Fig. 2.3(b) as follows

$$\begin{aligned} f_{\mathrm{T}} &= \frac{1}{2\pi RC} \\ &= \frac{1}{2\pi \times 10\text{k}\Omega \times 300\mu\text{F}} \simeq 0.05\text{Hz}. \end{aligned} \tag{2.4}$$

This cut-off frequency is considered to be low enough for our measurements with frequency equal 1 Hz or higher. The details of the LPF characteristics with the signal responses will be discussed on next section devoted to the LPF.

After setting the measurement system, the system characterization will be done to clarify the validity of the system. After confirmation of the system validity, measurements with the devices will be performed. The measurement procedures can be briefly summarized as follows. The DUTs, including probe station, are enclosed in a shielding box to reduce external effects. An SR570 low-noise preamplifier (LNA) is used to amplify weak current noise signals of the devices before they enter the spectrum analyzer, and converts the current noise signals to voltage noise signals via setting of the LNA sensitivity. The output voltage noise signal will be detected by an Agilent 35670A dynamic signal analyzer (DSA), and converted to current noise by a load resistor R_{f} of the LNA, which determines the sensitivity of LNA and the below detectable limitation of the signal by setting a corresponding noise floor of the LNA. The LNA sensitivity is an important factor,which shows the relation between the current noise signals S_I at the input of the LNA (the device original signal) and voltage noise signals S_V at the output of the LNA through the equation

$$S_V[\mathrm{V}^2/\mathrm{Hz}] = \text{sensitivity}^2[\mathrm{V}^2/\mathrm{A}^2] \times S_I[\mathrm{A}^2/\mathrm{Hz}]. \tag{2.5}$$

The voltage noise will be detected and analyzed by the DSA, which has a fast Fourier transform function to convert the signal in time domain to frequency domain. The noise spectra, which show a noise power spectrum density S_V as a function of frequency f, will be obtained. The device current noise S_I is obtained by converting the S_V by using Eq. (2.6).

2.2 Low-frequency noise measurement system characterization

In this section, we will discuss components of the measurement system in details. The measuring instrument specifications will be characterized basing on the measurement system characteristics.

2.2.1 Dynamic signal analyzer

The signal analyzer used for our measurements is a dynamic signal analyzer (DSA) of 35670A made by Agilent Technologies. The Agilent 35670A DSA is a versatile Fast-Fourier Transformation (FFT) analyzer with built in source for general spectrum and network analysis. The 35670A DSA will detect the noise signal in the time domain, and convert it to frequency domain by using the FFT function. For one measurement, the DSA controls frequency span (frequency range for one measurement), frequency resolution (measured frequency lines for one frequency span), and measured frequency range (a combination of measured frequency spans). To obtain accurate results, the measurement should be done in many times, and gotten in average, the averaging number will determine the total time for measurements.

The DSA is also an electronic instrument, it hence has a background noise. The background (or floor) noise of the DSA will set the lower limit for the measured signal. The noise floor of the 35670A DSA is measured by considered it as a voltage noise source with different input conditions: open, short, and 50 Ω. The results are shown in Fig. 2.5.

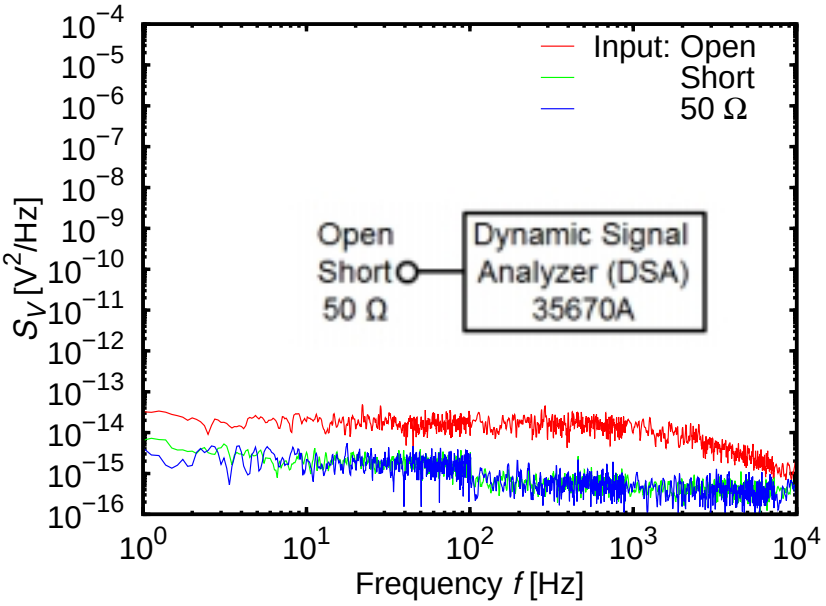

Figure 2.5: Floor noise of the 35670A dynamic signal analyzer, measured with different inputs. The measurement configuration is schematically described as the inset.

We realize that the floor noise of the DSA is white noise in order of 10^{-14} V^2/Hz, this is also the lower limit of our measurement system. However, the real lower limit of the measured signals should be several order higher than this value to ensure that the

floor noise does not affect to the measured results. The main characteristics of the DSA 35670A are listed as follows.

- Frequency span: 98 mHz - 51 kHz.
- Frequency resolution: 400, 800 and 1600 lines.
- Input impedance: 1 MΩ.
- Output mode: voltage noise
- Analysis mode: FFT.
- Dynamic range: 90 dB; accuracy: 0.15 dB.

2.2.2 Low-noise current preamplifier

In order to amplify the small device signal before it enters the DSA, a low-noise current preamplifier is used. The amplifier used for our measurement system is an SR570 low-noise current preamplifier (LNA), made by Standford Research System (SRS). Statements from the instrument maker about the LNA specifications are as follows: "The SR570 is a low-noise current preamplifier capable of current gains as large as 1 pA/V. It has sensitivity settings from 1 pA/V to 1 mA/V that can be selected in a 1-2-5 sequence. An input offset-current (up to 5 mA) adjustment is provided to suppress any undesired DC background currents. Offset currents can be specified from 1 pA to 5 mA in roughly 0.1% increments. The SR570 also has an adjustable input DC bias voltage (up to 5 V) that allows us to directly sink current into a virtual null (analog ground) or a selected DC bias." The SR570 works with battery mode, meaning no AC power connection during the measurements (only for charging the batteries before measurements). The battery operation ensures that no power supply noise will contaminate the input signals.

The input of LNA is device current noise signal S_I and the output is voltage noise S_V with an amplification. The signal is amplified with the sensitivity of s_{LNA} by

$$S_V[\mathrm{V}^2/\mathrm{Hz}] = {s_{\mathrm{LNA}}}^2[\mathrm{V}^2/\mathrm{A}^2] \times S_I[\mathrm{A}^2/\mathrm{Hz}]. \tag{2.6}$$

Measurements are performed with a control of the LNA sensitivity as follows. Because the lower limit of the DSA is fixed, about 10^{-14} V^2/Hz as shown in the Fig. 2.5, the sensitivity will determine the lower limit of the input of the LNA, meaning the lower limit of the DUT output signals that can be detected by the DSA at that sensitivity. Furthermore, the LNA also has its impedance that depends on the sensitivity, ranging from 1 Ω to 1 MΩ. The internal impedance of the LNA R_{in} will affect again the measured device signals, and may modify the device signals and/or the LNA output. An equivalent circuit for the DUT of resistance R in connection with the LNA in series is schematically shown in Fig. 2.6. The device current signal i will be transferred to the LNA, and the current signal after ther LNA input is $\widetilde{i}$, which will be amplified by the LNA gain G, the gain will determine the LNA impedance: the higher G the higher R_{in}, and become the voltage signal v at the LNA output. The current signal after the amplification of the input is given by

$$\widetilde{i} = \frac{R}{R + R_{\mathrm{int}}} i = \frac{1}{1 + R_{\mathrm{int}}/R} i. \tag{2.7}$$

The voltage signal at the LNA output is determined by the LNA gain

$$\widetilde{v} = G\widetilde{i} = G\frac{1}{1 + R_{\mathrm{int}}/R} i. \tag{2.8}$$

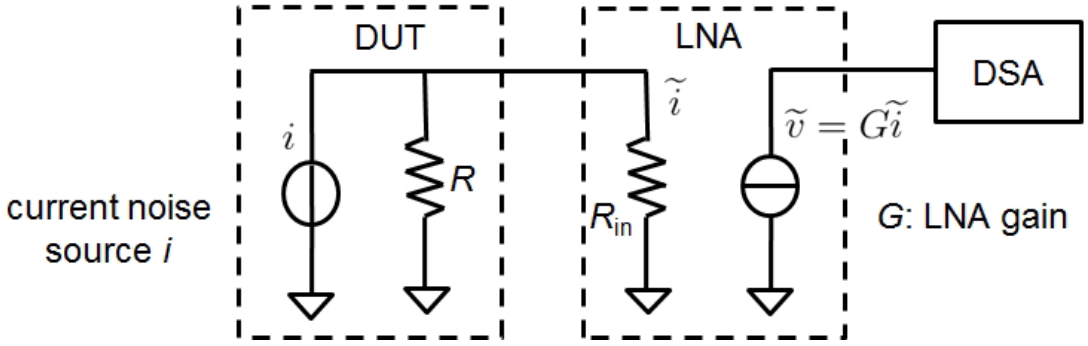

Figure 2.6: Equivalent circuit of DUT, LNA and DSA in series connection.

We realize that,

$$\widetilde{v} = G\frac{1}{1 + R_{\text{int}}/R}i \simeq Gi \Leftrightarrow R_{\text{int}} \ll R. \tag{2.9}$$

For measurements, the high gains with low input impedance are desired, but there exists a trade-off between them. This trade-off should be considered during measurements. The trade-off is also between the sensitivity, that is required to get lower current noise limits for higher sensitivities, and the device resistance, that is required to have lower ratio with the LNA impedance for higher sensitivities. For example, the DUT with $R = 200\ \Omega$ is measured, the sensitivity should be chosen to be 10^3 or 10^4 V/A, corresponding to the internal impedance of 1 Ω. If the sensitivity is higher, the internal impedance will dramatically increase (100 Ω for 10^5 V/A sensitivity, as shown in the specifications at the end of the section), and the condition given by Eq. (2.9) will be broken, i.e., the measured signals are not the complete device signals.

For pre-measurement tests, the LNA is considered as a noise source and connected with the DSA with different input conditions: open, short, and 50 Ω. The measurement results are shown in Fig. 2.7, these are also the LNA noise floors at the measured conditions. We observed small power supply noise spikes at about 60 Hz, for very high sensitivity in the case of open input of the LNA. However, we do not care about this external noise because two reason: First, these sensitivity has very large internal impedance, they should not be used for device with small resistance as discussed in Eq. (2.9). Second, the spikes are much lower than the noise floor of small sensitivities, which have small internal impedance and should be used for our measurements. Furthermore, the spikes disappear in measurements with short or 50 Ω inputs, similarly to real measurements with DUT input. Hence, these spikes do not appear in our measurements with devices as seen in the later chapters.

The specifications of the LNA is as follows.

- Gain mode: low-noise
- Maximum off-set current: 5 mA (down to 1 pA)
- Maximum bias voltage: 5 V (down to 1 mV)
- Frequency range: DC-1 MHz
- Sensitivity (Input impedance): 10^3, 10^4 V/A (1 Ω), 10^5, 10^6 V/A (100 Ω), 10^7, 10^8 V/A (10 kΩ), $10^9 - 10^{12}$ V/A (1 MΩ).

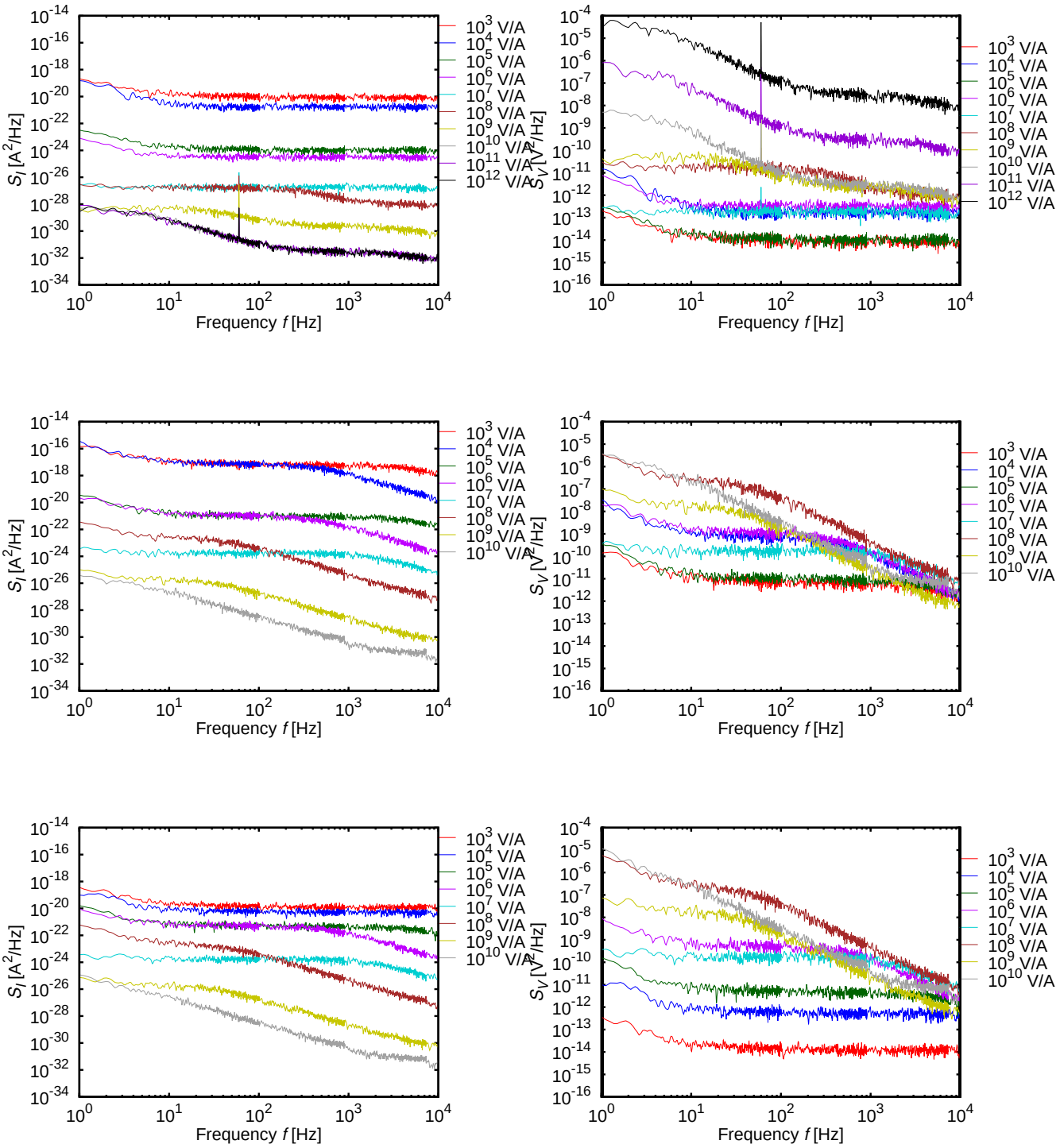

Figure 2.7: Floor noise of the SR570 amplifier, measured with different inputs from top to bottom are for open, short and 50 Ω inputs. The power supply noise at 60 Hz is observed at open condition with high sensitivities, this may be due to exposure of the input channel in the atmosphere without shielding chamber.

2.2.3 Low-pass filter

The LPF used for the measurement system was briefly described in the section 2.1, we will show here its characteristics with different configurations. Before measuring with the

devices, we characterized the LPF used for the measurement system. We tested the LPF using the following scheme.

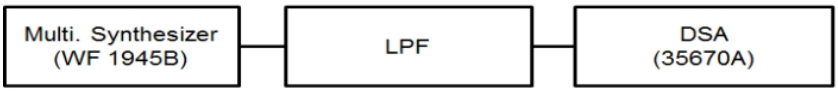

Figure 2.8: Schematic configuration for the LPF test.

A multifunction synthesizer WF 1945B is used to form the input signals with wave and pulse functions. The signals are then transferred to the LPF and the output will be detected and analyzed by an analyzer (Agilent DSA 3650A for wave signals, and Tektronix Oscilloscope TDS3000B for pulse signals). The measurements with pulse signals was shown in Fig. 2.9, which exhibited a cut-off frequency less than 0.05 Hz, and a rate of frequency roll-off about -20 dB/decade.

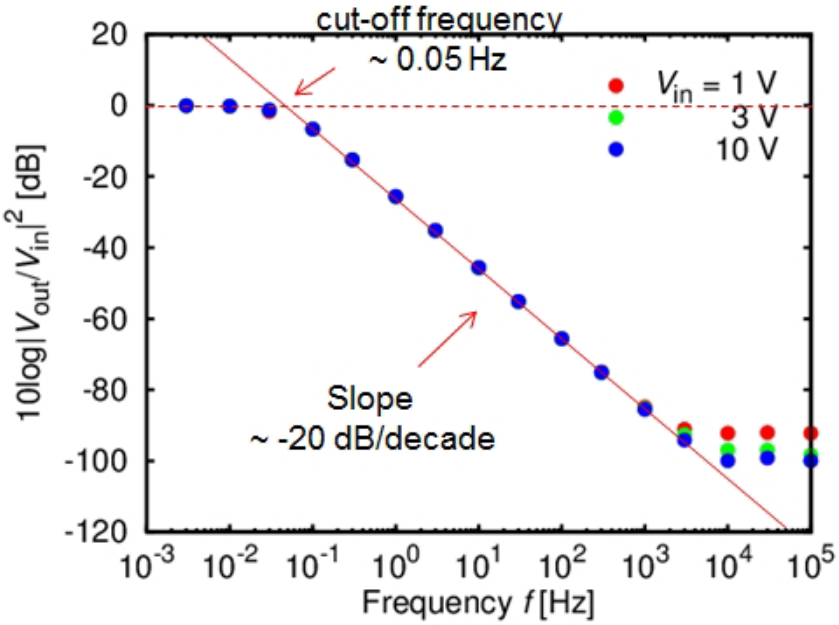

Figure 2.9: Low-pass filter response with the pulse signals.

The background of the LPF may be due to the lower limit of the oscilloscope, and also comes from interactions among the system components, which cannot be completely excluded. But the noise background is out of our measurement frequency range, and low enough to ensure that it cannot dominate or affect to the measured signals. These characteristics told us that the LPF could be used for our measurements with frequency range equal or higher than 1 Hz without any wonders of the effect of signal generator's noise to the DUT noise characteristics. To confirm the effectiveness of the LPF, we carried out the measurements with wave signals, as shown in Fig. 2.10. We can realize that the signals with frequencies higher than the cut-off frequency is completely suppressed with a rate of frequency roll-off about -20 dB/decade similarly to the LPF response with pulse signals, and the output noise background is same as that of the analyzer. This means that the LPF can not only suppress the signals with frequency higher than its cut-off

value, but also not generate any new signals. The output background depends only on the analyzer lower limit.

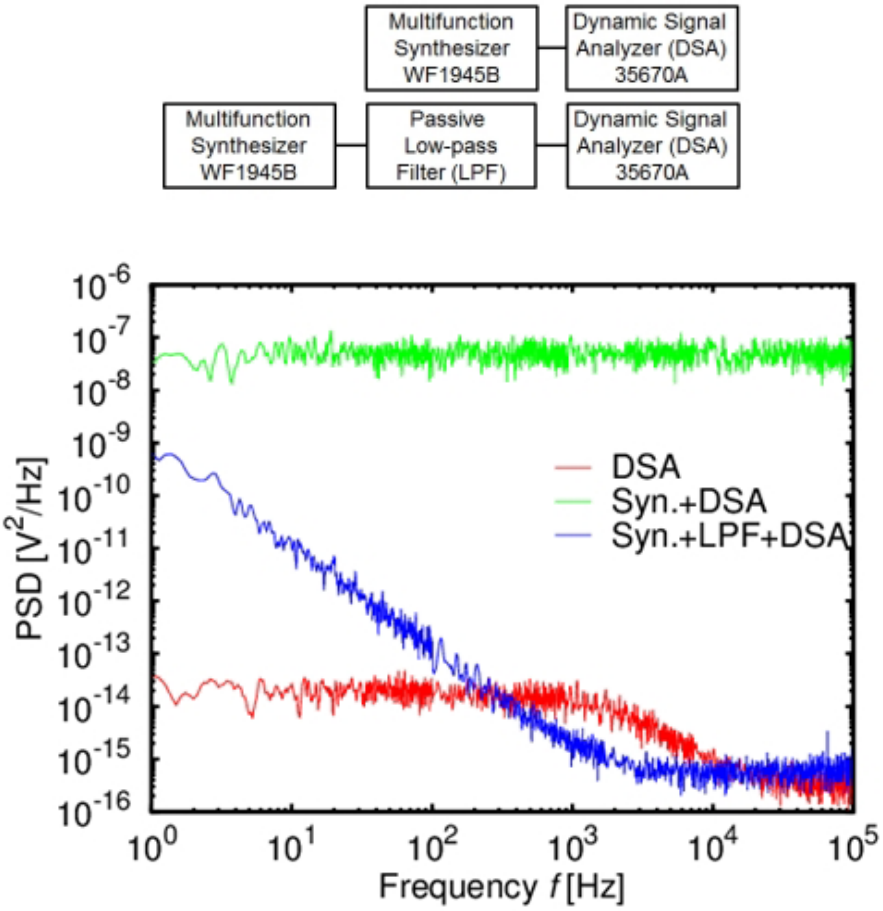

Figure 2.10: Low-pass filter response with the wave signals. The measurement configuration is schematically described.

2.2.4 Source measurement unit

The SMU used for the measurement system is an Agilent Technologies 4155C semiconductor parameter analyzer. The Agilent 4155C can generate and measure a voltage and a current at the same time. It can be used as an analyzer for the device DC characterization, and then as a voltage source for gate biasing in low-frequency noise measurements with three-terminal DUT, e.g. FETs. The SMU can supply a bias up to ± 40 V with 1 mV steps. The measurement results for noise floors of the SMU and a combination of SMU and LPF are shown in Fig. 2.11. We realize that the SMU-related floor noise is almost same as the floor noise of the DSA shown in Fig. 2.5. It means that the SMU and LPF do not add noise to the system. We also observe power supply noise spikes for the case of SMU, but these spikes are suppressed in measurements with LPF, suggesting a good filter property.

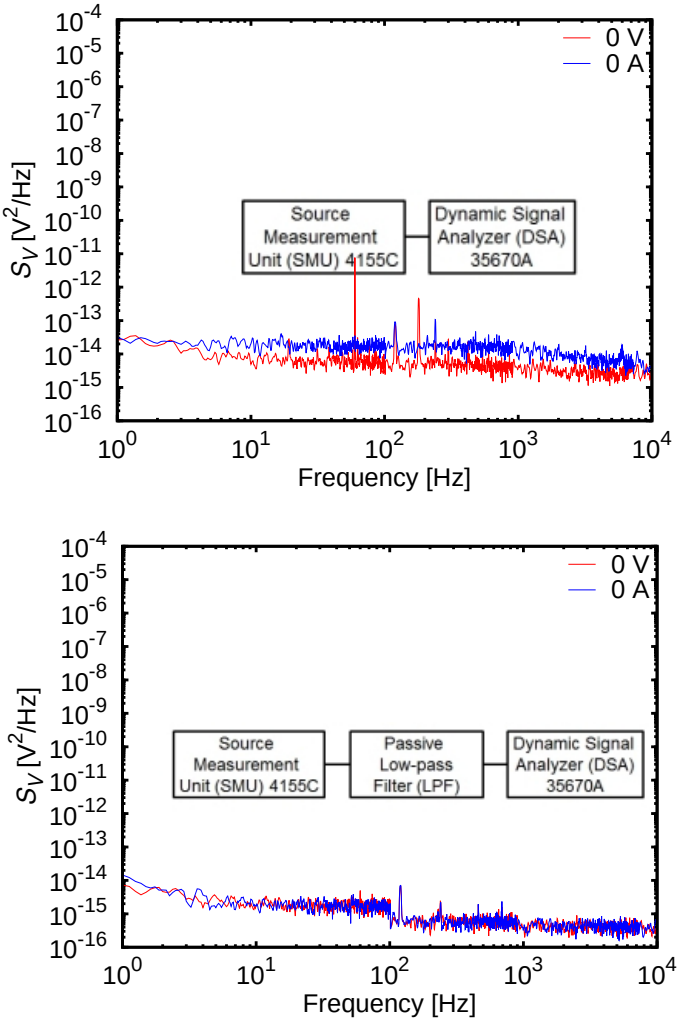

Figure 2.11: The floor noise of the SMU and a combination of SMU and LPF with different outputs of the SMU: 0 V and 0 A output. The measurement configuration is schematically described in the inset.

2.3 Summary

2.3.1 Summary of measurement setting

After characterization of the measurement system components, we have tested for the system, and compared with some typical results. The test results are shown for our measurement system in the Fig. 2.12(a), and a comparison data in Fig. 2.12(b) [103]. We can see that all the noise floors are at almost the same typical values with neither peaks nor bumps from the external noise sources, implying valid settings for the measurement system.

Basing on the above characterization, we will use the followed setting parameters for our measurements:

The DSA (for data analysis) has

- Frequency range from 1Hz up to $\sim$ 10 kHz with frequency spans: 1-101 Hz, 101-901

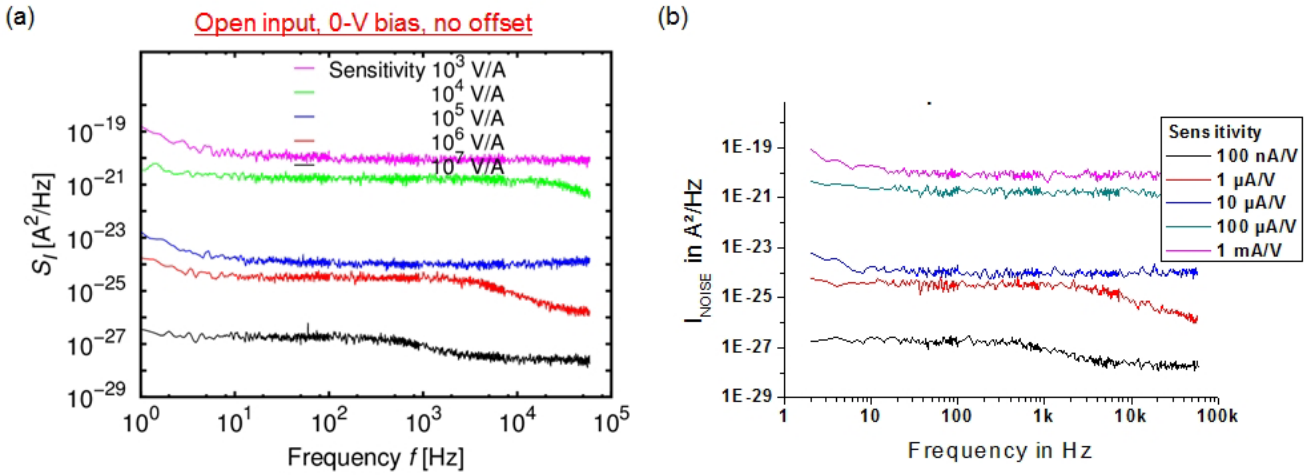

Figure 2.12: (a) Measurement system floor noise and (b) its reference in [103].

Hz, 901-7301 Hz.

- Frequency resolution: 800 lines
- Averaging time: 30
- Output mode: voltage noise
- Analysis mode: FFT.

The LNA (for obtaining data) has

- Gain mode: low-noise
- Off-set current and bias voltage: determined by I-V measurements.
- Sensitivity (Input impedance): 10^3, 10^4 V/A (1 Ω) for small resistance devices, 10^5, 10^6 V/A (100 Ω) for large resistance devices.

All parameter settings are remotely controlled by a VEE program (a product of HP Technologies) using a computer through GBIP addresses.

2.3.2 Summary of chapter 2

We established a measurement system with different configurations for low-frequency noise in 2T and 3T DUTs. The system characterization is summarized as follows.

- The measuring frequency ranges from 1 Hz up to 10 kHz.
- The voltage biasing devices is up to ±5 V with 1 mV steps.
- The off-set current suppressing DC component is up to ±5 mA with steps down to 1 pA.
- The cut-off frequency of the LPF is low enough (0.05 Hz $\ll$ 1 Hz).
- The noise floors are almost at the same as typical values without effects from external noise sources, confirming the validity of the measurement system.

Chapter 3

Low-frequency noise in InAs films bonded on low-k flexible substrates or grown on GaAs(001)

3.1 Fabrication of InAs film devices on low-k flexible substrates or on GaAs(001)

Two-terminal devices were fabricated by using InAs films grown on GaAs(001) (InAs/GaAs), or InAs films bonded on low-dielectric-constant (low-k) flexible substrates (FS) (InAs/FS). The InAs/GaAs(001) was obtained by a direct growth of InAs layers on GaAs(001) substrates, and the InAs/FS was achieved by a separation-bonding formation of InAs layers on low-k FS. For the InAs/FS, InAs films were firstly grown on GaAs(001) substrates with a sacrificial layer (the heterostructure is schematically shown in Fig. 3.1(b)), then separated from the GaAs(001) substrates by epitaxial lift-off (ELO) process [72], and finally bonded on low-k FS by Van-der-Waals bonding (VWB) [71, 104].

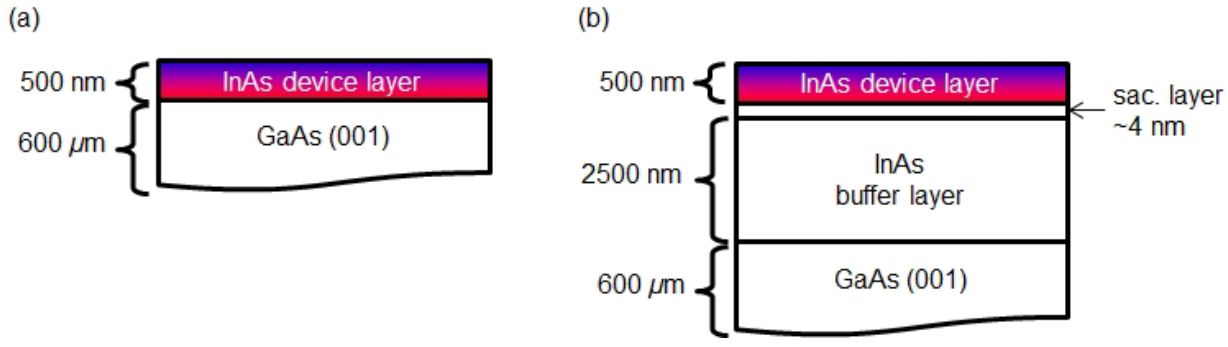

Figure 3.1: Schematic of (a) InAs/GaAs(001) and (b) InAs/sacrificial/buffer/GaAs(001) heterostructures. The sacrificial layer is $In_{0.3}Al_{0.7}As$(1 nm)/AlAs(2 nm)/$In_{0.3}Al_{0.7}$(1 nm).

The InAs/GaAs(001) and InAs/sacrificial/buffer/GaAs(001) heterostructures, which are schematically shown in Fig. 3.1 with their cross-section and layers' thickness, were obtained by solid-source molecular beam epitaxy (MBE). For the heterostructure used for ELO-VWB, an InAs buffer layer was used to reduce effects of lattice-mismatch (between

GaAs and InAs layers) on the InAs device layer. In order to reduce large-lattice mismatch between layers, a composite thin sacrificial layer including $In_{0.3}Al_{0.7}As$(1 nm)/AlAs(2 nm)/$In_{0.3}Al_{0.7}As$(1 nm) was employed. The conditions for MBE growth of InAs heterostructures are shown as follows:

- Substrate temperature: ~ 480 °C
- Pressure: $\sim 5 \times 10^{-8}$ Torr.
- In flux: $\sim 6.0 \times 10^{-5}$ Torr.
- Al flux: $\sim 1.4 \times 10^{-7}$ Torr.
- As flux: $\sim 1.3 \times 10^{-5}$ Torr.

Hall-effect measurements show as-grown electron mobility and sheet concentration at room temperature of the heterostructures as in Table 3.1

	μ [cm^2/Vs]	n_s [cm^{-2}]
InAs/sacrificial/buffer/GaAs(001)	8000	5.3×10^{12}
InAs/GaAs(001)	7100	3.2×10^{12}

Table 3.1: Electron transport properties of InAs heterostructures at room temperature.

After the heterostructure growth, we carried out the separation-bonding process, ELO-VWB, to obtain the InAs/FS systems. The schematic of process is shown in Fig. 3.2, and detailed process flow is described as follows.

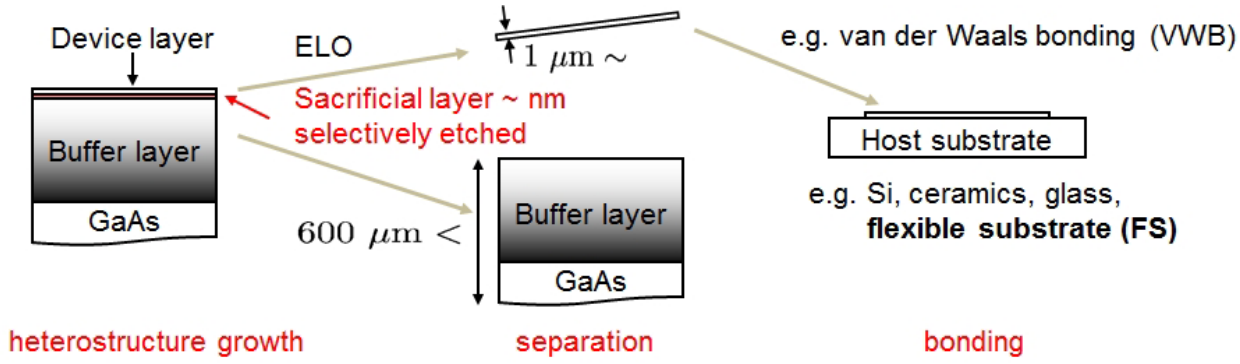

Figure 3.2: Schematic of the ELO-VWB process [72].

- Growth: MBE growth as the above
- Separation: InAs device layer is separated from the growth substrate by a selective etching of the sacrificial layer (epitaxial lift-off, ELO). The device layer will be transferred to the host substrate while the growth substrate can be reused.
- Bonding: InAs device layer is transferred to and bonded on host substrates, for example, by VWB.

The epitaxial lift-off and Van-der-Walls bonding (ELO-VWB) process can be considered as an advanced technology of the heterogeneous integration to obtain high quality device thin films (e.g., InAs films) by eliminating the effects of the large lattice-mismatch between the growth substrate and the device layers. By using this technology, InAs films with very high electron mobilities were obtained on low-k FS, about 10.000 cm^2/Vs for $\sim$ 20 nm films [71, 104], very promising for high-speed device applications. The details of ELO-VWB process to obtain the InAs films on a low-k FS used for our device fabrication are shcematically shown in Fig. 3.3, and the detailed description is followed.

- Sample preparation

The FS was obtained by polyethylene terephthalate (PET) coated by bisazide-rubber (OMR-85), and cut into $\sim$ 1 cm $\times$ 1 cm. The FS surface was made hydrophilic by oxygen-plasma ashing, and dipped in deionized water (DIW). The InAs heterostructure for ELO-VWB was cut into $\sim$ 1mm $\times$ 1 mm, and cleaned by organic solvents (acetone and methanol) for removing organic contaminants. Oxygen-plasma ashing was used to remove organic contaminants on the InAs surface, which were not able to be eliminated by organic solvents. The InAs samples were then cleaned by a H_3PO_4 solution for removing surface oxides, and dipped into DIW.

- Bonding

The cleaned samples were put on a hot plate (HP) of 80-110 ^oC with DIW in order to prevent air bubbles from penetrating into the InAs/FS interface. The high temperatures were used to evaporate the water, and to enhance the strength of the VWB.

- Separation

The InAs heterostructure samples bonded on the FS were dipped into an HF solution (the HF selectively etches the sacrificial layer) for ELO process in a time of hours. The sacrificial layer was selectively etched, and InAs device layers were obtained on FS.

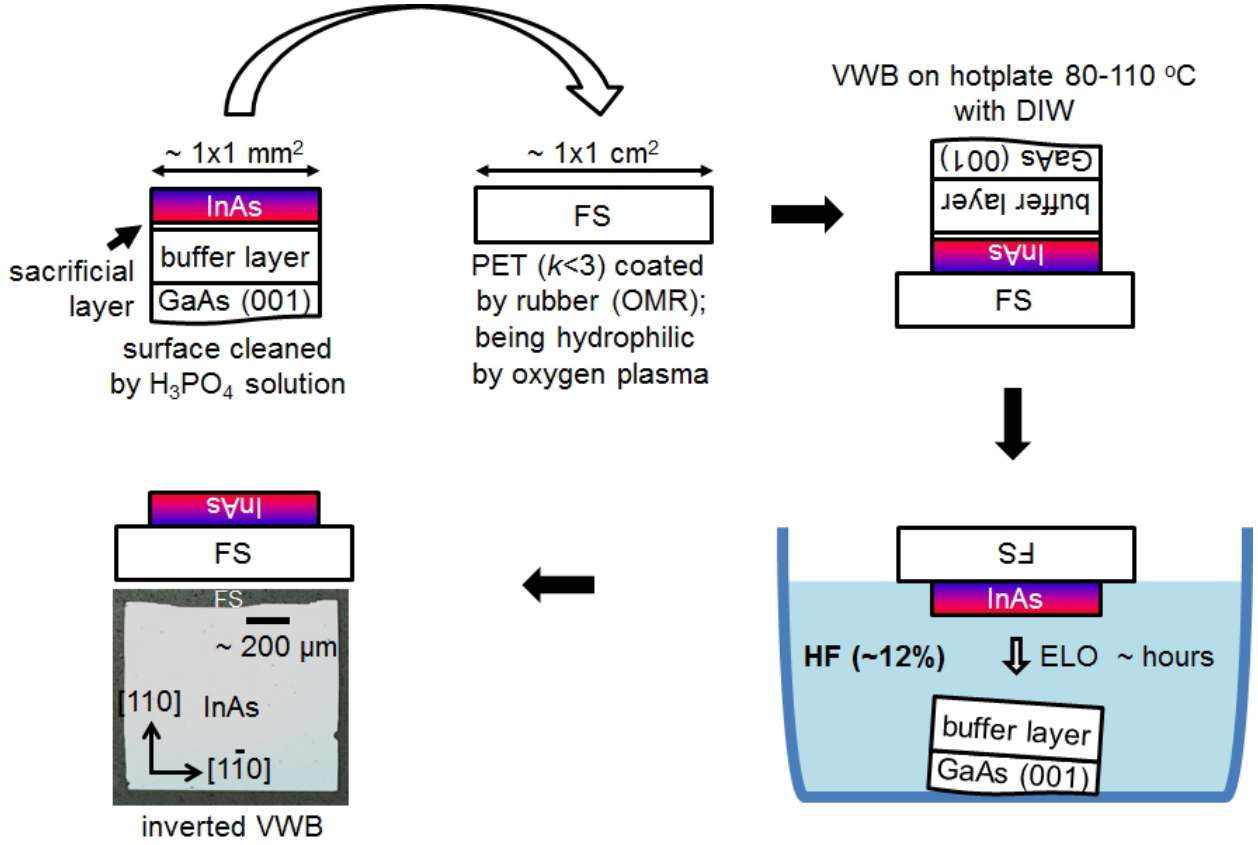

Figure 3.3: Process flow of the separation-bonding process for the InAs/FS.

Using InAs/GaAs(001) and InAs/FS systems, we fabricated 6-terminal Hall-bar devices (50-μm width, 400-μm length, and distance between parallel arms of 200-μm length, as seen in Fig. 3.5) with the current-flowing direction on the [1$\bar{1}$0] crystal direction, by isolation and thinning of the InAs layers, and electrode formation using the conventional photolithography. The details of fabrication process is as follows.

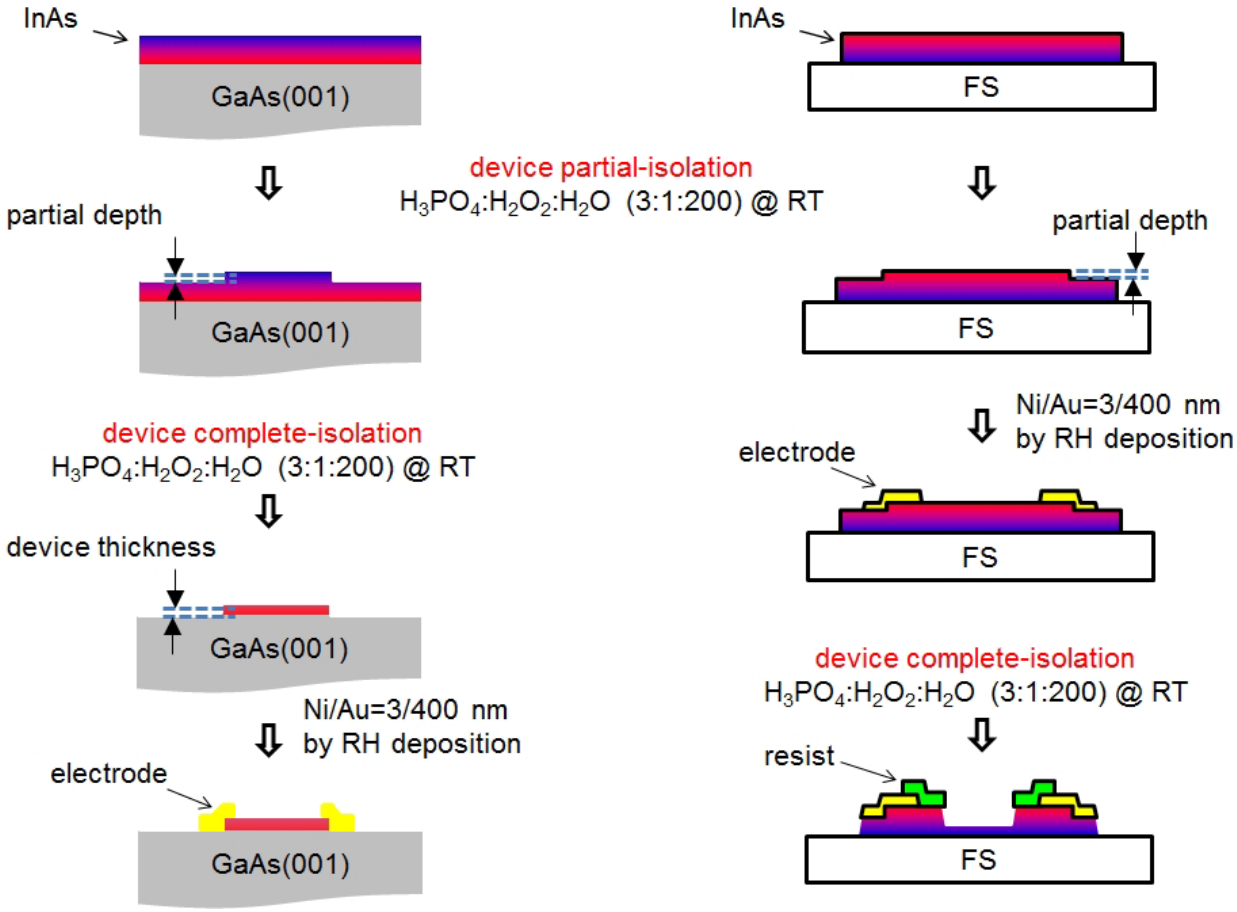

Figure 3.4: Schematic of InAs film device fabrication process.

- Partial isolation

The purpose of partial isolation is to determine the device area as well as the final device InAs layer thickness. The partial isolation included

Surface cleaning: H_3PO_4:H_2O, and DIW to remove surface oxides.

Patterning: Baking on HP at 110 °C, 5 min
Resist coating: TSMR 4000 rpm, 60 sec
Baking on HP at 110 °C, 1.5 min
UV lithography: 12 mW/cm^2, 12 sec
Development: NMD-W 1min, DIW

Etching: H_3PO_4:H_2O_2:H_2O to the device thickness, and DIW. The expected thickness was determined by etching rate and etching time.

After etching, the resists on device mesa was removed by acetone, methanol and DIW. The device thickness after partial isolation was confirmed by laser scanning microscope (LSM), which is considered to be accurate with the thickness in sub-10 nm [104].

- Complete isolation

After the thickness confirmation, the InAs/GaAs(001) devices were isolated by a wet etching. Because of color difference between InAs (blue) and GaAs (violet), the isolation was completed when we realized the color changing around the device mesa. The isolation

was confirmed by IV measurements with mesa. The device film thickness was confirmed again by LSM. The InAs/FS was isolated after the electrode deposition to prevent thin InAs films from damage during the high-temperature electrode formation.

- Electrode formation

Ohmic electrodes were formed by resistance-heating evaporator with Ni and Au sources. The electrode structure is Ni/Au 5/250 nm. The device fabrication process is schematically summarized in the Fig. 3.4.

Hall-bar devices have a channel length $L = 400$ μm and a width $W = 50$ μm. The arms have $L = 300$ μm, $W = 20$ μm, and distance between two arms of 200 μm. Figure 3.5 shows optical images of the fabricated devices with InAs thickness is about 10 nm.

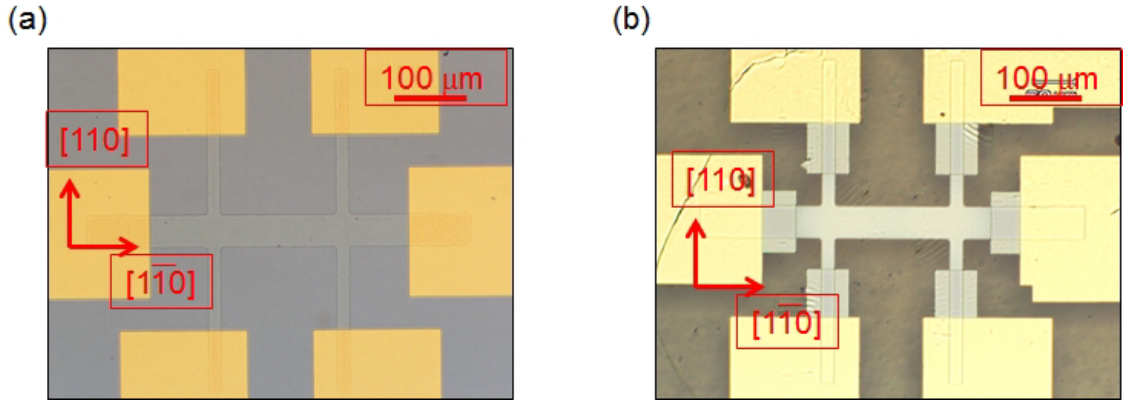

Figure 3.5: Optical image of devices for (a) InAs/GaAs(001) and (b) InAs/FS with InAs thickness ∼10 nm.

3.2 DC characterization of InAs films on low-k flexible substrates or on GaAs(001)

Using the fabricated devices, we firstly obtained electron transport properties of the InAs films by Hall-effect measurements. Figures 3.6 and 3.7 show electron mobility and sheet concentration as functions of the InAs thickness. The thickness dependence of the InAs film transport properties was reported [71, 104]. Hence, in this work, we only consider the regime in which the low-frequency noise measurements were performed.

While the sheet concentration n_s of the InAs/GaAs(001) shows a weak thickness dependence, that of the InAs/FS decreases with decreasing InAs thickness but spreads out in the thin film regime, as observed in Fig. 3.6. The mechanism of the thickness dependence of the electron concentration in the InAs films was reported elsewhere [71]. In contrast, the electron mobility μ shows a clear thickness dependence: the μ monotonically decreases with the decreasing InAs thickness with a rapid decrease at very thin films. The mechanism of the thickness dependence of the electron mobility in the InAs films was reported elsewhere [104]. In the regime of InAs thickness d larger than 15 nm, the electron mobility μ is fitted well by equation

$$\frac{1}{\mu} = \frac{1}{\mu_0} + \frac{1}{ad}, \tag{3.1}$$

where d is the InAs thickness, μ_0 and a are fitting parameters, shown in the Table 3.2.

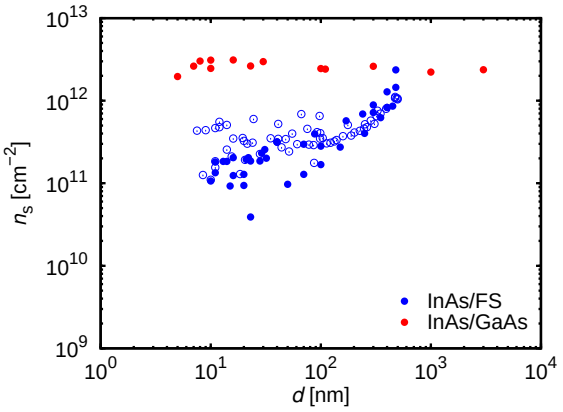

Figure 3.6: The electron sheet concentration n_s as functions of the InAs film thickness d. The solid points belong to the devices used for low-frequency noise measurements.

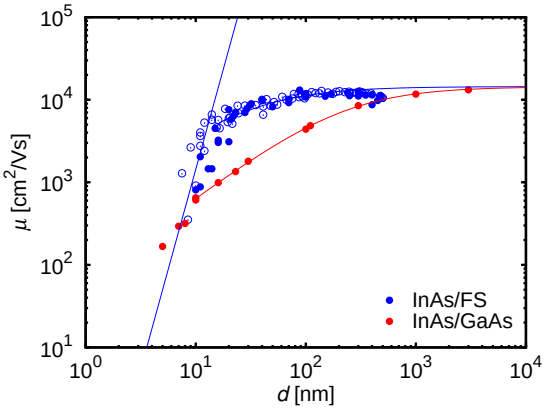

Figure 3.7: The electron mobility μ as functions of the InAs film thickness d. The solid points belong to the devices used for low-frequency noise measurements.

	InAs/FS	InAs/GaAs(001)
μ_0 [cm^2/Vs]	14430	14340
a [cm/Vs]	5.1×10^9	6.6×10^8

Table 3.2: Fitting parameters of the thickness dependence of electron mobility by Eq. 3.1.

In Eq. (3.1), the first term is attributed to the phonon scattering, while the second term is due to Coulomb scattering owing to surface charges. The common μ_0 implies the same phonon scattering mobility for InAs/FS and InAs/GaAs(001), while the difference in a indicates different surface charge conditions. As discussed in [104], the thickness dependence given by Eq. (3.1) was attributed to the Coulomb-scattering mobility with $\mu_C = ad$. We calculated the Coulomb mobility (see Appendix B for the details of the calculation) and obtained

$$\mu_C = \left\{ \frac{4\pi\varepsilon_s^2\hbar^3k^3}{n_{ss}e^3m^{*2}} \right\} d = ad \propto d, \tag{3.2}$$

where ε_s is the semiconductor dielectric constant, k is the wave vector determined by Fermi sphere using values of sheet concentration, n_{ss} is the surface charge density, and m^* is the electron effective mass. The two-dimensional Fermi wave vector $k \equiv k_F$ is calculated by using

$$n_s = 2\frac{\pi {k_F}^2}{(2\pi)^2}. \tag{3.3}$$

From Eq. (3.2) and fitting parameters in Table 3.2, we can evaluate the density of surface charges, which play important roles in both electron transport properties and low-frequency noise characteristics of the InAs film systems. The values of the surface charge density n_{ss} is shown in the Table 3.3.

	InAs/FS	InAs/GaAs(001)
n_s [cm^{-2}]	$\lesssim 2 \times 10^{12}$	~2-3×10^{12}
n_{ss} [cm^{-2}]	$\lesssim 1 \times 10^{13}$	$\sim 8 \times 10^{13}$

Table 3.3: The sheet electron concentration n_s used to calculate wave vector k by Eq. (3.3) and the surface charge density n_{ss} in InAs films obtained by Eq. (3.2).

3.3 Low-frequency noise characterization of InAs films on low-k flexible substrates or on GaAs(001)

3.3.1 Low-frequency noise in InAs films on low-k flexible substrates or on GaAs(001)

After the DC characterization, the low-frequency noise in InAs films was measured by the system having configuration shown Fig. 2.2(a). By changing bias voltage with proper setting of the off-set currents, we obtained the current noise as functions of the frequency f in the range of 1→ 10^4 Hz. In order to determine the off-set current, IV measurements were done to obtain the current I as a function of the bias voltage V, and the off-set currents were gotten as the same as the current obtained by the IV results for the corresponding bias voltages. For the setting of low-noise preamplifier (LNA) sensitivity, we have to follow the trade-off between the lower limit of the measurement system and the device resistance, as discussed in section 2.2.2. The measurement procedures are as follows. Inside the shielding chamber of the probe station, one Ohmic electrode of the device is connected to the LNA with applications of a DC bias voltage and a DC off-set current, while the other Ohmic electrode is grounded. The current noise is amplified by the LNA, whose output is entered to the dynamic signal analyzer (DSA) to obtain the power spectrum density(PSD). Finally, we obtain the current noise with PSD $S_I(f)$ as functions of the frequency f, depending on the current I flowing through the devices.

Figure 3.8 shows low-frequency spectra of the current noise PSD S_I as functions of frequency f for InAs film devices with some InAs film thicknesses as examples. The low-frequency noise with current noise PSD inversely proportional to the frequency $S_I \propto 1/f^\gamma$ ($\gamma \sim 1$) is observed in InAs films at measured frequencies from 1 Hz to ~kHz. The flat behavior at high frequencies in low-current measurements is due to below limitation

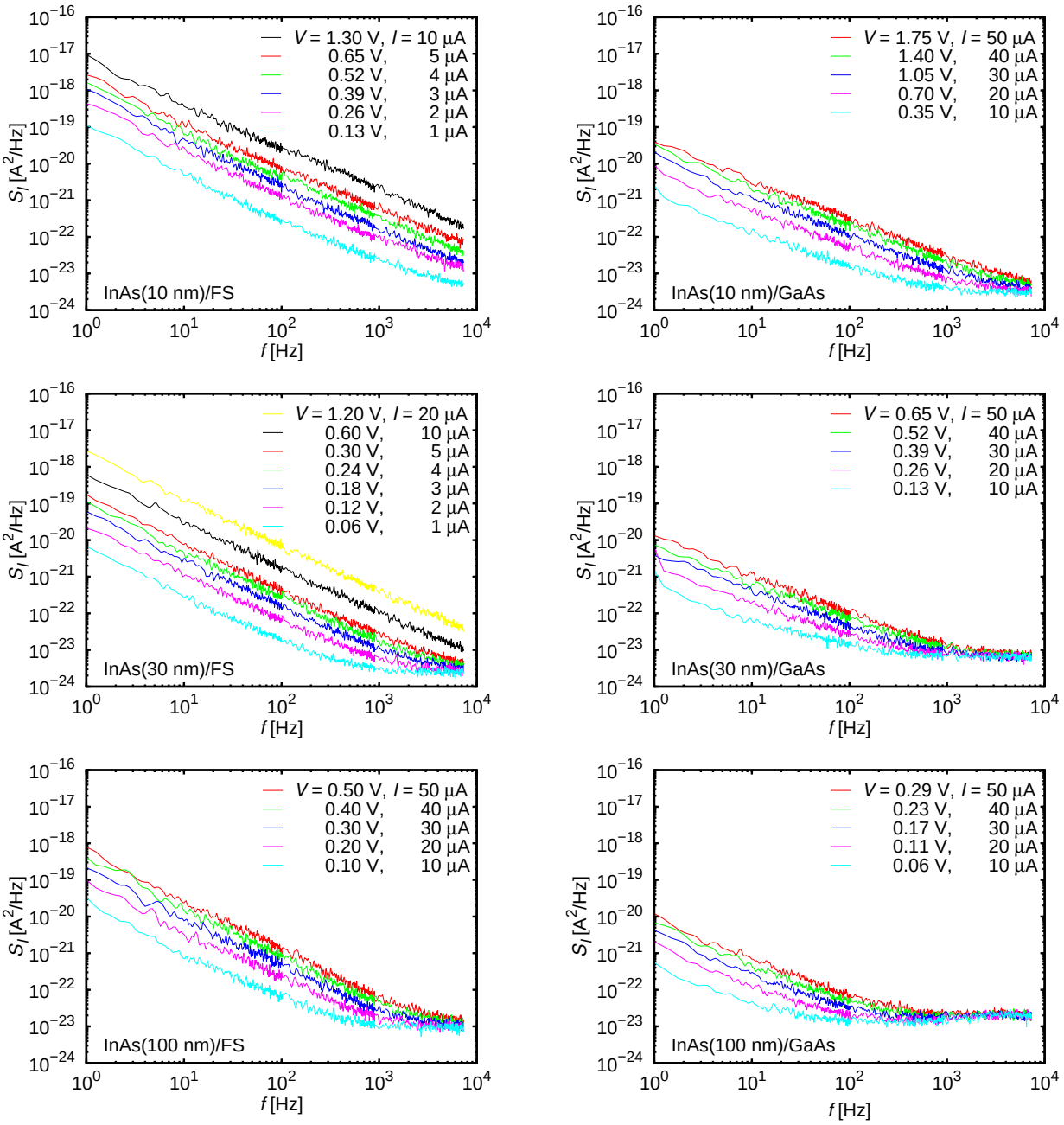

Figure 3.8: Low-frequency spectra of the current noise in InAs films having $L = 400$ μm, $W = 50$ μm with the noise power spectrum density (PSD) S_I as functions of the frequency f.

of the measurement system, which depends on the LNA input impedance, i.e., on the amplifier sensitivity setting used for the measurements. Neither peaks nor bumps are observed, implying no recombination-generation noise due to specific high-density electron traps with a specific time constant in the films.

In order to analyze details of the observed low-frequency noise, we normalized the spectra by the square of current S_I/I^2, and plotted in Fig. 3.9 for S_I/I^2 as functions of f. $S_I/I^2 \propto 1/f$ is observed, and seemingly $S_I/I^2 =$ constant. Figure 3.10 shows the

noise power $S_I f$ as functions of the current I, from which we can confirm that $S_I f \propto I^2$. From the above, we realize that the noise spectra can be expressed by a formula using a constant factor K

$$S_I \simeq \frac{KI^2}{f}, \tag{3.4}$$

where the factor K depends on the InAs film dimensions, i.e, the channel length L, the device width W, and the film thickness d.

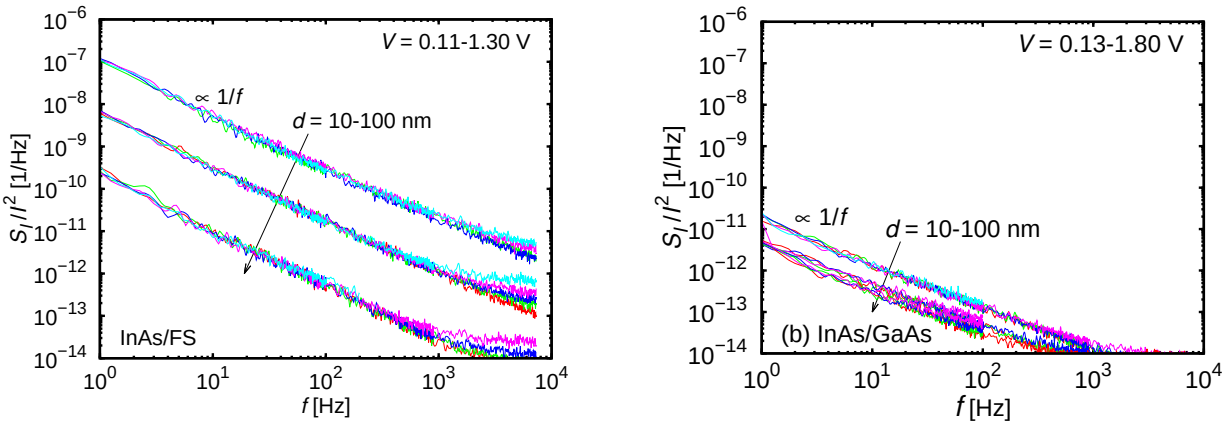

Figure 3.9: The noise spectra normalized by the square of current S_I/I^2 as functions of the frequency f, where d is the InAs thickness.

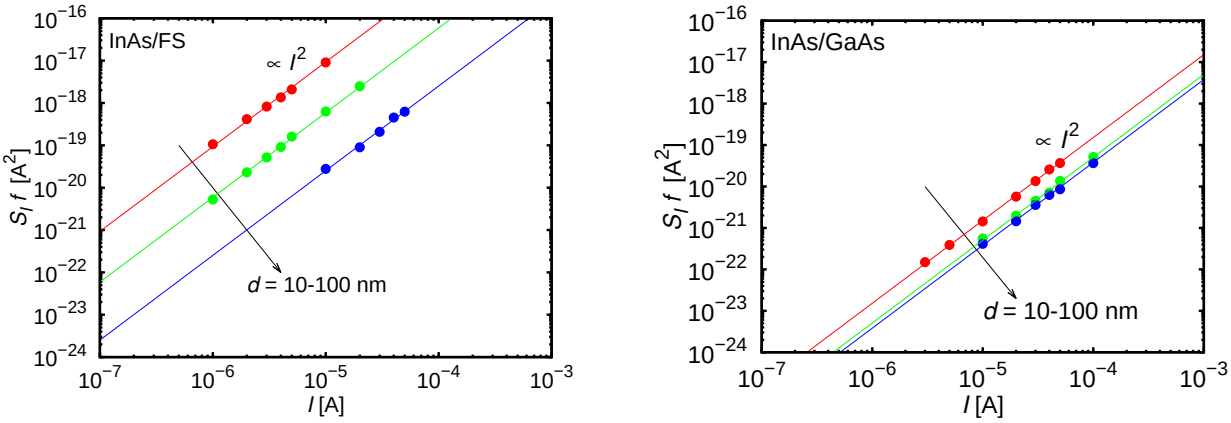

Figure 3.10: The noise power $S_I f$ as functions of the current I, where d is the InAs thickness.

Because the device includes the InAs channel and the contact electrodes, we have to consider the contribution from each part to the total noise of the device. In order to evaluate the contribution of the conduction channel to the total noise power, we consider the electrode contacts and InAs film channel as resistors in series, as schematically shown in Fig. 3.11. For two resistors A and B in series, the voltage V drop on A and B is

$$V = V_{\mathrm{A}} + V_{\mathrm{B}}, \tag{3.5}$$

where $V_{\rm A}$ and $V_{\rm B}$ are the voltage drop on A and B, respectively. The total noise PSD generated is hence given by (see Appendix D)

$$S_V = S_{V_{\rm A}}^{\rm A} + S_{V_{\rm B}}^{\rm B}, \text{ or} \tag{3.6}$$

$$\frac{S_I}{I^2}V^2 = \frac{S_I^{\rm A}}{I^2}{V_{\rm A}}^2 + \frac{S_I^{\rm B}}{I^2}{V_{\rm B}}^2, \tag{3.7}$$

where we used the relation

$$\frac{S_I}{I^2} = \frac{S_V}{V^2}, \tag{3.8}$$

with a notification that this equation is held only for Ohmic regime, where $V \propto I$ (see Appendix D). By applying Ohm's law for the resistance, we have

$$S_I = S_I^{\rm A}\frac{{V_{\rm A}}^2}{V^2} + S_I^{\rm B}\frac{{V_{\rm B}}^2}{V^2} = S_I^{\rm A}\frac{{R_{\rm A}}^2}{(R_{\rm A}+R_{\rm B})^2} + S_I^{\rm B}\frac{{R_{\rm B}}^2}{(R_{\rm A}+R_{\rm B})^2}, \tag{3.9}$$

where $R_{\rm A}$ and $R_{\rm B}$ are the resistance of A and B.

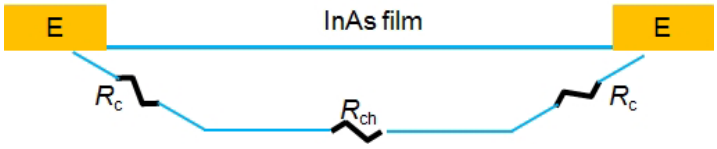

Figure 3.11: The schematic of the conduction path for the InAs film devices with resistors in series: $R_{\rm c}$ of the contact, $R_{\rm ch}$ of the InAs film channel.

Using Eq. (3.9) and Fig. 3.11, we obtain the S_I for the InAs film devices

$$S_I = S_I^{\rm c}\frac{2{R_{\rm c}}^2}{(2R_{\rm c}+R_{\rm ch})^2} + S_I^{\rm ch}\frac{{R_{\rm ch}}^2}{(2R_{\rm c}+R_{\rm ch})^2}, \tag{3.10}$$

where $S_I^{\rm c}$ is the current noise PSD generated by one contact of resistance

$$R_{\rm c} = \frac{r_{\rm c}}{W}, \tag{3.11}$$

where $r_{\rm c}$ is the specific contact resistance in Ω·mm; and $S_I^{\rm ch}$ is the current noise PSD generated by the InAs film channel of resistance

$$R_{\rm ch} = r_{\rm s}\frac{L}{W}, \tag{3.12}$$

where $r_{\rm s}$ is sheet resistance obtained by IV measurement (in Hall-effect measurements) in relation with electron μ and sheet concentration $n_{\rm s}$

$$r_{\rm s} = \frac{1}{en_{\rm s}\mu}. \tag{3.13}$$

The factor K is obtained from Eq. (3.10)

$$\begin{aligned} K &= \frac{S_I}{I^2}f \\ &= K_{\rm c}\frac{2{R_{\rm c}}^2}{(2R_{\rm c}+R_{\rm ch})^2} + K_{\rm ch}\frac{{R_{\rm ch}}^2}{(2R_{\rm c}+R_{\rm ch})^2} \end{aligned} \tag{3.14}$$

where K_c, K_{ch} are the factors for the contact and InAs channel, respectively. The latter is given by Hooge model

$$K_{ch} = \frac{\alpha}{N} = \frac{\alpha}{n_s LW}, \tag{3.15}$$

where α is the Hooge parameter and N is the total carrier number in the InAs film channel. We can combine Eqs. (3.11-3.15) as

$$KW = \frac{(K_c W/2) + (\alpha/n_s)(r_s/2r_c)^2 L}{[1 + (r_s/2r_c)L]^2}. \tag{3.16}$$

From this equation, we realize that the InAs channel dominates the total noise power when $(K_c W/2) \ll (\alpha/n_s)(r_s/2r_c)^2 L$ and $1 \ll (r_s/2r_c)L]^2$, i.e., the contacts give negligible contributions to both the noise power and the device resistance. In that case

$$KW \simeq \frac{\alpha}{n_s L} \propto \frac{1}{L}. \tag{3.17}$$

On the other hand, when the contact dominates the total noise power, $(K_c W/2) \gg (\alpha/n_s)(r_s/2r_c)^2 L$ and $1 \gg (r_s/2r_c)L]^2$,

$$KW \simeq K_c W/2 = constant. \tag{3.18}$$

These limits of the L-dependence of KW will identify whenever the contact electrodes or the conducting channel dominates the current noise in the InAs film devices.

We carried out measurements with InAs films having the same thickness but different dimensions. A plot of KW as functions of L was shown in Fig. 3.12 with fitting lines using Eq. (3.17). We realized that the Eq. (3.17) is held for all films with long range of L, e.g., very thin InAs films on GaAs(001), indicating a negligible contribution of the contacts to the current noise in the InAs film devices.

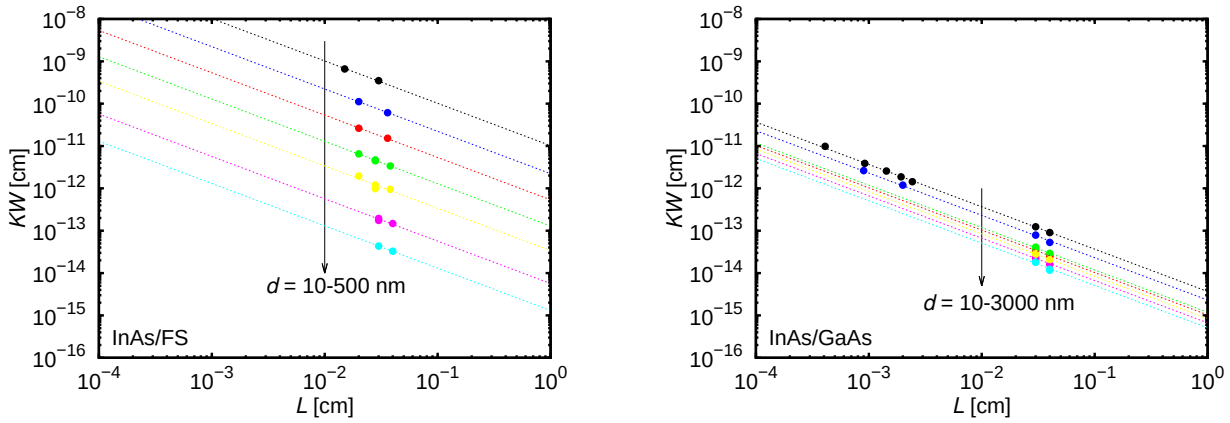

Figure 3.12: The factor KW as functions of the channel length L of the InAs film devices. The lines are fitting lines using Eq. (3.17).

In addition, we investigated the factor K as functions of the total electron number N in the InAs channel, as shown in Fig. 3.13 from which we can confirm $K \propto N = n_s LW$, indicating that the Eq. (3.17) is held. Hence, the Hooge parameter can be calculated by

$$\alpha = K_{ch} N \simeq KN = K n_s LW. \tag{3.19}$$

This means that Hooge parameter α is a characteristic of the noise in the film, and a constant for films with a fixed thickness.

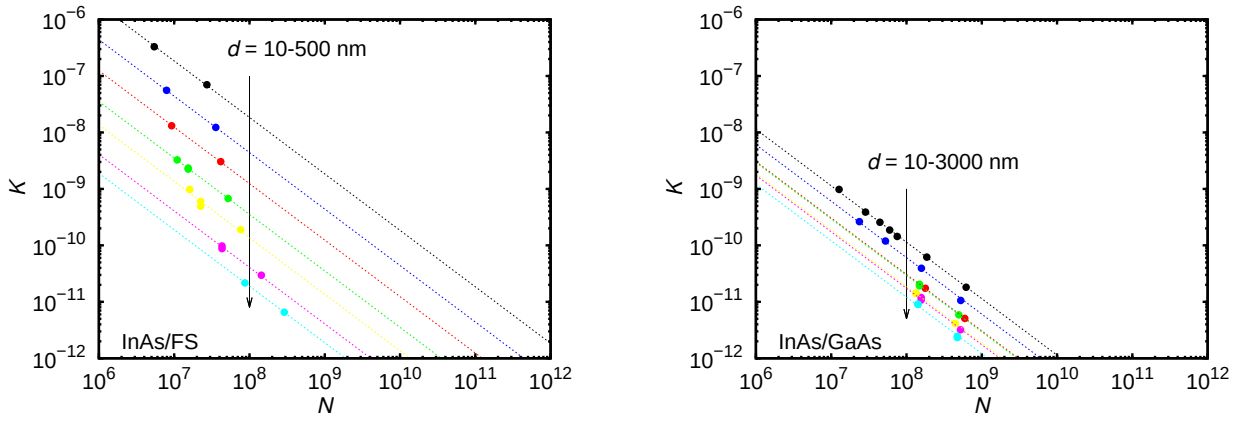

Figure 3.13: The factor K as functions of the total electron number N of the InAs film devices.

The Hooge parameter α as functions of the InAs film thickness and transport properties are shown in Fig. 3.14. We can see that almost the films have Hooge parameter $\alpha > \alpha_0$, here $\alpha_0 = 2 \times 10^{-3}$ is the Hooge universal constant [32, 33]. The large values of α suggest that the observed low-frequency noise in the InAs films is out of the Hooge noise model, which considers that phonon-scattering-limited mobility fluctuations are the origin of the low-frequency noise, leading to Hooge parameters equal or less than $\alpha_0 = 2 \times 10^{-3}$ [33]. Moreover, the thickness dependence of the α shows different tendencies for different thickness region. This behavior may relate to thickness dependence of the electron mobility in InAs films, which was reported elsewhere [104]. The above results require a new explanation of the observed low-frequency noise.

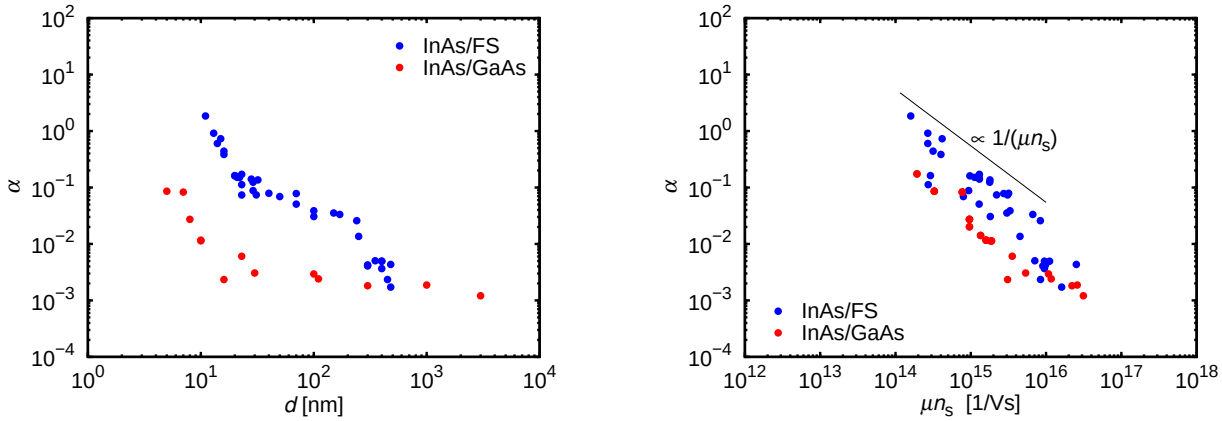

Figure 3.14: The Hooge parameter α as functions of the films thickness and of a product of transport properties μn_s.

3.3.2 Low-frequency noise model

Current fluctuation in homogeneous films

To clarify the mechanism of the observed low-frequency noise in the InAs films, we first consider a current I flowing through a thin film of length L and width W under a bias voltage V

$$I = \sigma_{\rm s}\frac{W}{L}V = n_{\rm s}(LW)e\mu\frac{V}{L^2} = e\frac{V}{L^2}N\mu = e\frac{V}{L^2}\sum_{\rm i=1}^{N}\mu_{\rm i}, \tag{3.20}$$

where $\sigma_{\rm s}$ is the sheet conductivity, $n_{\rm s}$ is the sheet carrier concentration, $N = LWn_{\rm s}$ is the total carrier number in the conduction channel, μ is the measured (average) carrier mobility, and $\mu_{\rm i}$ is mobility of the $i^{\rm th}$ individual carrier. By using Burgess theorem [105], we obtain the averages

$$\begin{aligned}
\langle\langle\sum_{i=1}^{N}\mu_i\rangle\rangle &= \langle\mu\rangle\langle N\rangle \\
\langle\langle\Big(\sum_{i=1}^{N}\mu_i\Big)^2\rangle\rangle &= \langle\langle\sum_{i=1}^{N}\mu_i^2\rangle\rangle + \langle\langle\sum_{i\neq j}^{N}\mu_i\mu_j\rangle\rangle = \langle\mu^2\rangle\langle N\rangle + \langle\mu\rangle^2\langle N^2-N\rangle,
\end{aligned} \tag{3.21}$$

where, the symbol $\langle\langle ...\rangle\rangle$ means taking average on two variables, here are μ and N ones. Hence, the current fluctuations, which will give power spectrum density of the measured current noise, are given by

$$\begin{aligned}
(\delta I)^2 &= \langle I^2\rangle - \langle I\rangle^2 \\
&= \left(e\frac{V}{L^2}\right)^2[\langle N\rangle(\delta\mu)^2 + \langle\mu\rangle^2(\delta N)^2].
\end{aligned} \tag{3.22}$$

By using Eq. (1.27) and (3.22), we normalize the fluctuations by square of the current I^2

$$\frac{(\delta I)^2}{I^2} = \frac{1}{\langle N\rangle}\frac{(\delta\mu)^2}{\langle\mu\rangle^2} + \frac{(\delta N)^2}{\langle N\rangle^2}, \tag{3.23}$$

which leads to PSD of the current noise $S_I \propto (\delta I)^2$ by

$$\frac{S_I}{I^2} \propto \frac{1}{\langle N\rangle}\left(\frac{(\delta\mu)^2}{\langle\mu\rangle^2} + \frac{(\delta N)^2}{\langle N\rangle}\right). \tag{3.24}$$

In the Eqs. (3.23-3.24), we obtain the factor $1/\langle N\rangle$ in the first term with the mobility fluctuations, which cannot be realized by normal calculation of the current fluctuation based on small fluctuation approximation by differentiating Eq. (3.20). Moreover, in the calculation of Eqs. (3.23-3.24), we do not need any assumption of independence of variables when taking the average. Hence, these advantages make Eqs. (3.23-3.24) the most general expression of the current noise PSD in homogeneous films. The current noise simultaneously comes from two origins: carrier-mobility fluctuations $(\delta\mu)^2$ (denoted by $\Delta\mu$) and carrier-number fluctuations $(\delta N)^2$ (denoted by ΔN), but while the ΔN-caused noise is independent of carrier mobility, the $\Delta\mu$-caused noise is inversely proportional to

carrier number. In the case of absence of the ΔN-caused noise, Eq. (3.24) becomes the Hooge empirical equation with a definition of Hooge parameter

$$\alpha_{\mathrm{H}} = \frac{(\delta\mu)^2}{\langle\mu\rangle^2}. \tag{3.25}$$

More general, from definition of S_I (the noise power in unit frequency bandwidth), we can obtain normalized noise power

$$\frac{(\delta I)^2}{I^2} = \int_{f_\ell}^{f_{\mathrm{h}}} \frac{S_I}{I^2}\mathrm{d}f = \int_{f_\ell}^{f_{\mathrm{h}}} \frac{\alpha}{Nf}\mathrm{d}f = \frac{\alpha}{N}\ln\frac{f_{\mathrm{h}}}{f_\ell}, \tag{3.26}$$

where f_{h} and f_ℓ are the high and low limits of $1/f$ behavior [17, 26], and Hooge parameter

$$\alpha = \frac{1}{\ln(f_{\mathrm{h}}/f_\ell)}\left(\frac{(\delta\mu)^2}{\mu^2} + \frac{(\delta N)^2}{N}\right) = \frac{1}{\ln(f_{\mathrm{h}}/f_\ell)}(\alpha_\mu + \alpha_N), \tag{3.27}$$

where, $\alpha_\mu = (\delta\mu)^2/\langle\mu\rangle^2$, and $\alpha_N = (\delta N)^2/\langle N\rangle^2$. This is the general expression of Hooge parameter in homogeneous samples, and can be extended to non-homogeneous samples such as field-effect transistors by substituting the averages by local values. The Hooge parameter given by Eq. (3.27) originates from two origins: carrier-mobility fluctuations α_μ and carrier-number fluctuations α_N. One can realize that α_μ and α_N are independent of carrier number and mobility, respectively; this property is different from the normalized noise power S_I/I^2 as discussed above. Hence, we can consider the noise origin through α_μ and α_N independently. To realize more details of the Eq. (3.27), and take insights into observed low-frequency noise in our experiments, we consider the carrier-number and mobility fluctuations for the case of InAs films on host substrates. In the InAs film systems, there exist interface states at the film surfaces. These states can be not only scattering centers governing the electron mobility such as by Coulombic interactions but also trapping centers causing electron number fluctuations resulting in low-frequency noise in the films.

Mobility fluctuation

Figure 3.15 shows the Hooge parameter as functions of the mobility μ. While α varies independently of μ for thick InAs films on FS ($d \gtrsim 20$ nm, corresponding to the high mobility regime in which μ weakly changes), $\alpha \propto 1/\mu$ for InAs/FS with $d \lesssim 20$ nm and InAs/GaAs. The dependence $\alpha \propto 1/\mu$ suggests that the current noise can be related to mobility fluctuations.

The total mobility of free electrons in the films can be formulated by Matthiessen rule

$$\frac{1}{\mu} = \frac{1}{\mu_0} + \frac{1}{\mu_{\mathrm{C}}} = \frac{1}{\mu_{\mathrm{ph}}} + \frac{1}{\mu_{\mathrm{m}}} + \frac{1}{\mu_{\mathrm{C}}} \tag{3.28}$$

where, μ_{ph} is the mobility caused by phonon scattering, μ_{m} is other components contributing to μ_0, and μ_{C} is the mobility caused by Coulomb scattering due to the interface charges. Considering the fluctuation of μ_{ph} and μ_{C} (μ_{m} does not have sample dependence, suggesting no fluctuation), Hooge parameter dominated by the mobility fluctuation is

$$\alpha \simeq \frac{(\delta\mu)^2}{\mu^2} = \frac{\mu^2}{{\mu_{\mathrm{ph}}}^2}\frac{(\delta\mu_{\mathrm{ph}})^2}{{\mu_{\mathrm{ph}}}^2} + \frac{\mu^2}{{\mu_{\mathrm{C}}}^2}\frac{(\delta\mu_{\mathrm{C}})^2}{{\mu_{\mathrm{C}}}^2} \tag{3.29}$$

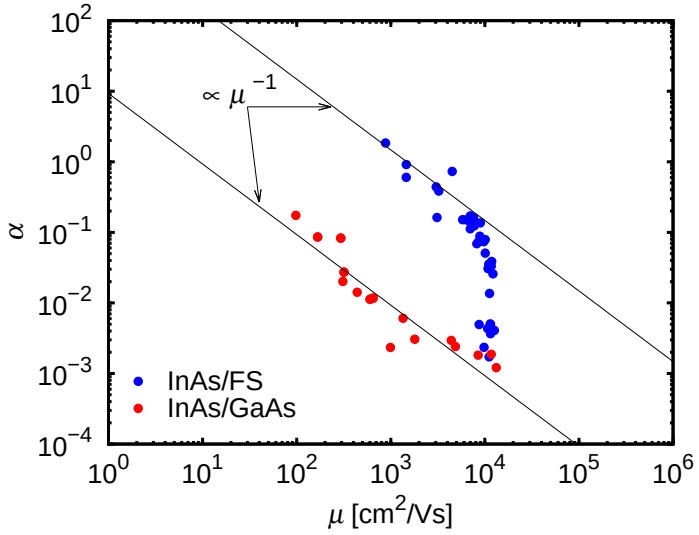

Figure 3.15: The Hooge parameter α as functions of the InAs electron mobility μ.

with an assumption of the independence

$$\langle \mu_{\rm ph} \cdot \mu_{\rm C} \rangle = \langle \mu_{\rm ph} \rangle \langle \mu_{\rm C} \rangle. \tag{3.30}$$

From Eq. (3.29), we can realize that when phonon scattering dominates the total mobility $\mu \simeq \mu_{\rm ph}$, the Hooge parameter is given by

$$\alpha_\mu = \frac{\mu^2}{{\mu_{\rm ph}}^2} \frac{(\delta\mu_{\rm ph})^2}{{\mu_{\rm ph}}^2} \simeq \frac{(\delta\mu_{\rm ph})^2}{{\mu_{\rm ph}}^2} \equiv \alpha_{\rm H}, \tag{3.31}$$

where $\alpha_{\rm H}$ is the Hooge universal constant; when non-phonon scatterings such as Coulomb scattering dominate the total mobility $\mu \simeq \mu_{\rm C}$, the Hooge parameter is given by

$$\alpha_\mu = \frac{\mu^2}{{\mu_{\rm C}}^2} \frac{(\delta\mu_{\rm C})^2}{{\mu_{\rm C}}^2} \simeq \frac{(\delta\mu_{\rm C})^2}{{\mu_{\rm C}}^2} \equiv \alpha_{\rm C}, \tag{3.32}$$

where $\alpha_{\rm C}$ is the Hooge parameter governed by $\mu_{\rm C}$, depending on the films' properties. For our observation, we consider

$$\frac{\mu^2}{{\mu_{\rm ph}}^2} \frac{(\delta\mu_{\rm ph})^2}{{\mu_{\rm ph}}^2} = \frac{\mu^2}{{\mu_{\rm ph}}^2} \alpha_{\rm H} = \frac{\mu^2}{{\mu_{\rm ph}}^2} \times 2 \times 10^{-3} \ll 10^{-3} \tag{3.33}$$

$$\Rightarrow \alpha \simeq \frac{\mu^2}{{\mu_{\rm C}}^2} \frac{(\delta\mu_{\rm C})^2}{{\mu_{\rm C}}^2} \text{ when } \alpha > 10^{-3} \tag{3.34}$$

Equation (3.34) means that the fluctuations in Coulomb mobility dominate the current fluctuations in the InAs films. Since

$$\mu_{\rm C} = \frac{4\pi\varepsilon_{\rm s}^2 \hbar^3 k^3}{n_{\rm ss} e^3 m^{*2}} d, \tag{3.35}$$

we can expect that the fluctuation of $\mu_{\rm C}$ is governed by the fluctuation of the thickness d

$$\alpha \simeq \frac{\mu^2}{{\mu_{\rm C}}^2} \frac{(\delta\mu_{\rm C})^2}{{\mu_{\rm C}}^2} = \frac{\mu^2}{{\mu_{\rm C}}^2} \frac{(\delta d)^2}{d^2}. \tag{3.36}$$

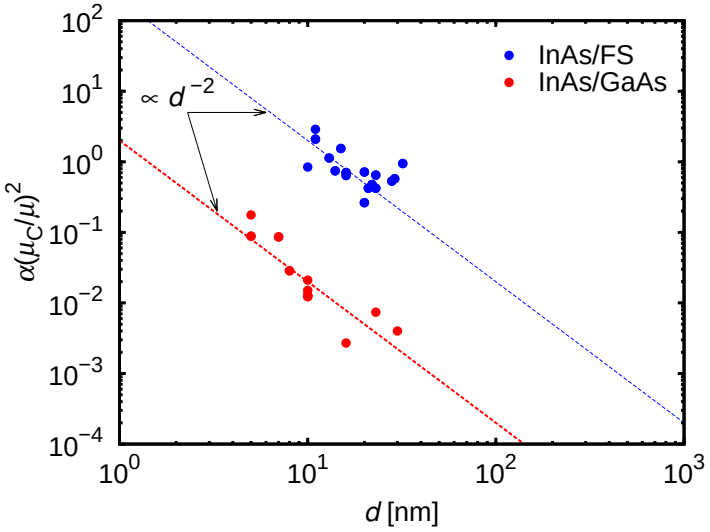

Figure 3.16: The Hooge parameter α as functions of the InAs electron mobility μ.

In order to confirm Eq. (3.36), we plot $\alpha(\mu_C/\mu)^2$ as a functions of d as shown in Fig. 3.16. We observe for the thin regimes of the InAs films that

$$\alpha\frac{{\mu_C}^2}{\mu^2} \propto \frac{1}{d^2}, \tag{3.37}$$

indicating

$$(\delta d)^2 \simeq \text{constant}. \tag{3.38}$$

We hence realize that the experimental data for very thin films are well explained by a mobility fluctuation due to constant thickness fluctuations. Hence, we conclude that the current noise with relation of $\alpha \propto \mu^{-1}$ in thin InAs films is due to mobility fluctuation caused by the fluctuations in InAs film thickness.

Carrier-number fluctuation

The carrier number in conduction channel can fluctuate by exchanging carriers with states out of the channel such as interface/surface states. However, the total carrier number in the film is a constant, we have

$$\begin{aligned} N + N_i &= \text{constant} \\ (\delta N)^2 &= (\delta N_i)^2, \end{aligned} \tag{3.39}$$

where N is the carrier number in the conduction channel, N_i is the carrier number out of the conduction channel such as being kept in interface states. There are only two possibilities of interface states: occupied by an electron or not. The occupation probability of one interface state, or average number of electrons in one state is hence given by Fermi-Dirac distribution

$$P = \frac{1}{e^{\beta(E-E_F)}+1}, \tag{3.40}$$

where E and $E_{\rm F}$ are the electron and Fermi level energy, respectively; $\beta = k_{\rm B}T$ with Boltzmann constant $k_{\rm B}$ and temperature T. The fluctuation of carrier number in the channel is equal to that of the interface state occupation given by (see Appendix E)

$$(\delta N)^2 = LW \int P(1-P) D_{\rm i} {\rm d}E \simeq LW D_{\rm i} k_{\rm B} T. \tag{3.41}$$

Hence, the Hooge parameter given by the carrier-number fluctuation is

$$\alpha_N = k_{\rm B} T \frac{D_{\rm i}}{n_{\rm s}} \propto {n_{\rm s}}^{-1}, \tag{3.42}$$

as observed in Fig. 3.17 for a regime of InAs/FS.

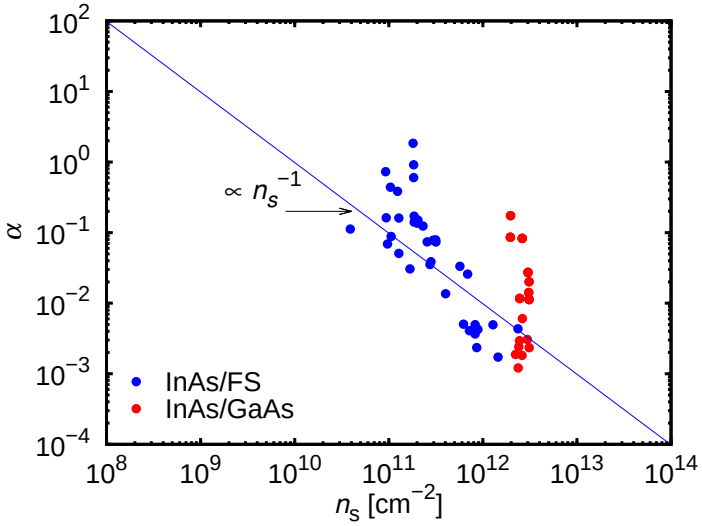

Figure 3.17: The Hooge parameter α as functions of the InAs electron sheet concentration $n_{\rm s}$.

In conclusion, when the carrier-number fluctuation dominates the noise, the Hooge parameter is inversely proportional to the sheet carrier concentration as discussed in Eq. (3.42), and shown in Fig. 3.17 for InAs/FS, indicating that the current noise in the films is generated by electron-number fluctuations due to electron trapping/detraping at the InAs/FS interface states. From experimental data, we obtained an interface state density $D_{\rm i} \sim 1 \times 10^{12}$ cm^{-2}eV^{-1} for InAs/FS, consistent with the calculation of Coulomb scattering with mobility μ as shown in previous discussion on the DC characterization. The same origin of both the low-frequency noise and electron scattering in InAs/FS suggests a correlation between the Hooge parameter α and the mobility μ as in Fig. 3.15.

3.4 Summary

We investigated low-frequency noise in InAs films. As a result, we clarified the $1/f$ noise in the films with various behaviors. For InAs/FS with thickness $d \gtrsim 20$ nm, where μ weakly changes, $\alpha \propto {n_{\rm s}}^{-1}$ is observed and attributed to the electron-number fluctuation $(\delta N)^2 \sim LWD_{\rm i}k_{\rm B}T$, where the interface state density $D_{\rm i} \sim 10^{12}$ cm^{-2}eV^{-1} is obtained from the data, being consistent with the Coulomb-scattering mobility. For InAs/FS with $d \lesssim 20$ nm and InAs/GaAs(001), where $n_{\rm s}$ weakly changes, $\alpha \propto \mu^{-1}$ is observed, which can be related to the mobility fluctuation due to fluctuations in the InAs film thickness.

Chapter 4

Low-frequency noise in AlGaN/GaN heterostructure

4.1 Fabrication of AlGaN/GaN heterostructure devices

AlGaN/GaN devices were fabricated by using $Al_{0.27}Ga_{0.73}N$(30 nm)/GaN(3000 nm) heterostructures obtained by metal-organic vapor phase epitaxy on sapphire(0001). The schematic of the heterostructure cross-section is shown in the Fig. 4.1. Hall-effect measurements of the heterostructure show an as-grown electron mobility of 1200 cm^2/Vs and a sheet electron concentration of 1.2×10^{12} cm^{-2} at room temperature.

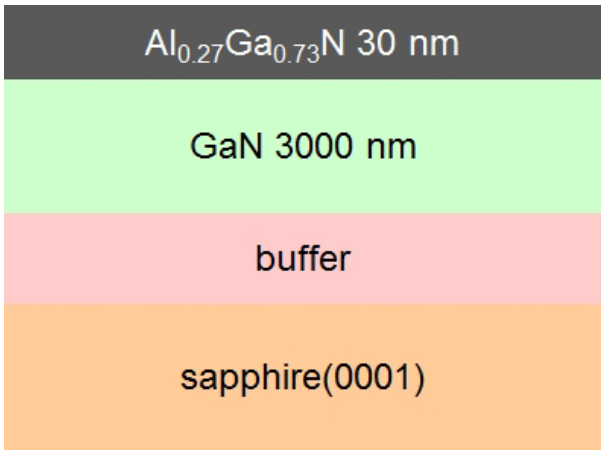

Figure 4.1: Schematic of the AlGaN/GaN heterostructure.

By using the $Al_{0.27}Ga_{0.73}N$(30 nm)/GaN(3000 nm) heterostructures, AlGaN/GaN devices were fabricated. The device fabrication process flow is schematically shown in Fig. 4.2 for metal-insulator-semiconductor (MIS) structures and Schottky structures, which were fabricated simultaneously. The AlGaN/GaN devices include heterojunction field-effect transistors (HFETs) and ungated two-terminal devices obtained on the same wafer. The MIS devices used AlN films, which were deposited by RF sputtering, as the insulator layer. The details of the fabrication process are as follows.

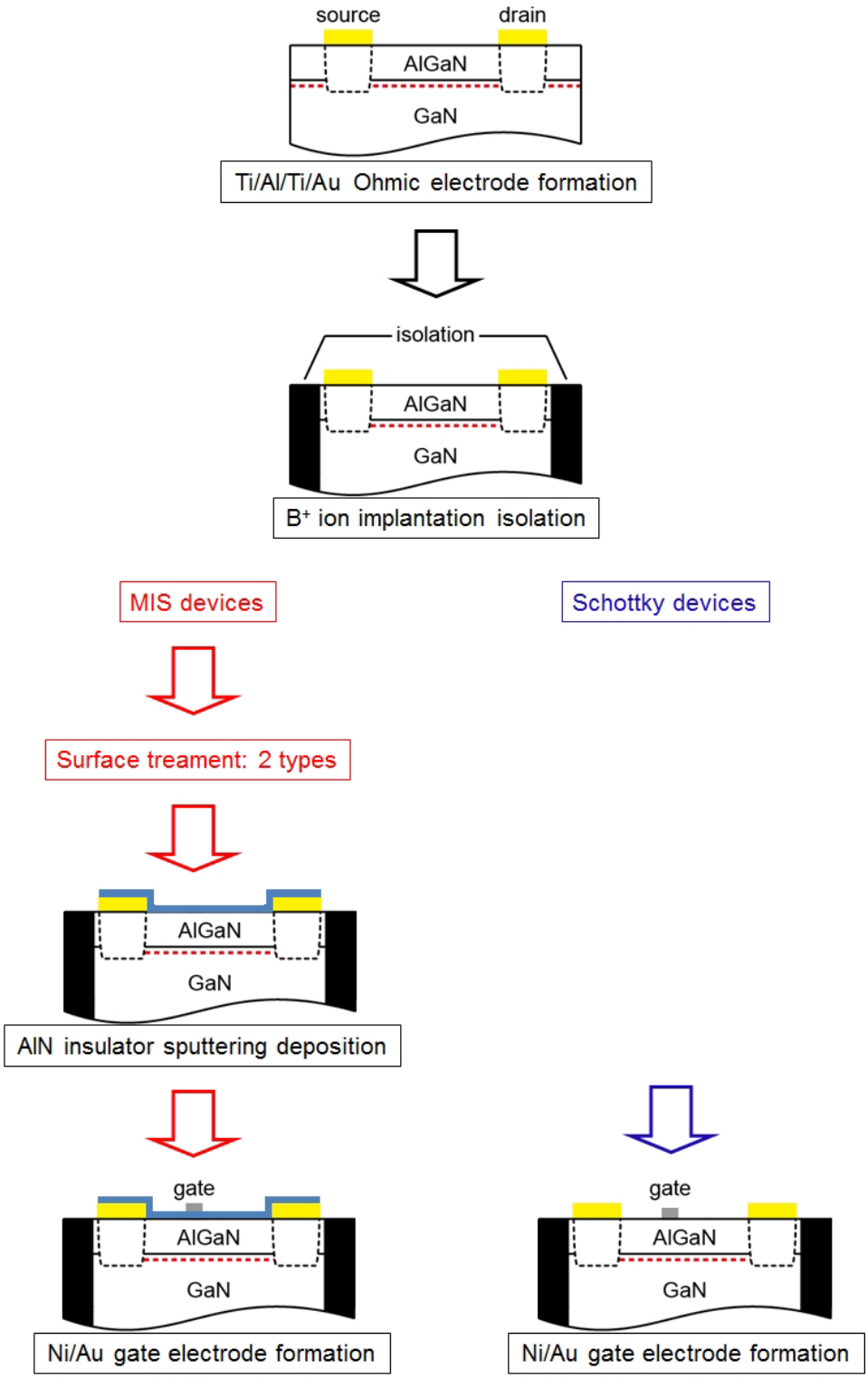

Figure 4.2: Fabrication process flow of AlGaN/GaN heterostructure devices.

- Marker formation

Marker for electron-beam (EB) lithography patterning was firstly formed on the AlGaN/GaN heterostructure, by using UV lithography and EB evaporator. The receipt for

the marker formation is shown in the Table 4.1.

Step	Content
surface treatment	acetone, methanol, DIW 3 min each
	O_2 plasma ashing 50 Pa 10 W 4 min
	Semico-clean 5 min, DIW 3 min
	baking 110^{o}C 3 min
resist coating	LOL2000 (3000 rpm, 60 s), baking (180^{o}C 180 s)
	TSMR-8900 (4000 rpm, 60 s), baking (110^{o}C 90 s)
patterning	exposure $\sim$ 12 mW/cm^2(405 nm) 6.2 s
	development NMD-W (60 s), DIW (180 s)
surface treatment	O_2 plasma ashing 50 Pa 10 W 10 s
	Semico-clean 5 min, DIW 3 min
deposition	Ti/Au 10/150 nm
lift-off	1165 at 60^{o}C
	acetone, methanol, DIW 3 min each

Table 4.1: Marker formation process for AlGaN/GaN heterostructure devices.

- Ohmic electrode formation
Ohmic electrodes were formed with process flow shown in Fig. 4.3.

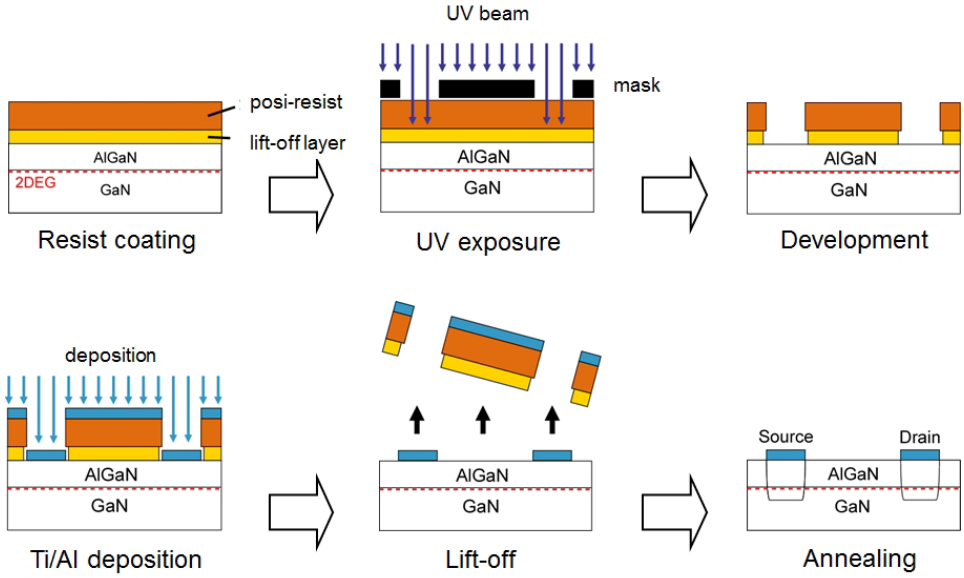

Figure 4.3: Schematic of Ohmic electrode formation process for AlGaN/GaN heterostructure devices.

A surface treatment was firstly carried out to clean the sample surface (by organic solution) and remove the oxide layer on the semiconductor surface (by semico-clean solution), and then followed by resist coating. The resists used were positive resists, which become soluble to the resist developers such as NMD-W when the resists are exposed by light. The first layer is LOL2000, which plays a role as lift-off layer that will be removed during lift-off process in 1165 solution. The second layer is TSMR8900, which plays a role of photoresist. The photoresist was patterned by an electrode mask and a photolithography system, the UV source used is an Hg source having wavelength of 405 nm and power

of 12 mW/cm^2. After development to create an electrode pattern, a surface treatment was carried out to clean the electrode region before deposition, this can reduce the contact resistance (also, on-resistance of devices). After the electrode formation by electron beam (EB) evaporator, the wafer was annealed at 575 °C in N_2 ambient to make the Ohmic contact between electrode and GaN layer (more accurately, to two-dimensional electron gas (2DEG) in GaN to form the channel connection for the current flow). The process receipt is summarized as in the Table 4.2.

Step	Content
surface treatment	acetone, methanol, DIW 3 min each
	O_2 plasma ashing 50 Pa 10 W 4 min
	Semico-clean 5 min, DIW 3 min
	baking 110^{o}C 3 min
resist coating	LOL2000 (3000 rpm, 60 s), baking (180^{o}C 180 s)
	TSMR-8900 (4000 rpm, 60 s), baking (110^{o}C 90 s)
patterning	exposure $\sim$ 12 mW/cm^2(405 nm) 6.2 s
	development NMD-W (60 s), DIW (180 s)
surface treatment	O_2 plasma ashing 50 Pa 10 W 10 s
	Semico-clean 5 min, DIW 3 min
deposition	Ti/Au 10/200 nm
lift-off	1165 at 60^{o}C
	acetone, methanol, DIW 3 min each
annealing	N_2 atmosphere 575^{o}C 5 min

Table 4.2: Ohmic electrode formation process for AlGaN/GaN heterostructure devices.

- Device isolation

Devices were isolated by using B^+ ion implantation with process flow shown in Fig. 4.4. The purpose of ion implantation is to isolate the device from the substrate by implant

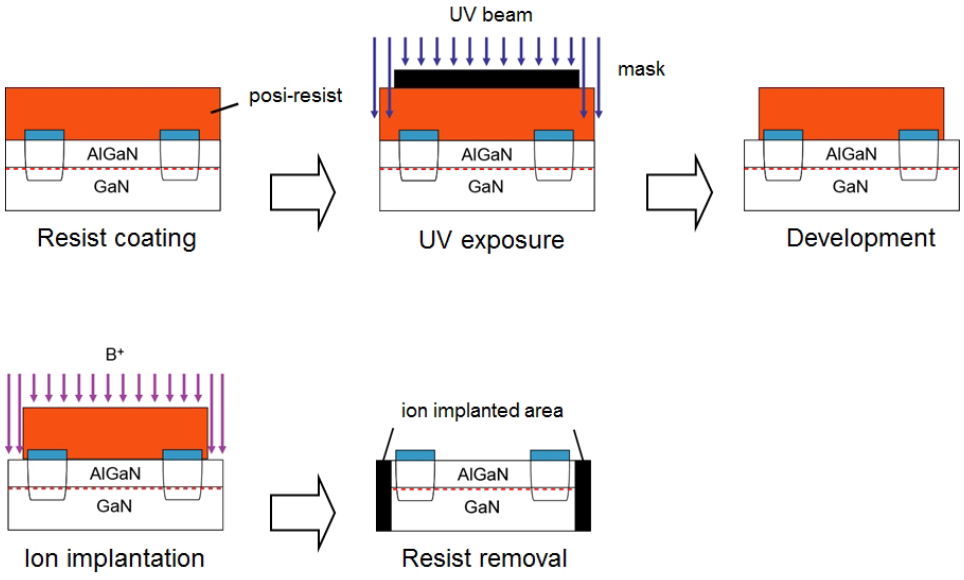

Figure 4.4: Schematic of isolation process for the AlGaN/GaN heterostructure devices.

high-energy ion beams (boron ion source was used) into around the device (determined by a photo resist mask), the ion beams cause damage in implanted region, and the device will be isolated. The receipt of process flow is summarized as in the Table 4.3.

Step	Content
surface treatment	acetone, methanol, DIW 3 min each
	O_2 plasma ashing 50 Pa 10 W 4 min
resist coating	LOL2000 (3000 rpm, 60 s), baking (180^{o}C 180 s)
	TSMR-8900 (4000 rpm, 60 s), baking (110^{o}C 90 s)
patterning	exposure $\sim$ 12 mW/cm^2(405 nm) 6.2 s
	development NMD-W (60 s), DIW (180 s)
	baking 140^{o}C 5 min
ion implantation	B^+ 30 keV (1×10^{14} cm^{-2}) +50 keV (1×10^{14} cm^{-2})
	+ 100 keV (1×10^{14} cm^{-2})
resist removal	1165 at 60^{o}C
	O_2 plasma ashing 50 Pa 30 W 10 min

Table 4.3: Isolation process for AlGaN/GaN heterostructure devices.

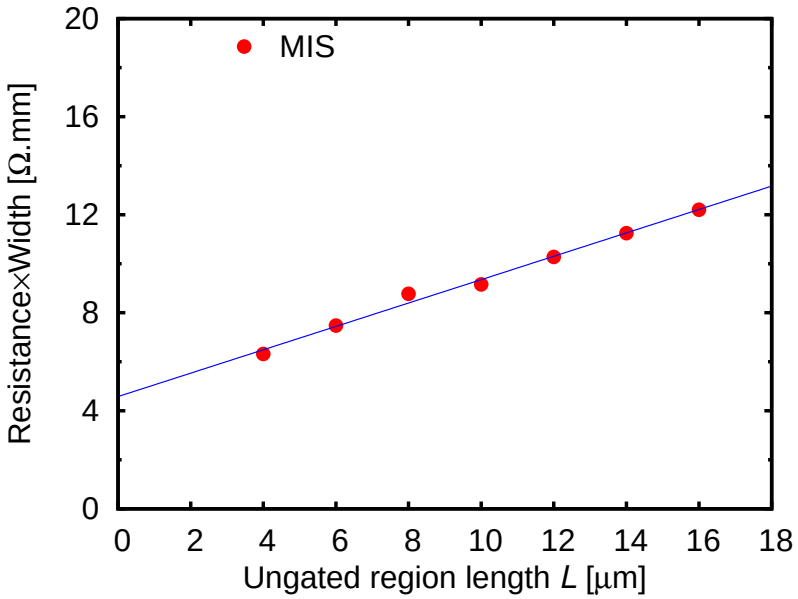

Figure 4.5: Electrode spacing dependence of the AlGaN/GaN heterostructure resistance after device isolation, obtained by TLM test element group (TEG).

After the ion implantation to isolate the device from the substrate, we carried out resistance measurements for transmission-line-model (TLM) devices, the results are shown in Fig. 4.5. We realize that the sheet resistance is about 470 Ω/sq., in the order of the result obtained by Hall effect measurements at room temperature of the AlGaN/GaN heterostructures. Hall effect measurement results show electron mobility of 1200 cm^{2}V^{-1}s^{-1}, and sheet carrier concentration of 1.2×10^{13} cm^{-2}, so we obtain

$$\rho_s = \frac{1}{e\mu n_s} = \frac{1}{1.6 \times 10^{-19} \times 1200 \text{ cm}^2/\text{Vs} \times 1.2 \times 10^{13} \text{ cm}^{-2}} \simeq 440\Omega/\text{sq.} \qquad (4.1)$$

This result shows that ion implantation did not cause strong damage or any significant change for the device region.

- Gate insulator deposition

Gate insulator, the AlN films, was deposited on the AlGaN surface following a surface treatment. We employed two types of surface treatment, the first one includes the oxygen plasma ashing and cleaning by the organic solvents for removing organic contaminants, and an additional cleaning by Semicoclean (an ammonium-based solution, ABS) for removing oxides. The second one includes the oxygen plasma ashing and cleaning by the organic solvents for removing organic contaminants The AlN layers were deposited by using RF sputtering, with the scheme shown in Fig. 4.6.

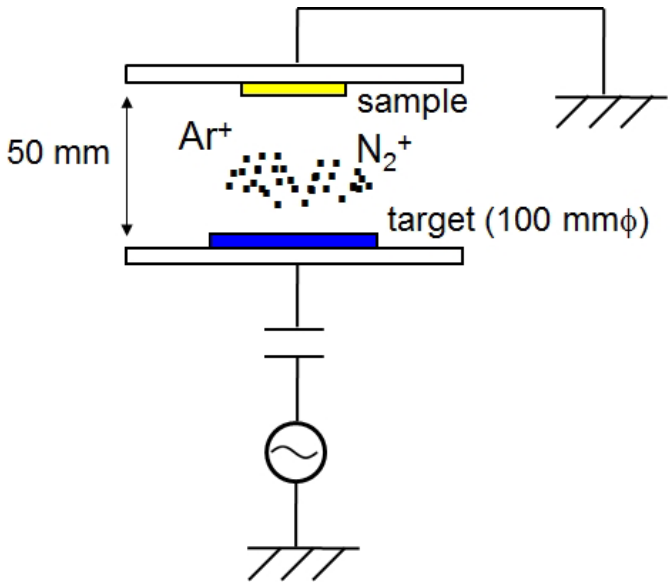

Figure 4.6: Schematic of sputtering deposition.

The sputtering conditions are:

Target: poly-crystalline AlN (3N)
Atmosphere: Ar 92% + N_2 8%
Working pressure: 0.2 Pa
Plasma power: 40 W
Preheating temperature: 250 ^oC
Sputtering temperature: RT
Sputtering rate: 2.7 nm/min

- Gate electrode formation

After the gate insulator formation, the gate electrode of the heterojunction field-effect transistors (HFETs) was patterned and deposited on the AlN layer by using EB lithography and resistance-heat (RH) evaporator. The process flow of the gate electrode formation is shown in Fig. 4.7. Surface treatments and resist coating were carried out as same as the Ohmic electrode formation process, but the patterning was done by electron beam (EB) lithography system. EB lithography is the practice of emitting a beam of electrons in a patterned fashion across a surface covered with a film called resist ("exposing" the resist) and of selectively removing either exposed or non-exposed regions of the resist ("developing"). EB lithography can create the pattern with errors less than 1 nm. After patterning

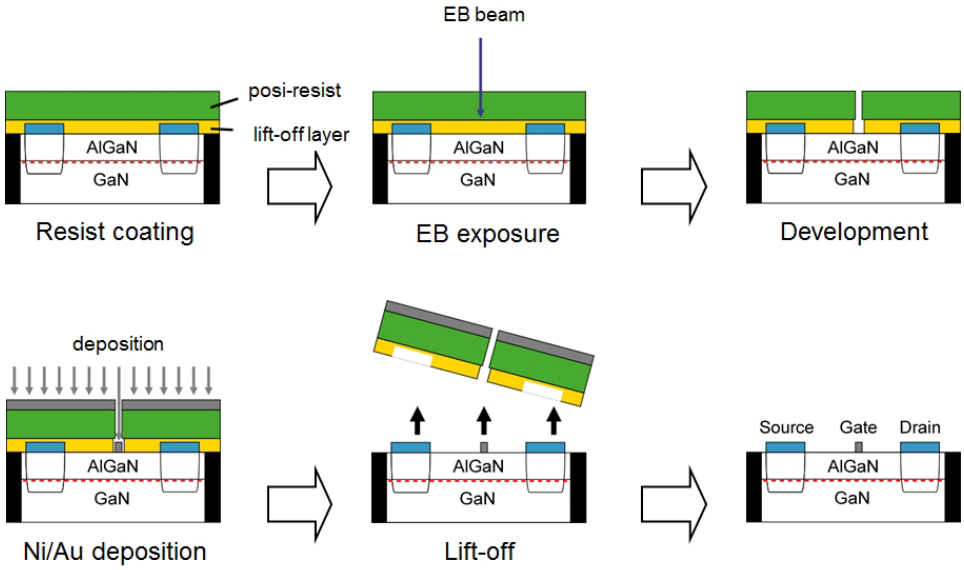

Figure 4.7: Schematic of gate formation process for AlGaN/GaN heterostructure devices.

by EB lithography system, a gate electrode was formed by resistive heating (RH) evaporator, and the electrode length would be checked (after formation) by scanning electron microscope (SEM). The receipt of electrode formation process flow is summarized in the Table 4.4.

Step	Content
surface treatment	acetone, methanol, DIW 3 min each
	O_2 plasma ashing 50 Pa 10 W 4 min
resist coating	LOL2000 (3000 rpm, 60 s), baking (180^{o}C 180 s)
	ZEP520-A7 (4000 rpm, 60 s), baking (180^{o}C 180 s)
	Espacer (1500 rpm, 60 s), baking (100^{o}C 180 s)
patterning	exposure (gate) 50 keV 50 pA pitch 13.0 μs ($\sim$ 150 μC/cm^2)
	exposure (pad) 50 keV 250 pA pitch 53.0 μs ($\sim$ 150 μC/cm^2)
	Espacer removal: DIW 60 s
	development ZED-N50 (60 s), ZMD-B (30 s) N_2 blow
	NMD-W (10 s), DIW (180 s) N_2 blow
surface treatment	O_2 plasma ashing 50 Pa 10 W 10 s
	Semico-clean 5 min, DIW 5 min
deposition	Ni/Au 5/35 nm
lift-off	1165 at 60^{o}C
	acetone, methanol, DIW 3 min each

Table 4.4: Ohmic electrode formation process for AlGaN/GaN heterostructure devices.

The gate formation (Ni/Au on the AlN surface for metal-insulator-semiconductor (MIS) devices, or on AlGaN surface for Schottky devices) completed the device fabrication process. After fabrication, the devices including heterojunction field-effect transistors (HFETs) and ungated structures (transmission-line-model TLM and Hall-bar devices) were simultaneously obtained on the same wafer. The devices include MIS structures and

Schottky structures, as shown in Fig. 4.8 with the device cross-section.

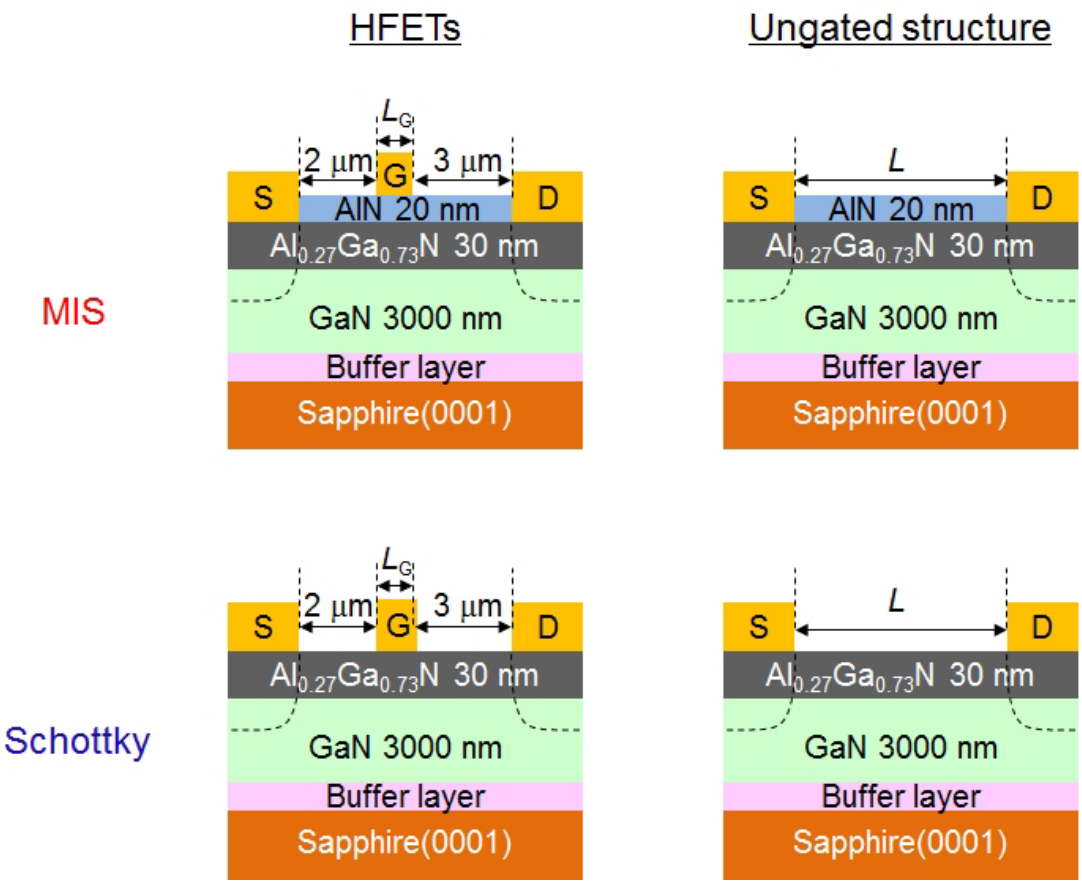

Figure 4.8: Schematic of cross section of AlGaN/GaN heterostructure devices: (a) AlN/AlGaN/GaN MIS-HFETs, (b) AlN/AlGaN/GaN MIS ungated two-terminal devices, (c) AlGaN/GaN Schottky-HFETs, (d) AlGaN/GaN Schottky ungated two-terminal devices.

The device optical images are shown in Fig. 4.9.

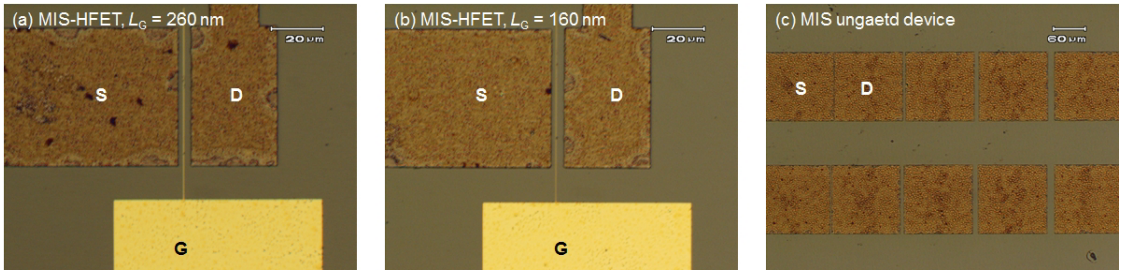

Figure 4.9: Optical image of AlN/AlGaN/GaN MIS devices: (a) and (b): AlN/AlGaN/GaN MIS-HFETs, (c) AlN/AlGaN/GaN MIS ungated two-terminal devices.

The HFETs have the gate length of 160 and 260nm, the source-gate spacing of 2 μm, the gate-drain spacing of 3 μm, and the channel width of 50 μm, while the TLM structures

have the channel width of 100 μm and electrode spacing of from 2 to 16 μm. The SEM images of the HFETs are shown in Figs. 4.10 and 4.11, which were also used to determine the gate length.

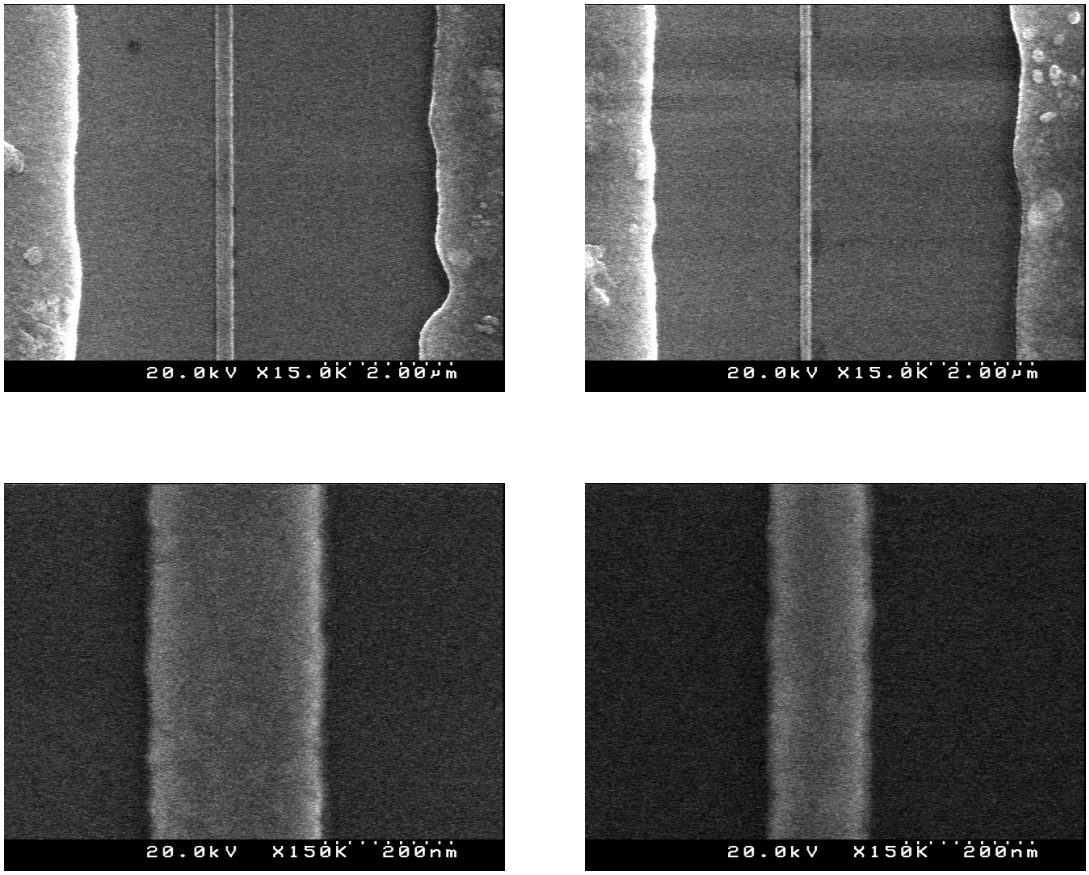

Figure 4.10: SEM image of AlN/AlGaN/GaN MIS-HFETs.

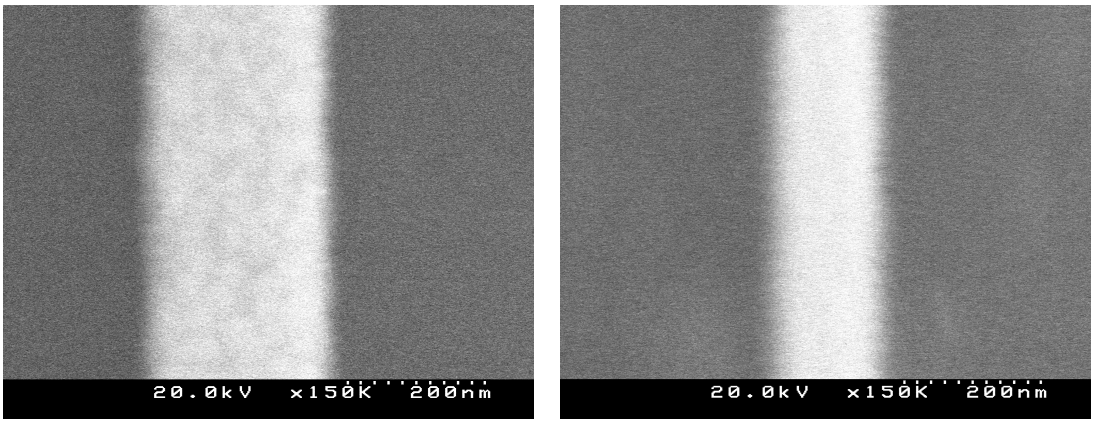

Figure 4.11: SEM image of AlGaN/GaN Schottky-HFETs.

4.2 DC characterization of AlGaN/GaN heterostructure devices

After the fabrication, the devices were characterized by using DC measurements and low-frequency noise measurements. This section is devoted to the device DC characterization, and firstly to the ungated two-terminal devices. Figure 4.12 shows the device resistance as a function of electrode spacing L for ungated TLM test element group (TEG). We realized a significant contribution of the contact to the total device resistance. The contact resistance, which was obtained from data fitting, is about 2.4 Ω.mm and almost the same for both MIS and Schottky devices, owing to the same Ohmic electrode formation process. However, the sheet resistance of the two-dimensional electron gas (2DEG) ungated region r_{sug} is different between structures; the MIS structures have $r_{\mathrm{sug}} \simeq 790\Omega$/sq. for devices with cleaning by semicoclean, an ammonium-based solution ABS, (w ABS), and 620Ω/sq. for devices without cleaning by ABS (w/o ABS), higher than that of the Schottky structures ($r_{\mathrm{sug}} \simeq 450\Omega$/sq.). The higher sheet resistance of the MIS devices is attributed to the AlGaN surface damage during the sputtering deposition of the AlN insulator layer, and the cleaning by ABS leads to further sputtering damage.

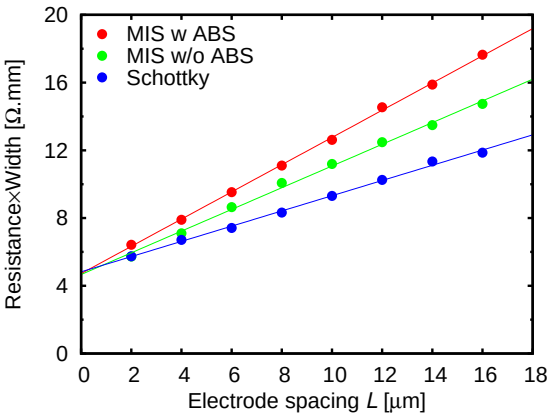

Figure 4.12: Electrode spacing L dependence of resistance obtained by ungated TLM TEG.

Furthermore, Hall-effect measurement results with Hall-bar TEG, which was fabricated simultaneously on the same wafer, are shown in the Table 4.5, from which we can realize the same sheet resistance as that obtained by the TLM TEG. We also see that both electron mobility μ and sheet carrier concentration n_{sug} of MIS structures are smaller than those of Schottky structures. The decrease of the mobility μ implies that the formation of the AlN insulator on the AlGaN surface induces addition scattering centers such as impurities due to surface damage and/or interface states due to a non-ideal insulator-semiconductor interface. The insulator and/or the insulator-semiconductor interface give significant influence on the 2DEG transport properties and also the device performances.

	MIS w ABS	MIS w/o ABS	Schottky
r_{sug} [Ω/sq.]	790	620	450
n_{sug} [cm^{-2}]	6.4×10^{12}	7.1×10^{12}	9.3×10^{12}
μ [cm^2/Vs]	1230	1430	1480

Table 4.5: Electron transport properties obtained by ungated Hall-bar TEG.

For the HFETs (three-terminal gated devices), we measured output and transfer characteristics, the results are shown as follows. Figure 4.13 shows output characteristics of the fabricated AlN/AlGaN/GaN MIS-HFETs and AlGaN/GaN Schottky-HFETs. Figures 4.14 and 4.15 show transfer characteristics of the MIS-HFETs and Schottky-HFETs for saturation regime (at $V_D = 10$ V) and linear regime (at $V_D = 0.1$ V), respectively.

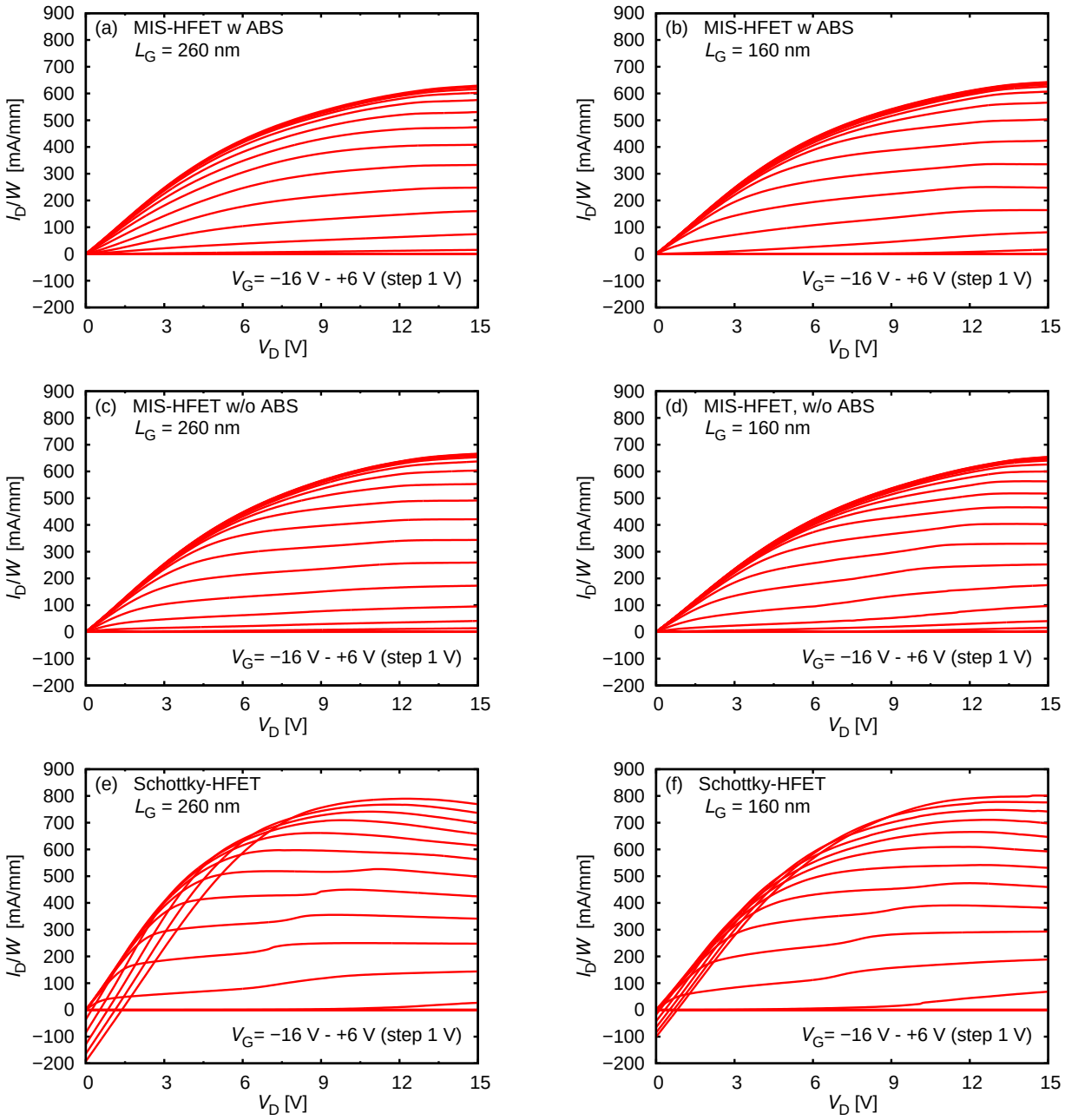

Figure 4.13: Output characteristics of the AlN/AlGaN/GaN MIS-HFETs and AlGaN/GaN Schottky-HFETs. The measurements were performed with gate-source volatge sweep of -16 V → 6 V with steps of 1 V. Drain current is normalized by the channel width I_D/W.

As seen in Fig. 4.13, while the Shottky-HFETs show negative conductance at high source-drain voltages V_D, this phenomenon is suppressed in MIS-HFETs with both types

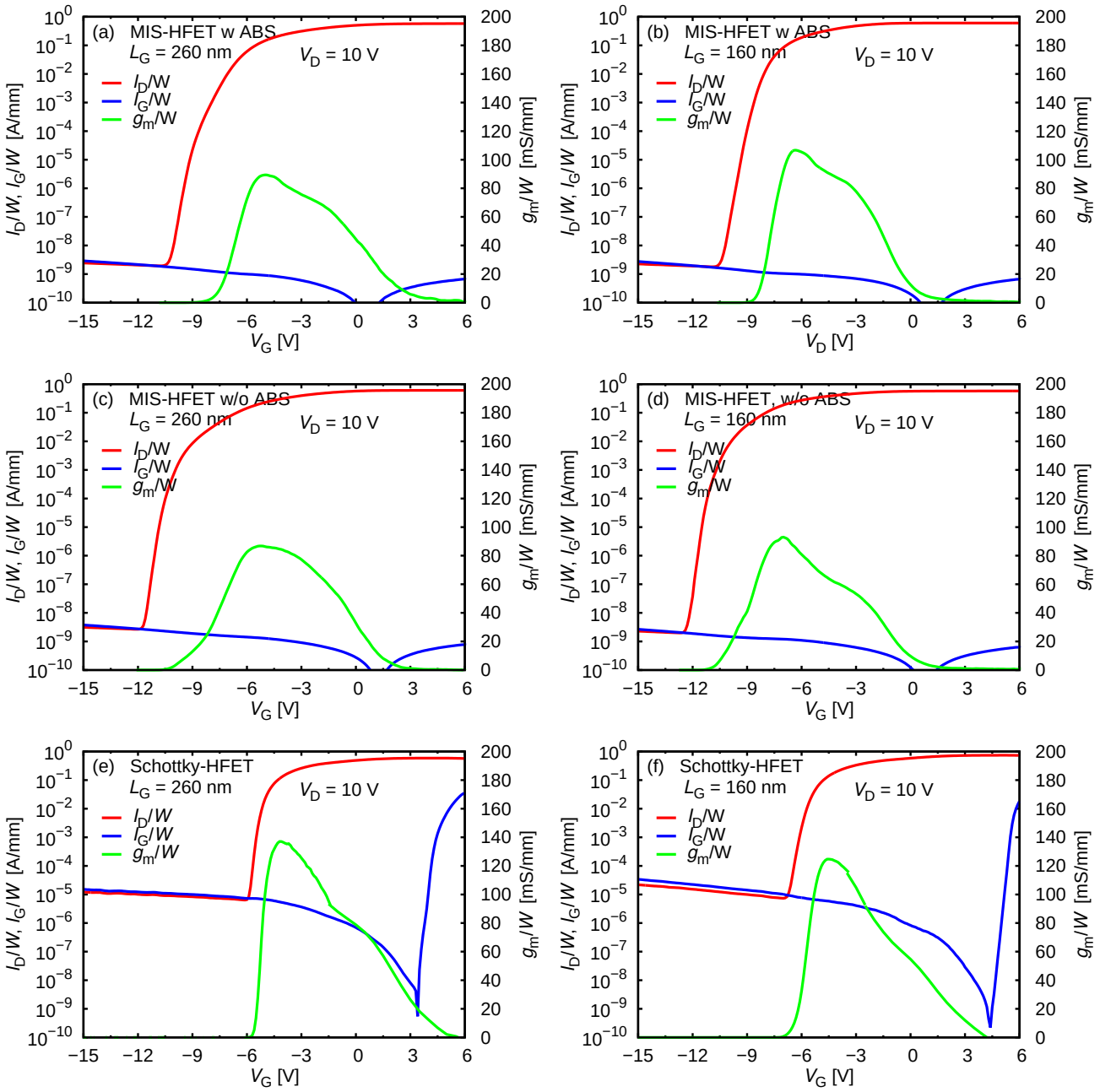

Figure 4.14: Transfer characteristics in saturation regime of the AlN/AlGaN/GaN MIS-HFETs and AlGaN/GaN Schottky-HFETs. The drain current I_D, gate current I_G, and transconductance current g_m were obtained with gate-source voltage sweep of -16 V $\rightarrow$ 6 V with steps of 0.1 V at drain voltage $V_D = 10$ V, and normalized by the channel width $1/W$.

of the surface treatment, owing to the excellent thermal conductivity of AlN, suggesting good heat release properties of the MIS-HFETs with the AlN as the gate dielectric. Kinky points sometimes appear around the drain-source voltage 6 to 9 V for the Schottky-HFETs, maybe due to crystal defects inside the AlGaN/GaN material occurred during ion implantation or electron capture at the AlGaN surface. The maximum drain current I_D of

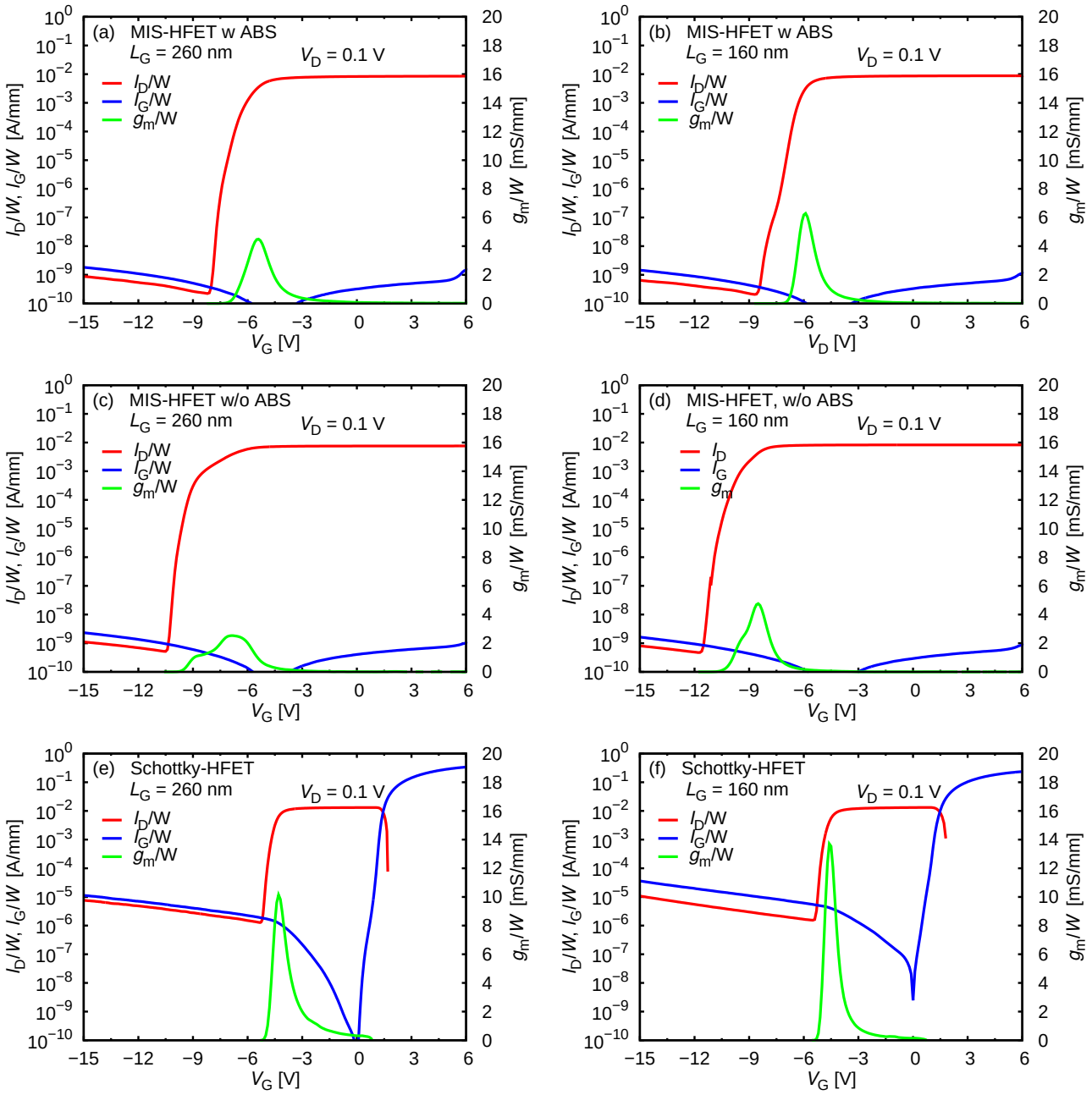

Figure 4.15: Transfer characteristics in linear regime of the AlN/AlGaN/GaN MIS-HFETs and AlGaN/GaN Schottky-HFETs. The drain current I_D, gate current I_G, and transconductance current g_m were obtained with gate-source voltage sweep of -16 V $\rightarrow$ 6 V with steps of 0.1 V at drain voltage $V_D = 0.1$ V, and normalized by the channel width $1/W$.

the MIS-HFETs (about 600 mA/mm) is lower than that of the Schottky-HFETs (about 800 mA/mm) due to an increase of the sheet resistance caused by AlGaN surface damage during the AlN deposition, confirming the data obtained by two-terminal ungated devices. However, the AlN/AlGaN/GaN MIS-HFETs with both types of the surface treatment do not show negative drain current, as observed in Schottky-HFETs at high gate voltages

($V_G > 1$ V) and low drain voltages ($V_D \leq 1.5$ V). Furthermore, the Schottky-HFETs with longer gate length $L_G = 260$nm show a more negative drain current at the same gate voltage. The negative drain current I_D is due to a domination of the gate leakage current over the drain current at high leakage current domain, in which

$$I_D = I_{SD} + I_{DG} < 0, \tag{4.2}$$

where I_{SD} and I_{DG} are currents flowing from the drain to source in the 2DEG, and from the drain to gate due to leakage paths. This is suppressed in MIS-HFETs due to a good insulating property of the AlN insulator layer, which leads to $|I_{DG}| \ll |I_{SD}|$, this conclusion is confirmed by transfer characteristics as follows.

The Fig. 4.14 obtained with source-drain voltage $V_D = 10$ V shows the transfer characteristics of AlGaN/GaN HFETs operating at saturation region, while the Fig. 4.15 obtained with source-drain voltage $V_D = 0.1$ V shows the transfer characteristics of the HFETs operating at linear region. For MIS-HFETs with both types of surface treatment, gate leakage currents are significantly small, 10^{-9} A/mm range or less, about 4 orders for reverse and 8 orders forward gate biases smaller than those of the Schottky-HFETs, owing to good insulating properties of the AlN. This is confirmed by the measurement results for the leakage current with open drain condition as shown in Fig. 4.16 for a comparison between MIS- and Schottky-HFETs. In addition, the MIS-HFETs always show positive drain currents even at small drain voltages and high gate voltages, but the Schottky-HFETs show negative drain currents at small drain voltages and high gate voltages as shown in the 4.15(e) and (f) for the Schottky devices. The negative drain region corresponds to the region in which the gate leakage current is very high and dominates over the drain current. This confirmed the negative drain current behaviors of the Schottky-HFETs as observed in the output characteristics. The small gate leakage currents of the MIS-HFETs lead to small drain off-currents. Furthermore, the MIS-HFETs show better transconductance linearity, suggesting a good gate controllability.

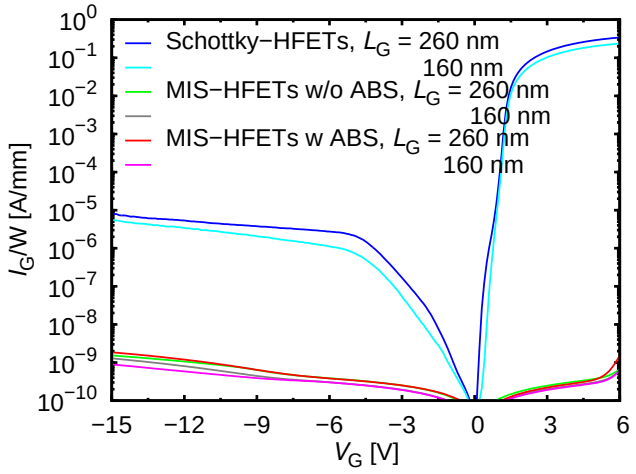

Figure 4.16: Gate leakage current I_G as functions of the gate voltage V_G for the AlGaN/GaN HFETs, obtained by measuring with open drain condition.

4.3 Low-frequency noise characterization of AlGaN/ GaN heterostructure devices

After the device DC characterization, low-frequency noise measurements were performed by using the measurement systems described in Chapter 2. All measurements were done under the atmospheric condition at room temperature in the dark when the devices and probing station were enclosed in a shielding chamber to suppressed the external effects. In this section, we will firstly discuss about the low-frequency noise characteristics of AlN/AlGaN/GaN metal-insulator-semiconductor (MIS) ungated two-terminal devices and AlGaN/GaN Schottky ungated two-terminal devices, and then about those of AlN/AlGaN/GaN MIS heterojunction field-effect transistors (HFETs) and AlGaN/GaN Schottky-HFETs (gated three-terminal devices). The MIS devices include two types of devices having the same device structures but the different fabrication processes with two types of the AlGaN surface treatments before the sputtering deposition of the AlN insulator layer as described in the section 4.1: with cleaning by ABS (MIS w ABS) and without cleaning by ABS (MIS w/o ABS).

4.3.1 Low-frequency noise characterization of AlN/AlGaN/GaN metal-insulator-semiconductor ungated two-terminal (2T) devices and AlGaN/GaN Schottky ungated 2T devices

The results of the low-frequency noise characterization of AlGaN/GaN ungated two-terminal devices including metal-insulator-semiconductor (MIS) structures and Schottky structures were obtained by measurements with ungated structures including transmission-line model (TLM) test-element group (TEG) and ungated HFET TEG. The device dimension was shown in the section 4.1. By changing bias voltages with proper settings of the off-set currents, we obtained the current noise as functions of the frequency f in the range of $1 \rightarrow 10^4$ Hz. In order to determine the off-set current, IV measurements were done to obtain the current I as a function of the bias voltage V, and the off-set currents were gotten as the same as the currents obtained by the IV results for the corresponding bias voltages. For the setting of low-noise preamplifier (LNA) sensitivity, we have to follow the trade-off between the lower limit of the measurement system and the device resistance, as discussed in section 2.2.2. Because of small resistance of the measured devices (in the order of 200 Ω or less, obtained from IV measurements), the sensitivity was chosen to be 10^3 or 10^4 V/A, corresponding to the 1 Ω internal impedance of the LNA (see section 2.2.2). For these sensitivities of the LNA, the system noise floors are between 10^{-19}-10^{-20} A^2/Hz as seen in the Fig 2.12. In addition, to ensure that the measurements were done under the linear regime of the devices, the measurements were limited to bias voltage equal or less than 1 V.

To measure the ungated two-terminal devices, inside the shielding chamber of the probe station, one Ohmic electrode of the device is connected to the LNA with applications of a DC bias voltage and a DC off-set current, while the other Ohmic electrode is grounded. The current noise is amplified by the LNA, whose output is entered to the dynamic signal analyzer (DSA) to obtain the power spectrum density(PSD). Finally, we obtained the current noise with PSD $S_I(f)$ as functions of the frequency f, and depending on the current I flowing through the devices. The measurement results were shown in

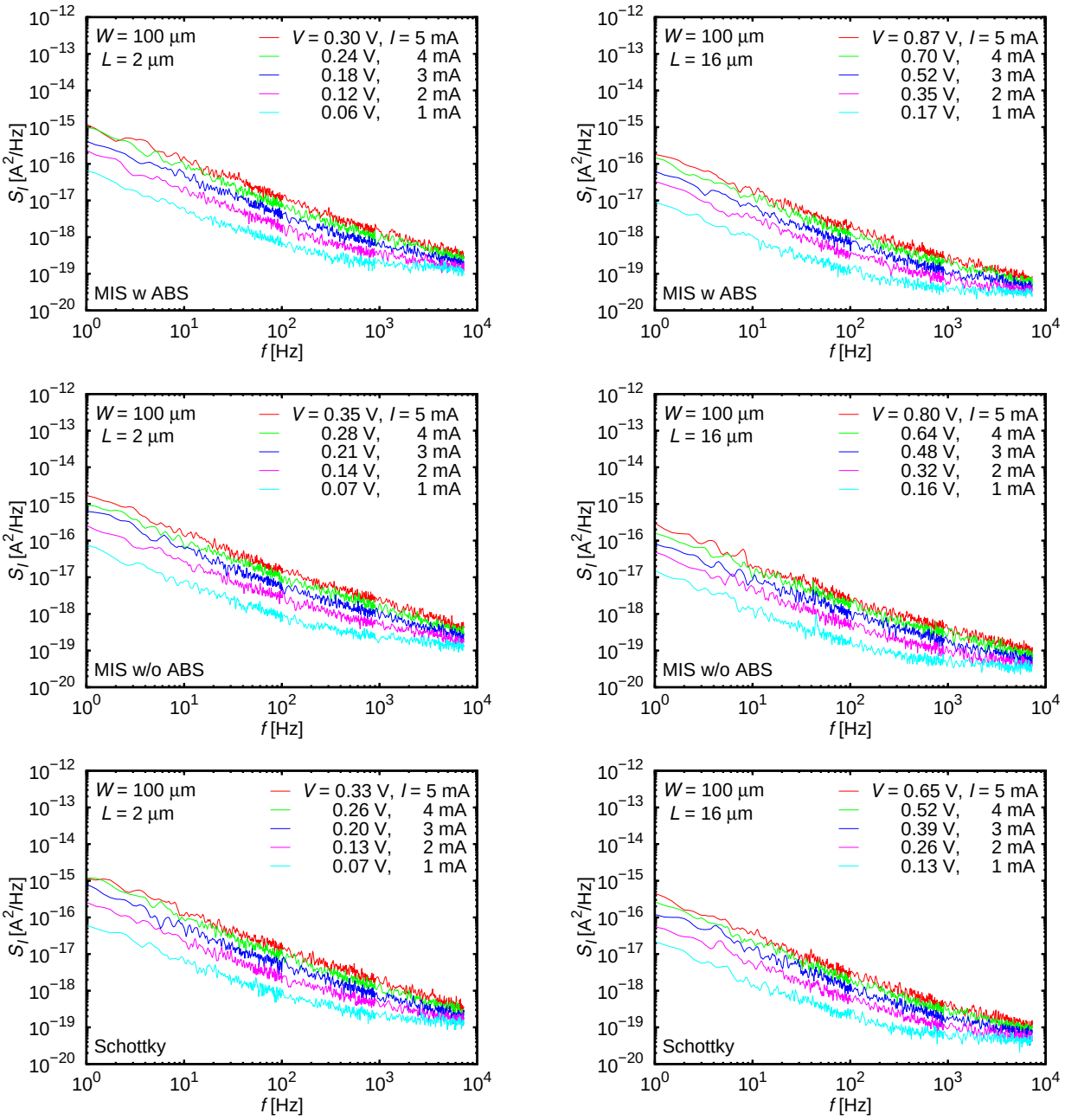

Figure 4.17: Low-frequency spectra of the current noise of AlGaN/GaN ungated TLM structures with PSD S_I as functions of the frequency f. From the top to the bottom are for MIS w ABS, MIS w/o ABS and Schottky devices, respectively. The measurement results are for electrode spacing $L = 2,\ 16$ μm as examples. The channel width $W = 100$ μm.

Figs. 4.17 with the S_I as functions of f, for ungated TLM devices with different electrode spacing (or ungated region length) L. Low-frequency noise spectra show $S_I \propto f^{\gamma},\ \gamma \simeq 1$ for all measurements with $f \lesssim 1$ kHz. Neither specific bumps nor peaks are observed, indicating no generation-recombination noise due to specific high-density electron traps with a specific time constant as well as no external noise effects. The flat behavior at

high frequencies $f \gtrsim 1$kHz in measurements with small currents is due to the lower limit of the measurement system.

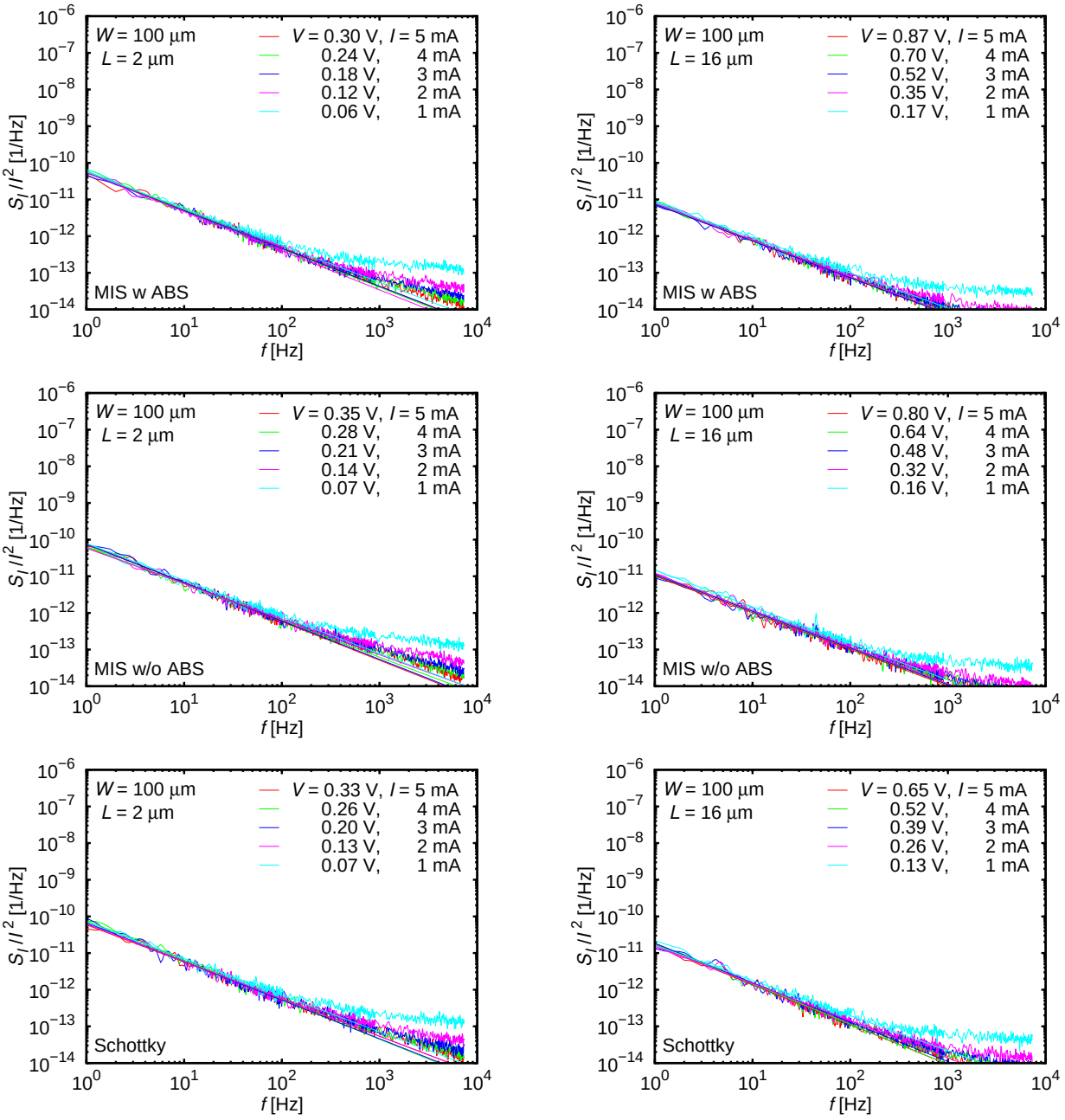

Figure 4.18: Low-frequency spectra of the current noise of ungated AlGaN/GaN TLM structures with S_I/I^2 as functions of the frequency f. From the top to the bottom are for MIS w ABS, MIS w/o ABS and Schottky devices, respectively. The measurement results are for electrode spacing $L = 2,\ 16$ μm as examples. The channel width $W = 100$ μm.

Figure 4.18 shows S_I/I^2 as functions of f. For the $1/f$ behavior domain, we realized that the S_I/I^2 seems a constant, independent of the current I for specific values of L. This means that S_I may be proportional to I^2. In order to clarify this conjecture, we

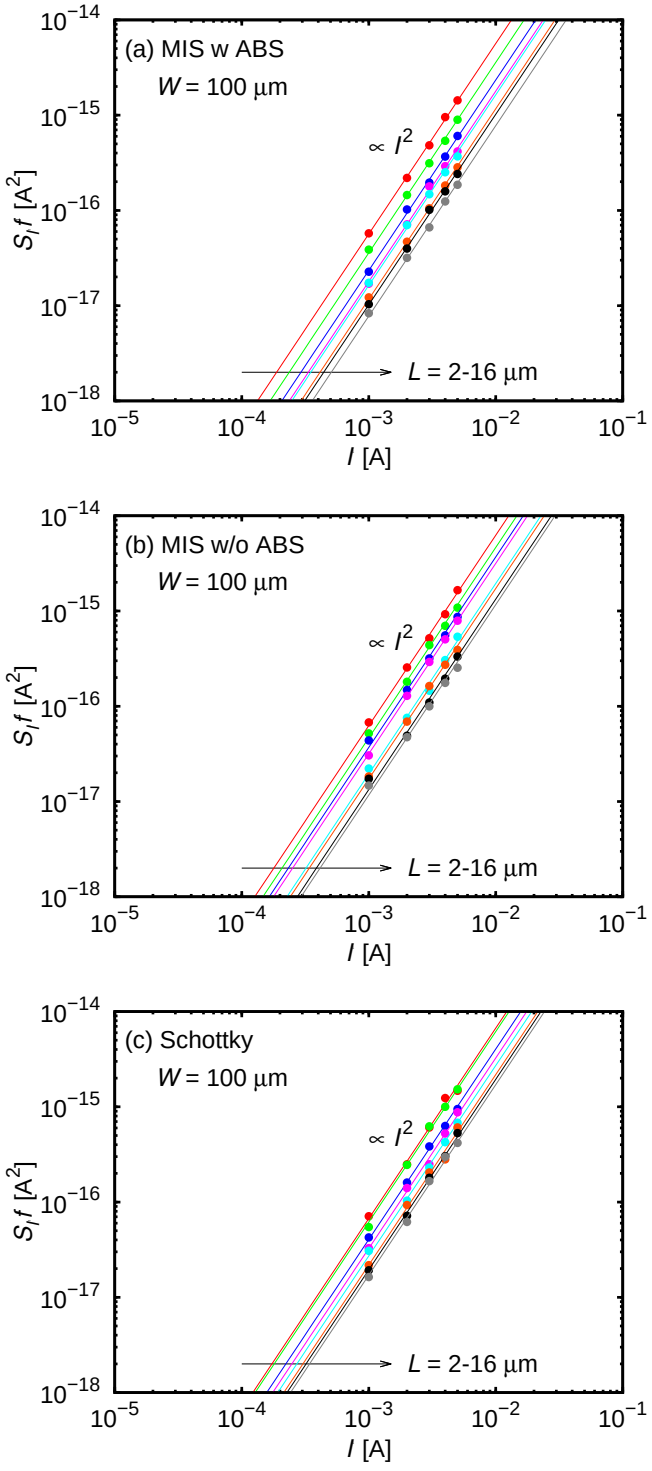

Figure 4.19: The $S_I f$ as functions of the current I for AlGaN/GaN ungated structures. From the top to the bottom are for MIS w ABS, MIS w/o ABS and Schottky devices, respectively.

investigated $S_I f$ as functions of the current I for different L, the results are shown in Fig. 4.19. We realized that $S_I f \propto I^2$ for all measurements, which implies a Hooge-like

formula expressing the low-frequency noise spectra using a constant factor K

$$S_I = \frac{KI^2}{f}. \tag{4.3}$$

Figure 4.19 not only confirms the validity of Eq. (4.3) but also shows that the factor K is a constant, depending on the device size. The size dependence of the factor K will be discussed as follows.

As discussed in the section 4.1 for the DC characterization, the contact resistance gives a significant contribution to the total resistance of the AlGaN/GaN ungated structures. Moreover, the current noise is actually the fluctuations in the device resistance, as discussed in section 1.3.2. Therefore, we may think about a significant role of the contact resistance in the generation of the device current noise. To evaluate the contribution of the contacts and the conducting channel, we consider them as two resistors, the contact resistor with resistance $2R_c$ and the 2DEG channel resistor with resistance R_{2DEG}, in series with a schematic figure of the conduction path shown in Fig. 4.20.

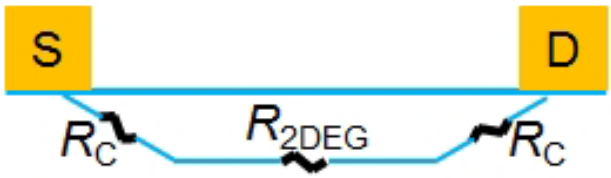

Figure 4.20: The schematic of the conduction path for the AlGaN/GaN ungated two-terminal devices with resistors in series.

For two resistors in series $V = V_A + V_B$, by reminding Eq. (3.9) we have

$$S_I = S_I^A \frac{{V_A}^2}{V^2} + S_I^B \frac{{V_B}^2}{V^2} = S_I^A \frac{{R_A}^2}{(R_A + R_B)^2} + S_I^B \frac{{R_B}^2}{(R_A + R_B)^2}. \tag{4.4}$$

Using this equation, we obtain the S_I for the AlGaN/GaN ungated two-terminal devices

$$S_I = S_I^c \frac{{2R_c}^2}{(2R_c + R_{2DEG})^2} + S_I^{2DEG} \frac{{R_{2DEG}}^2}{(2R_c + R_{2DEG})^2}, \tag{4.5}$$

where S_I^c is the current noise PSD generated by a single contact having a resistance

$$R_c = \frac{r_c}{W}, \tag{4.6}$$

and S_I^{2DEG} is the current noise PSD generated by a single ungated 2DEG channel having a resistance

$$R_{2DEG} = \frac{r_{sug} L}{W}, \tag{4.7}$$

where r_{sug} is the sheet resistance of the ungated 2DEG, which was obtained simultaneously with the contact resistance R_c by DC measurements with TLMs (discussed in section 4.2), L and W are the length and width of the devices, respectively.

Applying Eq. (4.5) for the factor K

$$\begin{aligned} K &= \frac{S_I}{I^2} f \\ &= K_{\rm c} \frac{2{R_{\rm c}}^2}{(2R_{\rm c} + R_{\rm 2DEG})^2} + K_{\rm 2DEG} \frac{{R_{\rm 2DEG}}^2}{(2R_{\rm c} + R_{\rm 2DEG})^2}, \end{aligned} \tag{4.8}$$

where $K_{\rm c}$, $K_{\rm 2DEG}$ are the factors for the contact and 2DEG channel, respectively; the latter is determined by Hooge model [33]

$$K_{\rm 2DEG} = \frac{\alpha_{\rm ug}}{N} = \frac{\alpha_{\rm ug}}{n_{\rm sug} LW}, \tag{4.9}$$

where $\alpha_{\rm ug}$ and N are the Hooge parameter and carrier number of the ungated 2DEG, and $n_{\rm sug}$ is the sheet electron concentration of the ungated 2DEG, which was obtained by Hall-effect measurements. Hooge parameter is then calculated by

$$\alpha_{\rm ug} = K_{\rm 2DEG} N = K_{\rm 2DEG} n_{\rm sug} LW. \tag{4.10}$$

We can rewrite Eq. (4.8) as

$$KW = \frac{(K_{\rm c} W/2) + (\alpha_{\rm ug}/n_{\rm sug})(r_{\rm sug}/2r_{\rm c})^2 L}{[1 + (r_{\rm sug}/2r_{\rm c})L]^2}. \tag{4.11}$$

Equation (4.11) indicates that the factor K is a function of the device size. In particular, the factor KW is a function of the electrode spacing L, i.e., the ungated 2DEG length of the ungated two-terminal devices. We will consider the behaviors of size dependence of the factor K in details as follows.

From Eq. (4.11), we realize that the size dependence of the factor K depends not only the noise parameters $K_{\rm c}$ and $K_{\rm 2DEG}$, but also transport properties $r_{\rm c}$ and $r_{\rm sug}$. When $2r_{\rm c} \gg r_{\rm sug} L$, i.e., the contact resistance is much larger than the 2DEG channel resistance (e.g., in the case of small L or more accurately, when $L \to 0$), the first term of Eq. (4.11) dominates the factor K, and we get

$$K \simeq K_{\rm c}/2 = constant, \tag{4.12}$$

the device noise is dominated by the contact noise. On the other hand, when $2r_{\rm c} \ll r_{\rm sug} L$, i.e., the contact resistance is much smaller than the 2DEG channel resistance (e.g., in the case of large L or more accurately, when $L \to \infty$), the second term of Eq. (4.11) dominates the factor K, and we obtain

$$KW \simeq \frac{\alpha_{\rm ug}}{n_{\rm sug} L} \propto \frac{1}{L}, \tag{4.13}$$

the device noise is dominated by the 2DEG channel noise. These limits of the L-dependence will identify whenever the contact or the semiconductor 2DEG conducting channel dominates the current noise of the ungated two-terminal devices.

Since $R_{\rm c} \propto 1/W$, $R_{\rm 2DEG} \propto L/W$, $K_{\rm c} \propto 1/W$, and $K_{\rm 2DEG} \propto 1/LW$, the factor KW given by Eq. (4.11) is a single-valued function of the electrode spacing L. A plot of the factor KW as functions of L with the fitting lines by using Eq. (4.11) is shown in Fig. 4.21 for AlGaN/GaN ungated two-terminal devices. The figure with linear scale

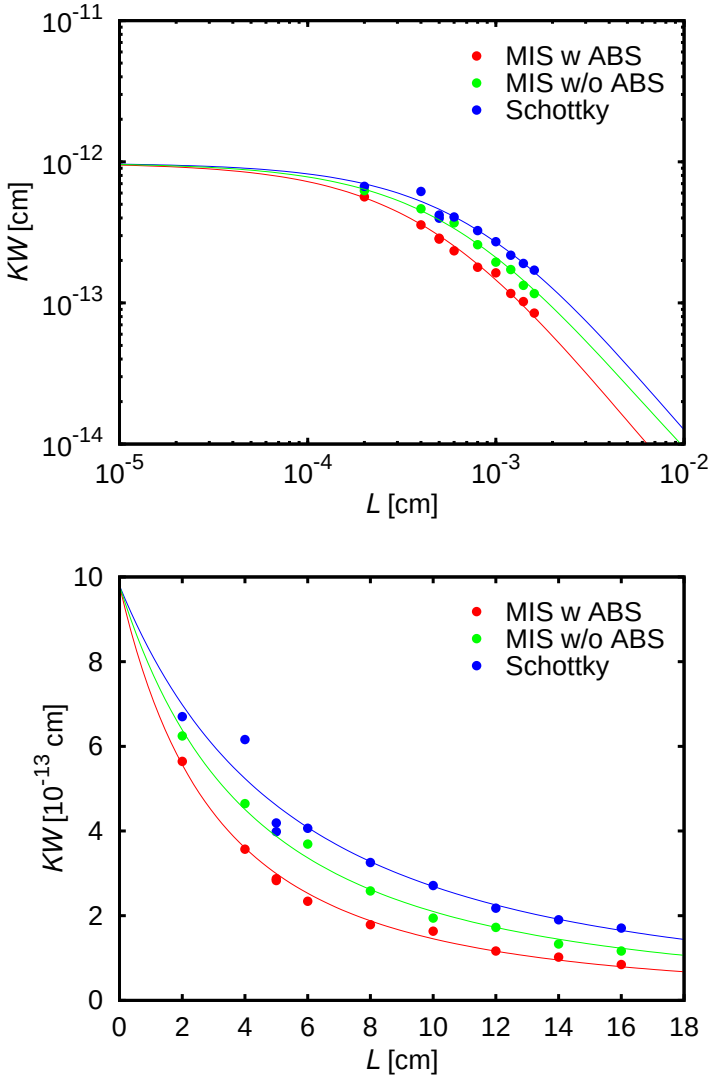

Figure 4.21: The factor KW as functions of L of the AlGaN/GaN ungated structures, in logarithm scale for the top and linear scale for the bottom. The lines are fitting lines using Eq. (4.11).

confirms the validity of the fitting. We realize that the Eq. (4.13) does not hold for whole range of L with a constant behavior at small L, suggesting a significant contribution of the noise generated by electrode contacts. In other words, the factor K is a function of both K_c and K_{2DEG}, expressed by Eq. (4.11), due to a significant contribution of the contact noise to the total noise in the AlGaN/GaN devices. Furthermore, we can also realize the limits formulated by Eqs. (4.12-4.13) from the experimental data as well as the fitting lines (seen more clearly in the figure with a logarithm scale). At large L values, $KW \propto 1/L$, indicating the domination of the conducting channel noise by Eq. (4.13), while $K \simeq$ constant at small L, showing the domination of the contact noise by Eq. (4.12). Furthermore, the size dependence of the factor K with fitting lines can help us evaluate the contributions of the contact and 2DEG channel to the total noise. The factor K_c

of the contact and Hooge parameter α_{ug} of the ungated 2DEG were obtained from size dependence of the factor K as fitting parameters of the data points with Eq. (4.11). The results are shown in Table 4.6. The factor K_c is almost the same for all structures due to the same Ohmic electrode formation process for both MIS and Schottky devices, but the Hooge parameter α_{ug} is different from MIS to Schottky devices with $\alpha_{ug} \simeq 2.2 \times 10^{-4}$ for the MIS devices with cleaning by ABS, $\simeq 4.1 \times 10^{-4}$ for the MIS devices without cleaning by ABS, and $\simeq 5.0 \times 10^{-4}$ for the Schottky devices. The decreasing of the Hooge parameter in MIS devices can be explained by a decrease in the electron mobility due to the presence of additional scattering mechanisms, which may be related to the insulator-semiconductor interface, suggesting that the mobility fluctuations may play a dominant role in the noise origin of the ungated devices, this was also supported by the unity frequency exponent ($\gamma \simeq 1$) as expected by Hooge mobility fluctuation model [33]. We hence conclude that the low-frequency noise in AlGaN ungated two-terminal devices including MIS structures using AlN as the insulator layer and Schottky structures is caused by a domination of the mobility fluctuation according to the Hooge model [33]. Furthermore, the values of Hooge parameter obtained by our devices is in order of 10^{-4}, this is a very small Hooge parameter in comparison with those ever reported for GaN-based devices, implying low-noise characteristics of the fabricated devices.

	MIS w ABS	MIS w/o ABS	Schottky
K_cW [cm]	1.94×10^{-12}	1.94×10^{-12}	1.94×10^{-12}
α_{ug}	2.2×10^{-4}	4.1×10^{-4}	5.0×10^{-4}

Table 4.6: The factor K_cW and Hooge parameter α_{ug} for ungated two-terminal devices.

To evaluate the validity of the fitting parameters, i.e., the factor K_c and also α_{ug}, we consider the contact electrode as a circuit shown in Fig. 4.22. The metal electrode has a length L_e, a width W, and a specific contact resistance ρ_c, leading to a conductance $G = \rho_c/W$ per unit length along (parallel to) the electrode (we should take a note that the current flowing direction through the metal is perpendicular to the metal pad). The semiconductor has a sheet resistance r_s, hence, the semiconductor region under the metal electrode has a resistance $R = r_s/W$ per unit length along the electrode pad. According to the current flowing direction, an element length dx of the electrode has a resistance Rdx, a conductance Gdx, and a corresponding impedance dZ.

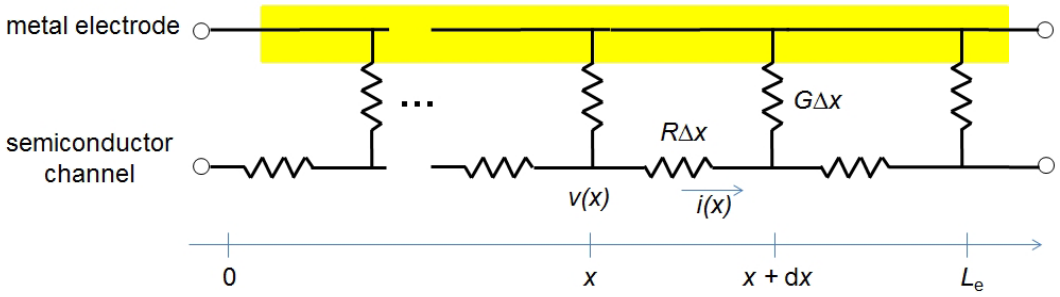

Figure 4.22: The schematic of the circuit of a contact electrode including a metal layer on a semiconductor.

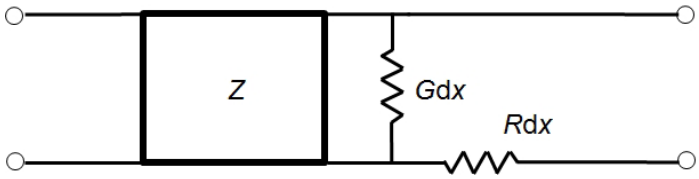

Figure 4.23: The schematic of the reduced circuit of a contact electrode illustrated by Fig. 4.22.

In this discussion and for a simplicity, we consider a reduced circuit of the contact electrode with its circuit shown in Fig. 4.22 as a combination shown in Fig. 4.23. Due to infinite condition of the $L_{\rm e}$ ($L_{\rm e} \gg {\rm d}x$), we can get

$$Z \simeq Z + {\rm d}Z = (\frac{1}{Z + R{\rm d}x} + G{\rm d}x)^{-1}. \tag{4.14}$$

By using the first-order approximation, we have

$$\begin{aligned} Z &= (\frac{1}{Z + R{\rm d}x} + G{\rm d}x)^{-1} \\ &\simeq [\frac{1}{Z}(1 + \frac{R{\rm d}x}{Z})^{-1} + G{\rm d}x]^{-1} \\ &\simeq [\frac{1}{Z}(1 - \frac{R{\rm d}x}{Z}) + G{\rm d}x]^{-1} \\ &\simeq [\frac{1}{Z}(1 - \frac{R{\rm d}x}{Z} + GZ{\rm d}x)]^{-1} \\ &\simeq Z(1 + \frac{R{\rm d}x}{Z} - GZ{\rm d}x). \end{aligned} \tag{4.15}$$

Combining Eq. (4.28) and (4.15), we obtain

$$\begin{aligned} {\rm d}Z &= (R - GZ^2){\rm d}x, \text{ or} && (4.16) \\ \frac{{\rm d}Z}{{\rm d}x} &= R - GZ^2 && (4.17) \end{aligned}$$

The impedance Z generates a current noise with a factor K, hence, the combination of Z and $R{\rm d}x$ in series will generated a current noise with a factor K'. The factor K' is given by a formula similar to Eq. (4.8) with the first order approximation as follows

$$\begin{aligned} K' &= \frac{KZ^2 + (A/{\rm d}x)(R{\rm d}x)^2}{(Z + R{\rm d}x)^2} && (4.18) \\ &\simeq [KZ^2 + AR^2{\rm d}x]Z^{-2}(1 - 2R{\rm d}x/Z) && (4.19) \\ &\simeq K(1 + \frac{AR^2}{Z^2K}{\rm d}x - \frac{2R}{Z}{\rm d}x), && (4.20) \end{aligned}$$

where the factor A is determined by using Eq. (4.8) $A = \alpha_{\rm ug}/(n_{\rm s}W)$. We next consider a combination of Z and $R{\rm d}x$ are in parallel to $G{\rm d}x$, these three resistors generate a current noise with a factor K''. We have to consider two resistors A and B with conductance $G_{\rm A}$

and $G_{\rm B}$ in parallel, where $I = I_{\rm A} + I_{\rm B}$, the total current noise PSD generated is given by (see Appendix D.1)

$$S_I = S^{\rm A}_{I_{\rm A}} + S^{\rm B}_{I_{\rm B}}, \text{ or} \tag{4.21}$$

$$\frac{S_I}{I^2} = \frac{S^{\rm A}_{I_{\rm A}} + S^{\rm B}_{I_{\rm B}}}{(I_{\rm A}+I_{\rm B})^2} = \frac{S^{\rm A}_{I_{\rm A}}}{{I_{\rm A}}^2}\frac{{I_{\rm A}}^2}{(I_{\rm A}+I_{\rm B})^2} + \frac{S^{\rm B}_{I_{\rm B}}}{{I_{\rm B}}^2}\frac{{I_{\rm B}}^2}{(I_{\rm A}+I_{\rm B})^2}. \tag{4.22}$$

The factor K for two resistors in parallel

$$K = K_{\rm A}\frac{{G_{\rm A}}^2}{(G_{\rm A}+G_{\rm B})^2} + K_{\rm B}\frac{{G_{\rm B}}^2}{(G_{\rm A}+G_{\rm B})^2}. \tag{4.23}$$

By applying this equation, the factor K'' is calculated similarly to the K'

$$K'' = \frac{K'/{Z'}^2 + (B/{\rm d}x)(G{\rm d}x)^2}{(Z'+G{\rm d}x)^2} \tag{4.24}$$

$$\simeq K'(1 + \frac{BG^2{Z'}^2}{K'}{\rm d}x - 2RZ'{\rm d}x), \tag{4.25}$$

$$\simeq K + [\frac{AR^2}{Z^2} + BZ^2G^2 - 2K(\frac{R}{Z} + GZ)]{\rm d}x, \tag{4.26}$$

where $Z' = Z + R{\rm d}x$ and the B is a constant factor. Hence

$$\frac{{\rm d}K''}{{\rm d}x} \simeq \frac{AR^2}{Z^2} + BZ^2G^2 - 2K(\frac{R}{Z} + GZ). \tag{4.27}$$

When $x = L \gg {\rm d}x$ or $x \to \infty$, from Eq. (4.16), we have

$$Z = \sqrt{RG} = \frac{\sqrt{\rho_{\rm c} r_{\rm s}}}{W} \tag{4.28}$$

and in combination with Eq. (4.27), we obtain the factor for a single contact electrode

$$K_{\rm c} = \frac{\sqrt{RG}(A+B)}{4}. \tag{4.29}$$

Equation (4.29) gives the factor $K_{\rm c}$ for the current noise generated by a single contact electrode (the contact noise), showing two important properties

- The noise power (here, the factor $K_{\rm c}$ of the contact) reaches to a constant value given by Eq. (4.29) but not to be zero, even when the contact length becomes infinite.
- The factor $K_{\rm c} \propto \sqrt{RG} \propto 1/W$, scaling down by only the semiconductor channel width, but independently of the electrode size.

For a rough evaluation, we also realize by using results shown in Tables 4.5-4.6 that

$$K_{\rm c} = \frac{\sqrt{RG}(A+B)}{4} \gtrsim \frac{\sqrt{RG}A}{4} = \frac{\sqrt{RG}}{4}\frac{\alpha_{\rm ug}}{n_{\rm sug}W} \simeq 6\times10^{-12}\ \text{cm}. \tag{4.30}$$

This is the lower limit of the factor $K_{\rm c}$ for our devices. This value is much smaller than $K_{\rm c}$ obtained by Eq. (4.11), indicating the validity of the equation. Furthermore, this also suggests that the contact noise $K_{\rm c}$ is mainly given by the second factor determined by B factor, which is given by calculation with G or ρ_c. This leads to a conclusion that

the contact noise is mainly generated by the conduction paths perpendicular to the metal contact pad, not by the conduction paths parallel to the metal pad. To reduce the contact noise, we have to reduce the contact resistance between the metal and semiconductor.

In addition to the size dependence of the factor K, we also obtained a size dependence of the total resistance R of the ungated region,

$$RW = (2R_c + R_{2DEG})W = 2r_c + r_{sug}L \tag{4.31}$$

leading to the factor K is a single-valued function of the R, given by

$$KW = \frac{2K_c r_c + (\alpha_{ug} r_{sug}/n_{sug})(RW - 2r_c)}{(RW)^2} \tag{4.32}$$

Plots of KW as functions of RW are shown in Fig. 4.24. The correlation between KW and RW is important for analysis the noise of gated structures in which we consider the conduction path of the gated devices as gated region and ungated part in series. The contribution of the ungated region will be determined using the KW-RW dependence obtained by the ungated structures, as shown in Fig. 4.24.

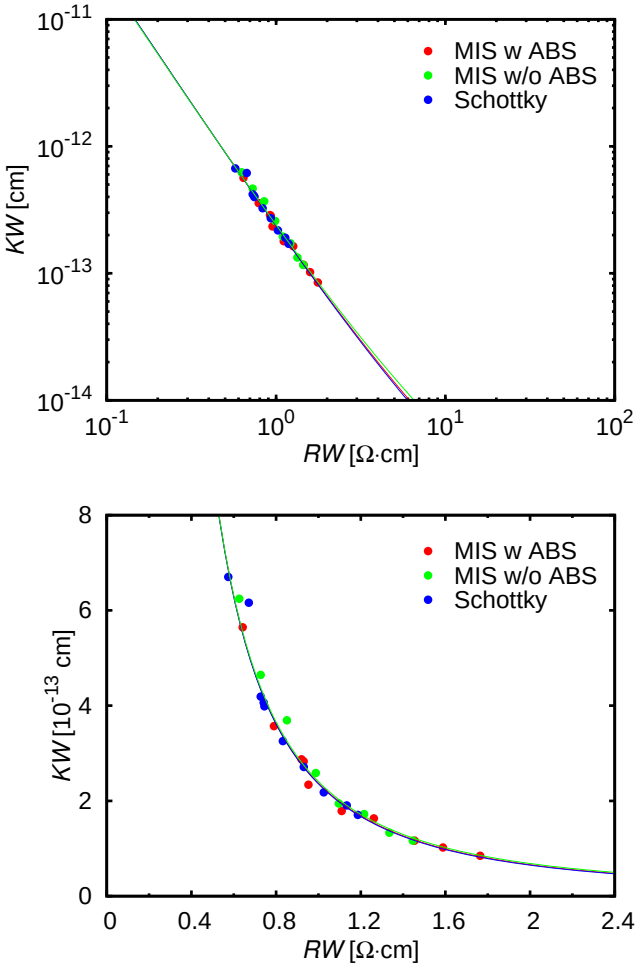

Figure 4.24: KW as functions of RW for the AlGaN/GaN ungated two-terminal devices, in logarithm scale for the top and linear scale for the bottom, with fitting lines using Eq. (4.32).

4.3.2 Low-frequency noise characterization of Al/AlGaN/GaN metal-insulator-semiconductor heterojunction field-effect transistors (MIS-HFETs) and AlGaN/GaN Schottky heterojunction field-effect transistors (Schottky-HFETs): a comparison between MIS-HFETs and Schottky-HFETs

After the characterization of the ungated two-terminal devices, low-frequency noise in AlGaN/GaN gated three-terminal devices was systematically investigated by using AlN/AlGaN/GaN MIS-HFETs, where the AlN film was sputtering-deposited as the gate insulator layer on the AlGaN surface with two different surface treatments as discussed in section 4.1 (as a result, we obtained two device types: MIS-HFETs w ABS and MIS-HFETs w/o ABS), and AlGaN/GaN Schottky-HFETs. Low-frequency noise measurements were performed by using 3T-DUT measurement system configuration shown by Fig. 2.2(b) as described in the chapter 2. In order to clarify the variation in the noise characteristics, changing in gate-source voltage V_{G} and drain-source voltage V_{D} was done during the measurements.

The measurement procedures are same as those for two-terminal devices. In order to determine the off-set current, we carried out $I_{\mathrm{D}}V_{\mathrm{D}}$ measurements with changing the V_{G}. We firstly bias the gate-source using the SMU with gate-source voltage V_{G}, then measure the drain current I_{D} as functions of V_{D}. The off-set dain current of low-frequency noise measurements is same at the drain current I_{D} at the corresponding V_{D} and V_{G}. At a fixed V_{G}, the low-frequency drain current noise as a function of the drain current I_{D} is obtained with changing V_{D}. By changing V_{G}, we will obtain the low-frequency drain current noise as a function of the gate voltage. For measurements of the HFETs, inside the shielding chamber, the source is grounded, the drain is connected to the LNA with applications of a DC bias drain voltage and a DC off-set drain current, and a gate voltage is applied from a parameter analyzer (SMU) through an RC passive low-pass filter (LPF) with a cut-off frequency $\sim$ 0.05 Hz to eliminate the noise from the parameter analyzer. As a result, we obtain the drain current noise with the noise power spectrum density (PSD) $S_{I_{\mathrm{D}}}$ as functions of both V_{D} (or I_{D}) and V_{G}, and of course, a function of the frequency f. Due to limits of measurement system, we restricted our measurements with either $I_{\mathrm{D}} \lesssim$ 5mA or $V_{\mathrm{D}} \lesssim$ 5V. However, the measurement voltage range is also restricted in linear regime (confirmed by $I_{\mathrm{D}}V_{\mathrm{D}}$ measurements) for all the gate-source voltages.

In combination with the investigation of low-frequency noise in the ungated two-terminal devices, which was presented in the section 4.2, we extract low-frequency noise behaviors of the intrinsic gated region in the HFETs, which depend on the gate bias voltage. The low-frequency noise characteristics of the intrinsic gated region will be discussed in details in order to clarify the noise mechanisms in the AlGaN/GaN HFETs. Furthermore, the low-frequency noise characteristics of the intrinsic gated region of different devices will be compared with each other (MIS-HFETs with Schottky-HFETs, MIS-HFETs w ABS with MIS-HFETs w/o ABS) simultaneously. In addition, in order to calculate the Hooge parameter of the intrinsic gated region, we have to know the electron sheet concentration under the gate. The CV measurements were done with the capacitors, which were obtained simultaneously with the ungated TEG and the HFET TEG. The electron sheet concentration n_{s} under the gate would be calculated from the integration of capacitance C, depending on the gate bias voltage.

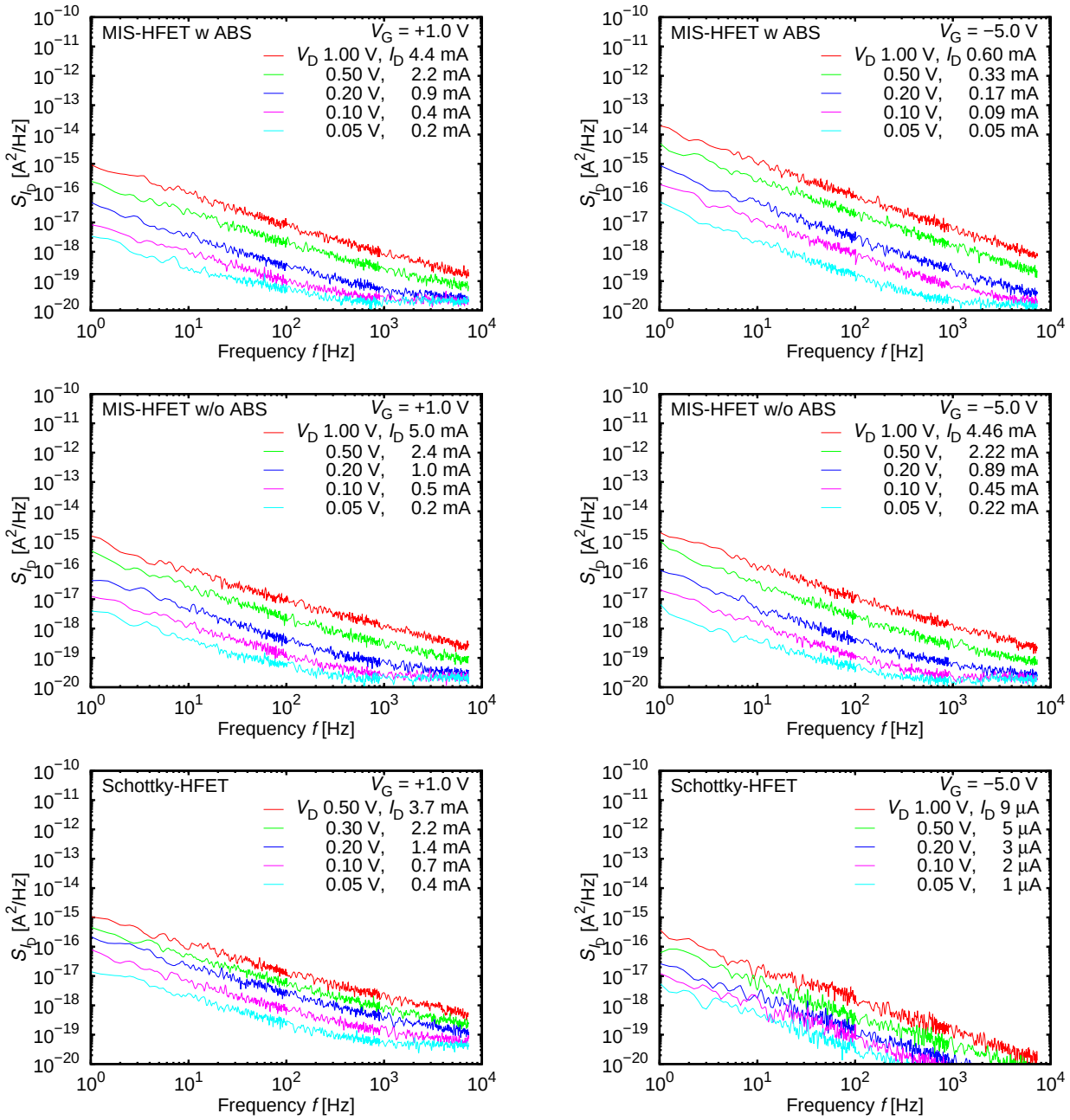

Figure 4.25: Low-frequency noise spectra of the drain current I_D in AlGaN/GaN HFETs having gate length $L_G = 260$ nm and channel width $W = 50$ μm with PSD S_{I_D} as functions of the frequency f. From the top to the bottom are for MIS w ABS, MIS w/o ABS and Schottky devices, respectively. The measurement results are for some gate-source voltages V_G as examples.

The measurement results are shown in Figs. 4.25 and 4.26 for the AlN/AlGaN/GaN MIS-HFETs and AlGaN/GaN Schottky-HFETs with the drain current noise PSD S_{I_D} as functions of the drain current I_D and the frequency f, at some values of the gate-source voltage V_G as examples. Figure 4.25 is for the HFETs having a gate length $L_G = 260$ nm

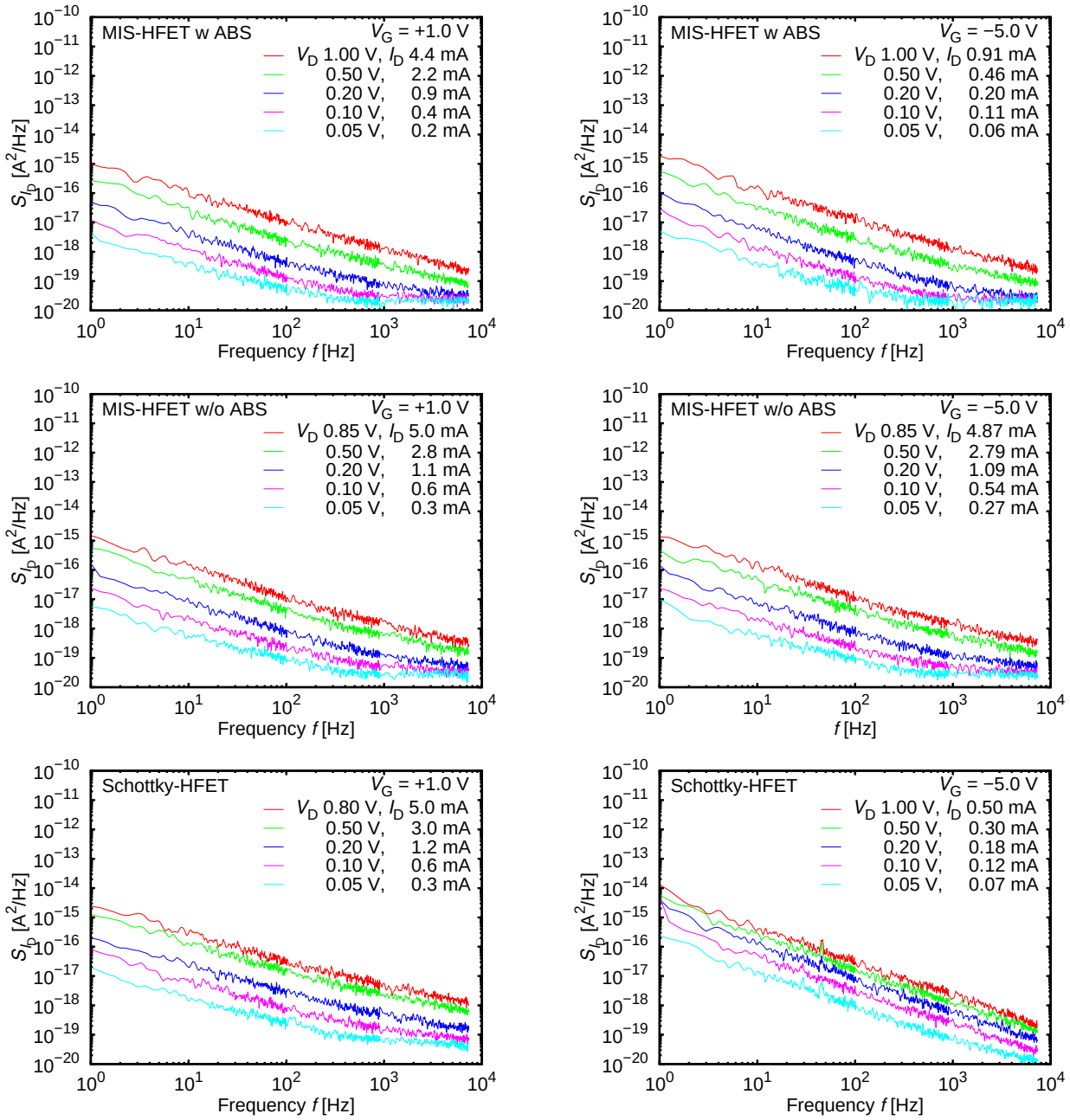

Figure 4.26: Low-frequency spectra of the drain current I_D noise of AlGaN/GaN HFETs having $L_G = 160$ nm and $W = 50$ μm with PSD S_{I_D} as functions of the frequency f. From the top to the bottom are for MIS w ABS, MIS w/o ABS and Schottky devices, respectively. The measurement results are for are for some gate-source voltages V_G as examples.

and Fig. 4.26 is for those having a gate length $L_G = 160$ nm. We observe

$$S_{I_D} \propto f^{\gamma}, \ \gamma \simeq 1 \tag{4.33}$$

for all measurements with $f \lesssim 1$ kHz. Neither specific bumps nor peaks are observed, indicating no generation-recombination noise due to specific high-density electron traps with a specific time constant as well as no external noise effects. The flat behavior at

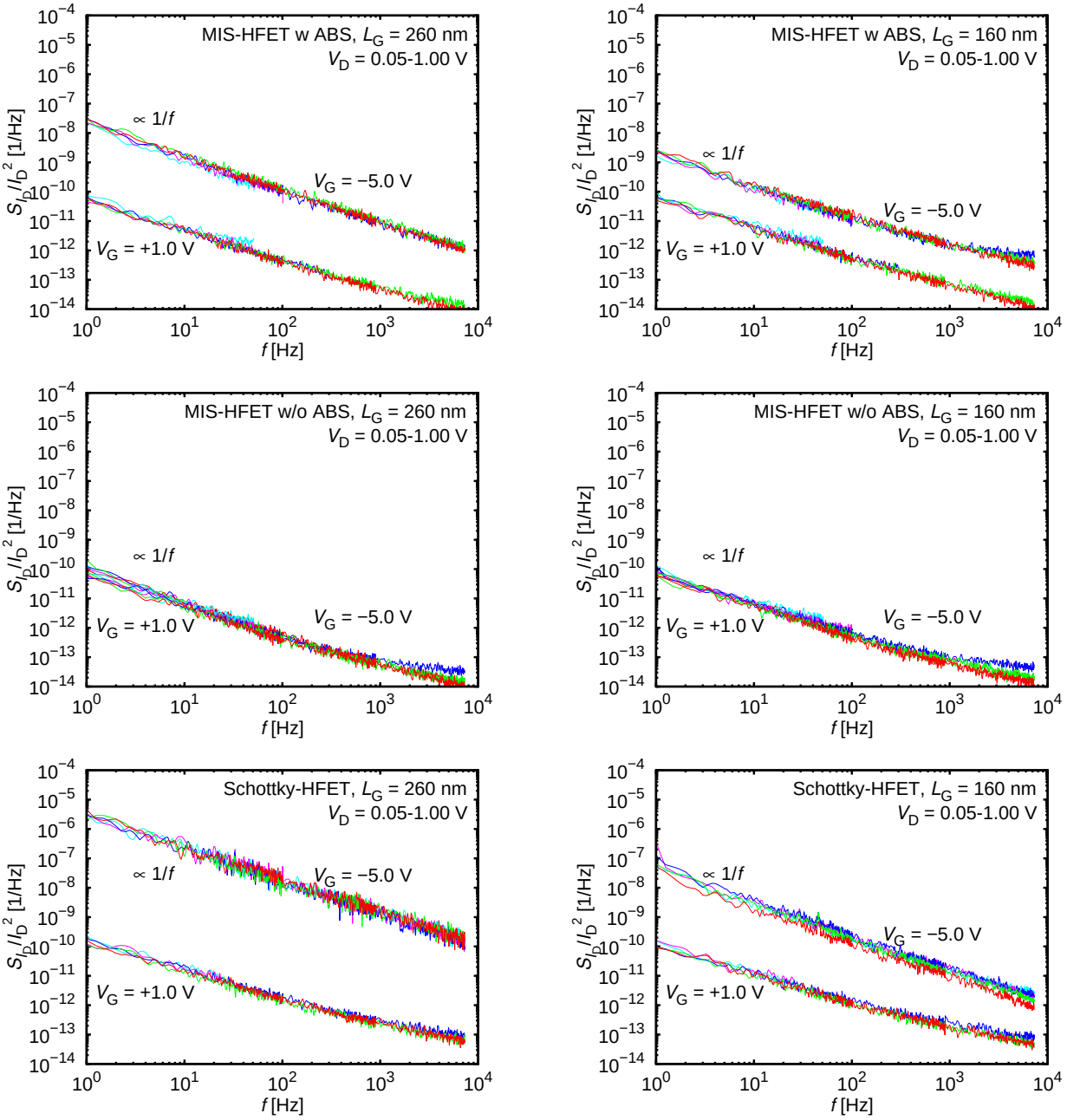

Figure 4.27: Low-frequency spectra of the drain current I_D noise of AlGaN/GaN HFETs having $L_G = 260$ nm (left), 160 nm (right) and $W = 50$ μm with $S_{I_D}/{I_D}^2$ as functions of the frequency f. From the top to the bottom are for MIS w ABS, MIS w/o ABS and Schottky devices, respectively. The measurement results are for some gate-source voltages V_G as examples.

high frequencies $f \gtrsim$ 1kHz in measurements with small currents is due to lower limit of the measurement system, as discussed in sections 2.2 and 4.2.

Figure 4.27 shows $S_{I_D}/{I_D}^2$ as functions of f. For the $1/f$ behavior domain, we realize that the normalized noise power $S_{I_D}/{I_D}^2$ seems to be a constant, independent of the current I_D, for a specific gate voltage V_G. This means that S_{I_D} may be proportional to the

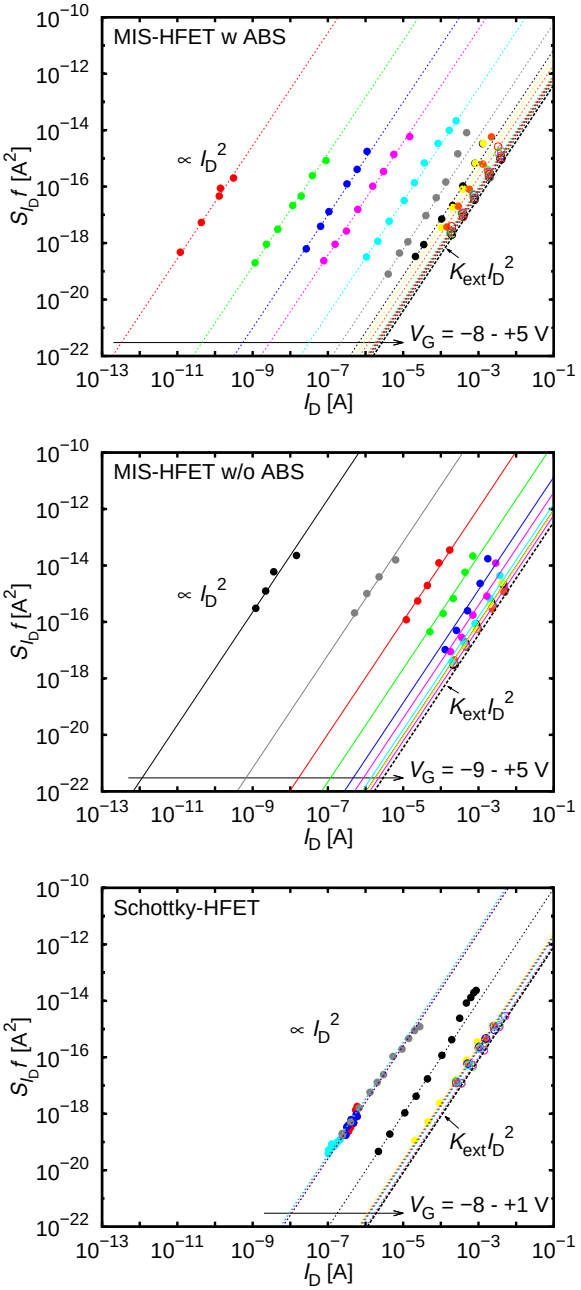

Figure 4.28: $S_{I_D} f$ as functions of the drain current I_D for AlGaN/GaN HFETs. From the top to the bottom are for MIS w ABS, MIS w/o ABS and Schottky HFETs having $L_G = 260$. The line indicated by $K_{ext} {I_D}^2$ is for the extrinsic part, which will be discussed in Eq. (4.47).

${I_D}^2$ with a proportion factor to be constant for a fixed gate voltage V_G, and depending on V_G. In order to clarify this, we plot $S_{I_D} f$ as function of the drain current I_D for some gate voltages V_G in whole measured range of V_G, as shown in Fig 4.28 for AlN/AlGaN/GaN MIS-HFETs and AlGaN/GaN Schottky-HFETs having gate length $L_G = 260$. From this figure, we can confirm the relation $S_{I_D} f \propto {I_D}^2$. This suggests a formula for the drain

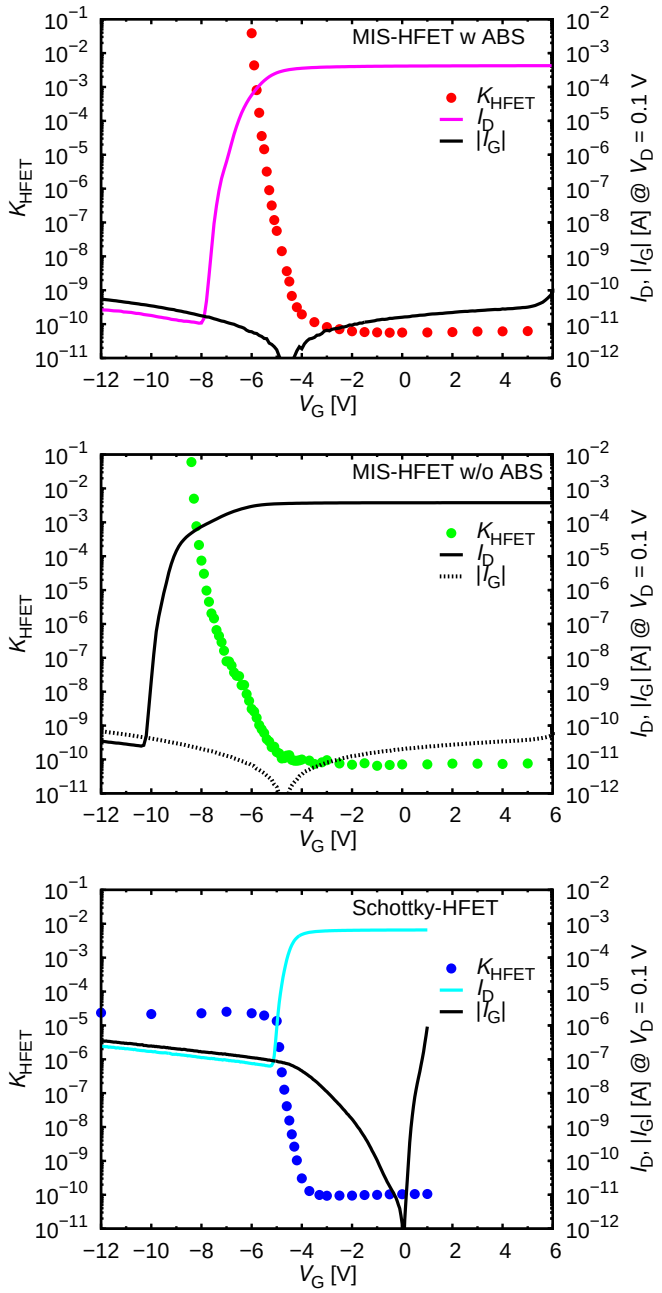

Figure 4.29: The factor K_{HFET}, the drain current I_{D} and the gate current I_{G} in linear regime with $V_{\mathrm{D}} = 0.1$ V, as functions of the gate-source voltage V_{G} for the HFETs having $L_{\mathrm{G}} = 260$.

current noise spectra

$$S_{I_{\mathrm{D}}} \simeq \frac{K_{\mathrm{HFET}} {I_{\mathrm{D}}}^2}{f}, \tag{4.34}$$

with a constant factor K_{HFET} depending on the fixed gate bias V_{G}, where the drain current I_{D} is varied by changing the drain voltage V_{D}. The factor K_{HFET} for the HFETs as a function of the V_{G} is plotted in Fig. 4.29, where the drain current I_{D} and gate current I_{G} for $V_{\mathrm{D}} = 0.1$ V in the linear regime are simultaneously shown. For the Schottky-HFETs,

we realize a singular behavior of the factor K_{HFET} at $V_{\mathrm{G}} \simeq -5.0$ V, in the regime below this voltage (high negative gate-source biases), the factor K_{HFET} exhibits a weak change. This is not observed for the MIS-HFETs.

We realize that the flat behavior of K_{HFET} for the Schottky-HFETs at high negative gate-source voltages corresponds to the regime in which the gate leakage current dominates the drain current $|I_{\mathrm{G}}| > I_{\mathrm{D}}$, as seen from the transfer characteristics in Fig. 4.15, and also in Fig. 4.29(c). As a result, the low-frequency noise is also dominated by the gate leakage. Hence, we attribute this behavior to the gate leakage current noise, which may be important in the high leakage domain. In the small leakage domain of the MIS-HFETs, $|I_{\mathrm{G}}| > I_{\mathrm{D}}$ at high negative gate-source voltages is also observed as seen in Figs. 4.15, but we cannot detect the $1/f$ noise in this region due to measurement limit (the current is very small, the noise level is also very small, lower than the measurement noise floor). We tentatively conclude that the gate leakage-dominated low-frequency noise is specific for the Schottky-HFETs with very leakage currents. In order to clarify the gate leakage-dominated low-frequency noise, we plot $S_{I_{\mathrm{D}}} f$ as function of the gate leakage current I_{G} for the regime $V_{\mathrm{G}} \lesssim -5.0$ V (in which the gate leakage dominates the drain current), shown in Fig. 4.30, which show $S_{I_{\mathrm{D}}} f \propto {I_{\mathrm{G}}}^2$. This result confirms that the low-frequency noise in the Schottky-HFETs in this regime is dominated by the gate leakage current.

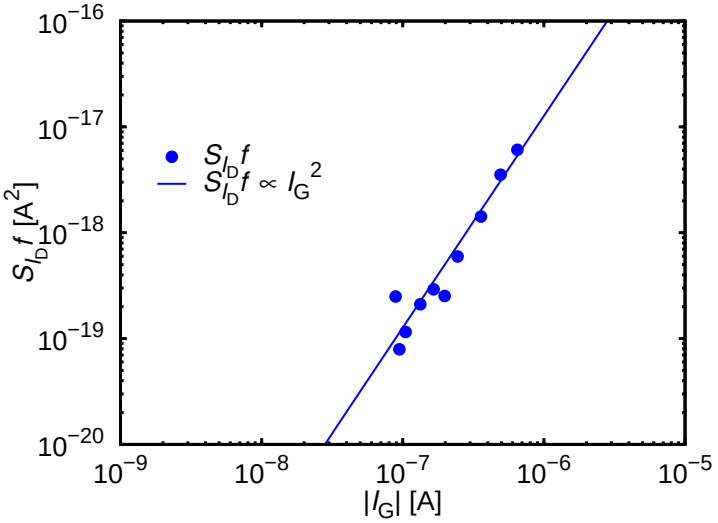

Figure 4.30: $S_{I_{\mathrm{D}}} f$ as a functions of gate current I_{G} for Schottky-HFETs with $V_{\mathrm{G}} \lesssim -5.0$ V.

We consider current components as follows

$$I_{\mathrm{G}} = I_{\mathrm{SG}} + I_{\mathrm{DG}} \tag{4.35}$$

$$I_{\mathrm{D}} = I_{\mathrm{SD}} - I_{\mathrm{DG}}, \tag{4.36}$$

where I_{SG} and I_{DG} are the leakage currents from the gate to source and to drain, and I_{SD} is the 2DEG (channel) current. When the gate leakage dominates the channel current

$$I_{\mathrm{D}} = I_{\mathrm{SD}} - I_{\mathrm{DG}} \simeq -I_{\mathrm{DG}}. \tag{4.37}$$

This implies the observed noise is a part of the noise generated by the gate leakage current. For the noise generated by the gate leakage current, we may have

$$S_{I_{\mathrm{G}}} \simeq \frac{K_{\mathrm{G}} {I_{\mathrm{G}}}^2}{f}, \tag{4.38}$$

this noise is not the intrinsic noise of the conduction channel (the noise of the gated 2DEG), it hence depends on the gate current itself, instead of the gate-source voltage. And the factor K_G for the gate current noise depends on the nature of gate current only, independent of the gate-source voltage. This explain why K_{HFET} is independent of gate-source voltage V_G at high negative V_G for the Schottky-HFETs, where the low-frequency noise is dominated by the gate leakage current. On the other hand, low-frequency noise in the MIS-HFETs is always dominated by only the 2DEG channel current.

With further increase of gate-source voltage V_G (more positive), the drain current quickly increases, dominates over the gate current $I_D \gg |I_G|$, and the noise is due to the 2DEG channel current. For the channel-current-dominated low-frequency noise, we should focus on the intrinsic noise by the gated region, depending on the gate bias. In order to clarify contributions from the intrinsic gated region and the extrinsic ungated part to the total drain current noise, we consider the source-drain conduction path of the HFETs as resistors in series schematically shown in Fig. 4.31.

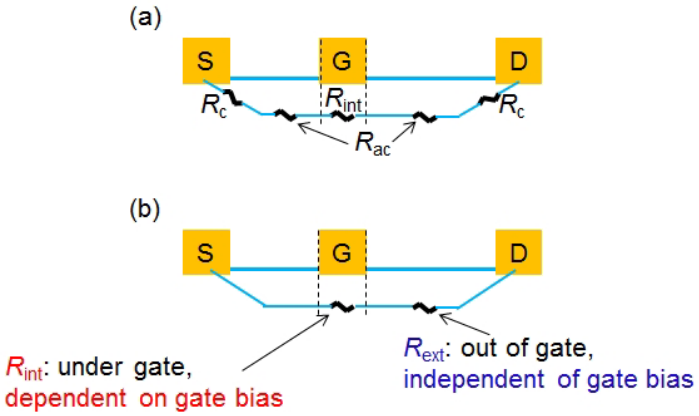

Figure 4.31: The schematic of the conduction path for the AlGaN/GaN HFETs with resistors in series. (a) Source-drain conduction path includes contact resistance R_c, access resistance R_{ac} (ungated 2DEG), and intrinsic under-gate resistance R_{int} (gated 2DEG). (b) Reduced source-drain conduction path includes intrinsic under-gate resistance R_{int} (intrinsic gated region) and extrinsic under-gate resistance R_{ext} (extrinsic gated part).

Since the total on-resistance R_{on} of the HFETs is the sum of the intrinsic resistance $R_{int} = r_s L_G/W$, where r_s is the sheet resistance of the gated region, depending on the gate voltage V_G and the extrinsic resistance R_{ext} of the ungated part

$$\begin{aligned} R_{on} &= R_{int} + R_{ac} + 2R_c \\ &= R_{int} + R_{ext}, \end{aligned} \tag{4.39}$$

where the extrinsic resistance R_{ext}, which is independent of V_G, is a sum of the contact resistances $R_c = r_c/W$ and the access resistance R_{ac} of the ungated 2DEG region. R_{ext} plays a same role as the total resistance of the ungated two-terminal devices.

By applying two-resistance-in-series model for R_{on} and using Eq. (3.9), we hence obtain the drain current noise PSD as

$$S_{I_D} = S_{I_D}^{int} \frac{{R_{int}}^2}{{R_{on}}^2} + S_{I_D}^{ext} \frac{{R_{ext}}^2}{{R_{on}}^2}, \tag{4.40}$$

where $S_{I_\mathrm{D}}^{\mathrm{int}}$ is the intrinsic noise generated by the gated region with under-gate resistance R_{int}, dependent on the gate-source voltage V_G; and $S_{I_\mathrm{D}}^{\mathrm{ext}}$ is the extrinsic noise generated by the ungated part with resistance R_{ext}, independent of V_G. We can easily realize that the contribution from the extrinsic part to S_{I_D} is always less than $S_{I_\mathrm{D}}^{\mathrm{ext}}$, hence when

$$S_{I_\mathrm{D}} \gg S_{I_\mathrm{D}}^{\mathrm{ext}}, \tag{4.41}$$

the drain current noise is dominated by the intrinsic noise,

$$S_{I_\mathrm{D}} \simeq S_{I_\mathrm{D}}^{\mathrm{int}} \frac{{R_{\mathrm{int}}}^2}{{R_{\mathrm{on}}}^2} \simeq S_{I_\mathrm{D}}^{\mathrm{int}}. \tag{4.42}$$

Using Eq. (4.40) for the factor K_{HFET}

$$K_{\mathrm{HFET}} = K_{\mathrm{int}} \frac{{R_{\mathrm{int}}}^2}{{R_{\mathrm{on}}}^2} + K_{\mathrm{ext}} \frac{{R_{\mathrm{ext}}}^2}{{R_{\mathrm{on}}}^2}, \tag{4.43}$$

where K_{int} is the factor for the intrinsic noise, dependent on the gate-source voltage V_G; and K_{ext} is the factor for the extrinsic noise, independent of the V_G. Plots of K_{HFET} as functions of the gate-source voltage V_G are shown in Fig. 4.29. We realize for the channel-current-dominated low-frequency noise that the factor K_{HFET} strongly depends on the gate bias when $V_\mathrm{G} \lesssim -4.0$ V, indicating the domination of the intrinsic noise. With further increase of the V_G (more positive), we realize that K_{HFET} becomes weakly dependent on the gate bias when $V_\mathrm{G} > -4.0$ V, implying a significant contribution of the extrinsic noise. When the gate bias is more positive, the intrinsic resistance becomes smaller (the drain current is large, as seen from the transfer characteristics), while the extrinsic resistance is unchanged. This leads to a stronger contribution of the extrinsic noise, with the increase of the second term in Eq. (4.43). Because the extrinsic noise with the factor K_{ext} is independent of the gate-source voltage V_G, the domination of the extrinsic noise leads to a weak dependence of the K_{HFET} on the V_G.

In order to evaluate the low-frequency noise behavior of the gated region, we have to excluded contribution of the ungated part (the second term in the Eqs. (4.40) and (4.43)) from the total drain current noise. For that purpose, we have to know $S_{I_\mathrm{D}}^{\mathrm{ext}}$ or K_{ext} and also R_{ext}. The extrinsic resistance R_{ext}, which is independent of the gate-source voltage V_G, is extracted from the Eq. (4.39) by measuring the total on resistance R_{on} as a function of V_G. We have

$$\begin{aligned} R_{\mathrm{on}} &= R_{\mathrm{int}} + R_{\mathrm{ext}} \\ &= r_\mathrm{s} \frac{L_\mathrm{G}}{W} + R_{\mathrm{ext}} \\ &= \frac{1}{e n_\mathrm{s} \mu} \frac{L_\mathrm{G}}{W} + R_{\mathrm{ext}}. \end{aligned} \tag{4.44}$$

By assuming that the mobility μ is weakly dependent on V_G near the zero regime, the V_G-dependence of R_{on} is owing to that of n_s in this regime, which shows $n_\mathrm{s} = \eta(V_\mathrm{G} - V_\mathrm{T}) \propto (V_\mathrm{G} - V_\mathrm{T})$ with the proportion factor η, where V_T is the threshold voltage, as seen in Fig. 4.36. According to these, Eq. (4.44) becomes

$$\begin{aligned} R_{\mathrm{on}} &= \frac{1}{e n_\mathrm{s} \mu} \frac{L_\mathrm{G}}{W} + R_{\mathrm{ext}} \\ &= \frac{1}{e \eta (V_\mathrm{G} - V_\mathrm{T}) \mu} \frac{L_\mathrm{G}}{W} + R_{\mathrm{ext}}. \end{aligned} \tag{4.45}$$

Figure 4.32 shows the on resistance R_{on}, which was obtained by $I_D V_G$ measurements in the linear regime with source-drain voltage $V_D = 0.1$ V, as a function of V_G with the lines of extrinsic resistance R_{ext}, obtained by fitting the data points with equation

$$R_{on} = \frac{a}{V_G + b} + R_{ext}, \tag{4.46}$$

basing on Eq. (4.45), where a and b are fitting parameters. The values of the R_{ext} for the HFETs are summarized in the Table 4.7

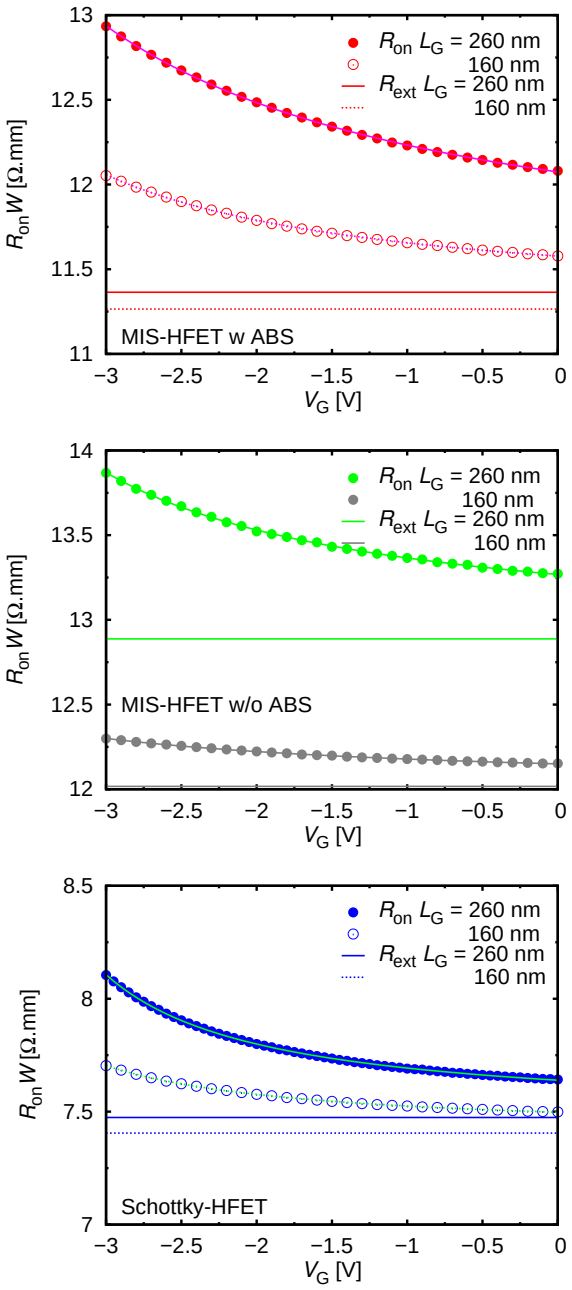

Figure 4.32: On resistance R_{on} of the HFETs as a function of V_G, obtained with $V_D = 0.1$ V.

L_G	MIS w ABS	MIS w/o ABS	Schottky
260 nm	11.4 Ω.mm	12.9 Ω.mm	7.5 Ω.mm
160 nm	11.3 Ω.mm	12.0 Ω.mm	7.4 Ω.mm

Table 4.7: Extrinsic resistance $R_{ext}W$ of the HFETs.

After determination of the extrinsic resistance R_{ext}, the extrinsic noise $S_{I_D}^{ext}$ of the ungated part is determined in combination with the ungated two-terminal devices. The ungated part of the HFETs, which includes two Ohmic contact electrodes and ungated 2DEG region, is similar to the ungated two-terminal devices. As discussed in the section 4.3.1 for the ungated two-terminal devices, the $S_{I_D}^{ext}$ can be expressed by a Hooge-like formula

$$S_{I_D}^{ext} = \frac{K_{ext} {I_D}^2}{f}, \tag{4.47}$$

where K_{ext} is the factor for ungated part, in a correlation with R_{ext} as in Fig. 4.33.

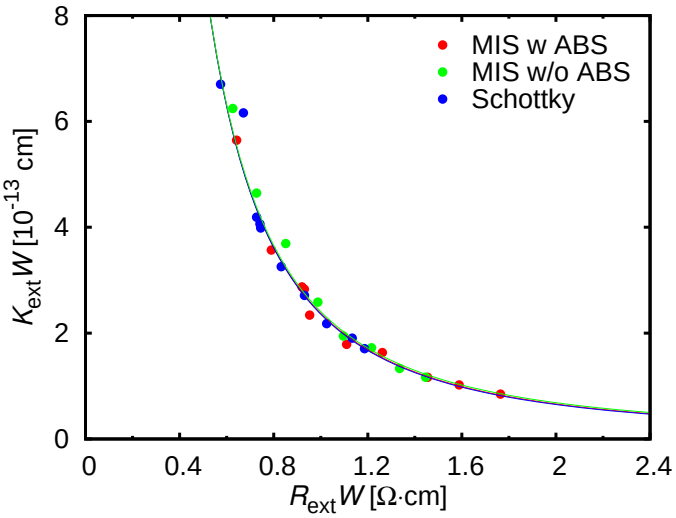

Figure 4.33: $K_{ext}W$ as functions of $R_{ext}W$ for the HFETs, obtained from measurements with the ungated two-terminal devices.

By using this correlation, we can obtain the factor K_{ext}, as shown in Table 4.8 for the HFETs. The $K_{ext}{I_D}^2$ is shown by the dotted lines in Fig. 4.28 for the $S_{I_D}f$ as functions of the drain current I_D. We realize that the data points approach the line for the large V_G, indicating the increase of the extrinsic noise contribution. The larger V_G, the smaller R_{int}, and the stronger contribution from the ungated part.

L_G	MIS w ABS	MIS w/o ABS	Schottky
260 nm	4.0×10^{-11}	3.2×10^{-11}	8.2×10^{-11}
160 nm	4.1×10^{-11}	3.6×10^{-11}	8.4×10^{-11}

Table 4.8: The factor K_{ext} for the HFETs.

The contribution from the extrinsic part is evaluated by using the factor K_{ext} and resistance R_{ext}. In order to clarify how dominant of the extrinsic noise, i.e., how important of the intrinsic noise at the positive gate bias voltages where data points approach the line of $K_{\mathrm{ext}}{I_{\mathrm{D}}}^2$, we consider contribution from the noise components given in Eq. (4.43), and plot them in Fig. 4.34. We realize that the contribution from the extrinsic noise dominates the total K_{HFET}, however, the contribution from the intrinsic noise is also significant and cannot be negligible. This implies that the direct calculation of K_{int} by using Eq. (4.43) is meaningful (of course, the calculation is always mathematically meaningful).

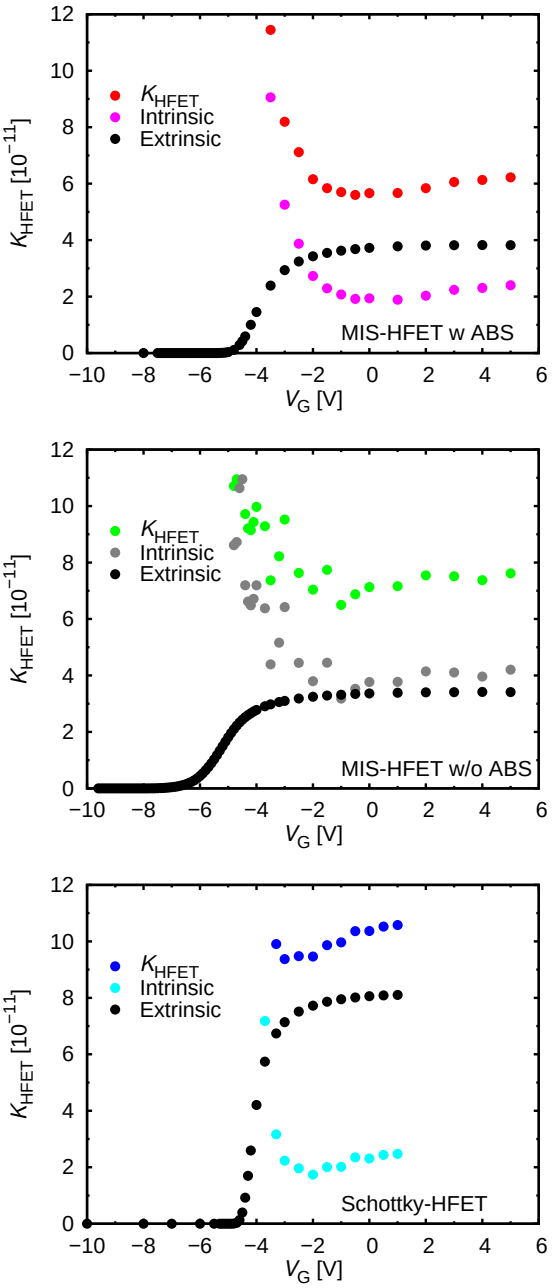

Figure 4.34: Contribution from intrinsic gated region and extrinsic ungated part for the HFETs having $L_{\mathrm{G}} = 260$ nm, calculated by Eq. (4.43).

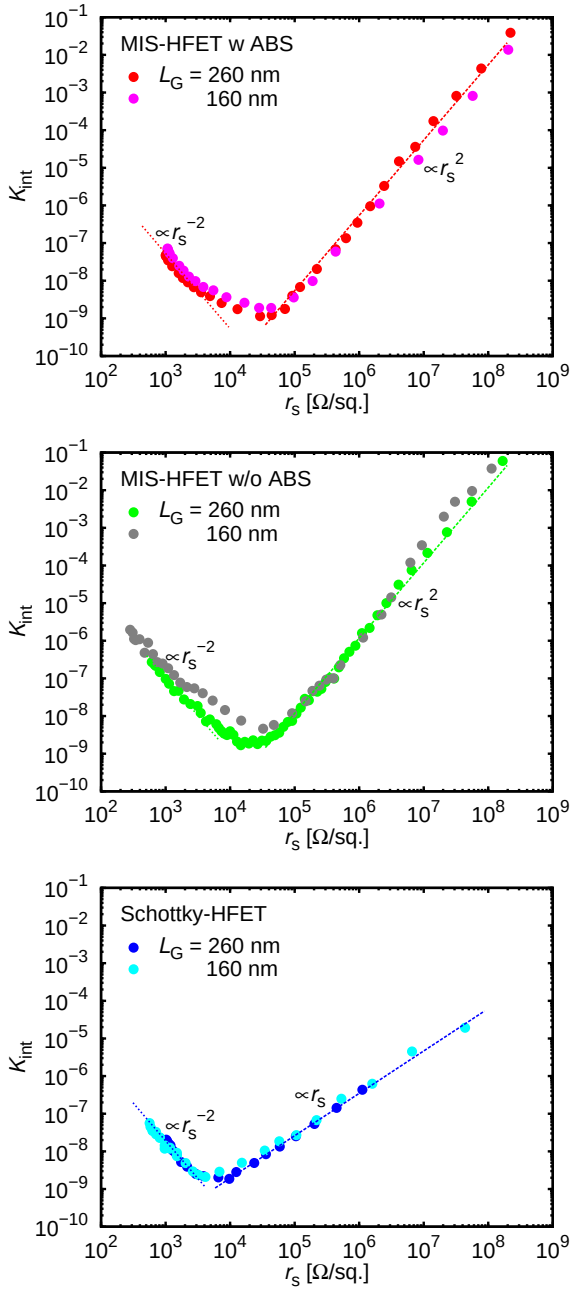

Figure 4.35: The factor $K_{\rm int}$ of the intrinsic gated region as functions of the under-gate sheet resistance $r_{\rm s}$ for the HFETs.

The factor $K_{\rm int}$ of the intrinsic gated region, obtained by using Eq. (4.43), as functions of the under-gate sheet resistance $r_{\rm s}$ are shown in Fig. 4.35. We can realize various $r_{\rm s}$-dependence of the $K_{\rm int}$: at small $r_{\rm s}$ ($\lesssim 10^4$ Ω/sq.), $K_{\rm int} \propto {r_{\rm s}}^{-2}$ for both MIS- and Schottky-HFETs; but at large $r_{\rm s}$ ($\gtrsim 10^4$ Ω/sq.), $K_{\rm int} \propto {r_{\rm s}}^{2}$ for MIS-HFETs, and $K_{\rm int} \propto r_{\rm s}$ for Schottky-HFETs. The different dependences of $K_{\rm int}$ on $r_{\rm s}$ imply the different noise mechanisms not only for different HFETs but also for the same HFETs under different operation conditions.

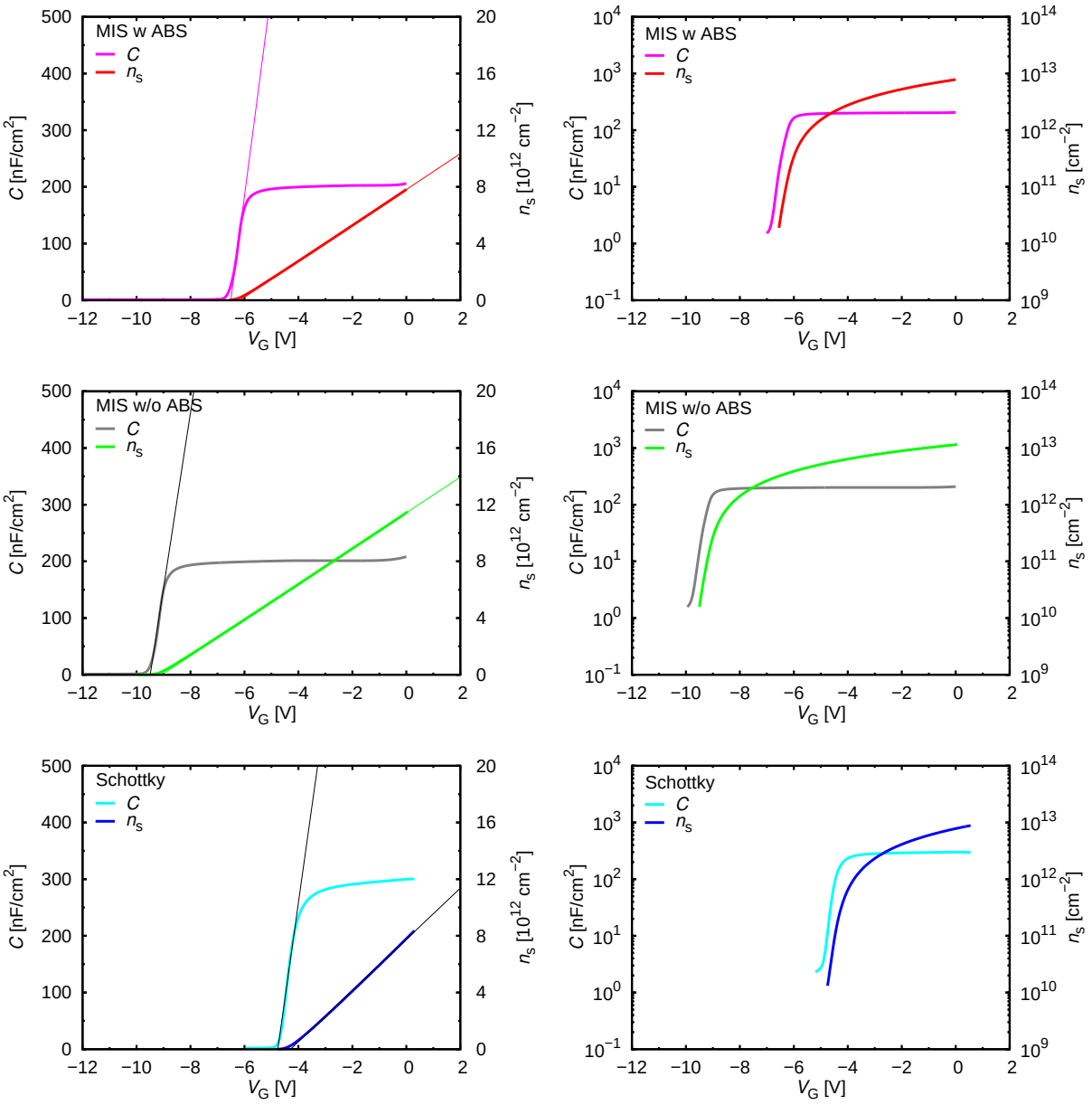

Figure 4.36: The capacitance C and under-gate sheet electron concentration n_s as functions of gate-source voltage V_G. The left (right) figures are for linear (logarithm) scale.

Moreover, in order to calculate the Hooge parameter of the intrinsic gated region $\alpha = K_{int}N$, where $N = L_G W n_s$ is the total carrier number under the gate with under-gate sheet electron concentration n_s, we estimated n_s using capacitance-voltage (C-V) measurements with the capacitors fabricated simultaneously with the HFETs. The results are shown in Fig. 4.36 for capacitance C (normalized by the capacitor area), under-gate sheet electron concentration n_s as functions of the gate-source voltage V_G. The under-gate sheet electron concentration n_s is calculated by an integration of C

$$n_s = \frac{1}{e}\int_{V_T}^{V} C\mathrm{d}V. \tag{4.48}$$

As a result, we can calculate the Hooge parameter of the intrinsic gated region for the HFETs, $\alpha = K_{\rm int} n_{\rm s} L_{\rm G} W$ and plot in Fig. 4.37 for α as functions of $n_{\rm s}$.

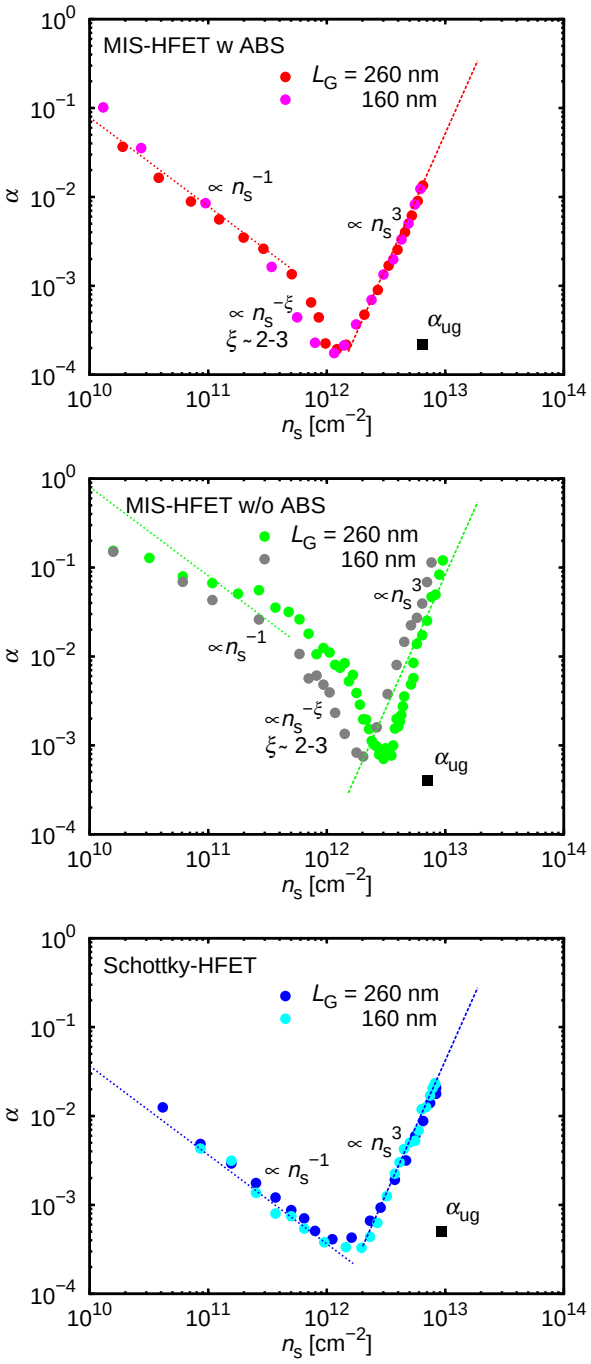

Figure 4.37: The Hooge parameters of the intrinsic gated region α as functions of the under-gate sheet electron concentration $n_{\rm s}$ for HFETs with the points of ungated two-terminal devices (square black points).

We realize that $\alpha \propto {n_{\rm s}}^{-1}$ at low electron concentration $n_{\rm s} \lesssim 10^{12}$ cm^{-2}, and $\alpha \propto {n_{\rm s}}^{3}$ at high electron concentration $n_{\rm s} \gtrsim 10^{12}$ cm^{-2} for both MIS-HFETs and Schottky-HFETs,

but $\alpha \propto {n_s}^{-\xi}$ with $\xi \sim$ 2-3 only for MIS-HFETs at moderate electron concentration 5×10^{11} cm$^{-2} \lesssim n_s \lesssim 10^{12}$ cm^{-2}.

By reminding Eq. (3.27) for Hooge parameter

$$\alpha = \frac{1}{\ln(f_h/f_\ell)} \left(\frac{(\delta\mu)^2}{\mu^2} + \frac{(\delta N)^2}{N} \right), \tag{4.49}$$

we will consider the n_s-dependence of α as follows. The behavior of $\alpha \propto {n_s}^{-1}$ is also often observed in GaN-based Schottky-HFETs and MOSFET [79, 83], and can be attributed to the electron-number fluctuation due to traps near the AlGaN/GaN interface. For a domination of the carrier-number fluctuation

$$\alpha \ln \frac{f_h}{f_\ell} \simeq \frac{(\delta N)^2}{N}. \tag{4.50}$$

The electron-number fluctuation due to electron traps of a density D_0 (see Appendix E)

$$(\delta N)^2 \simeq LWD_0 k_B T. \tag{4.51}$$

Using Eq. (4.50-4.51), we obtain

$$\alpha \ln \frac{f_h}{f_\ell} \simeq \frac{D_0 k_B T}{n_s} \propto {n_s}^{-1}. \tag{4.52}$$

This explains the $\alpha \propto {n_s}^{-1}$ behavior. According to this with the experimental data, we can obtain $\alpha \propto {n_s}^{-1}$ with the trap density $D_0 \sim 10^{11}$ cm^{-2}eV^{-1}, which is reasonable for the AlGaN/GaN interface. It is natural to consider that this behavior should be significantly influenced by the AlN/AlGaN interface states in the MIS-HFETs, whose density is rather high, 10^{13} cm^{-2}eV^{-1} order or more for energy levels near the AlGaN conduction band bottom [106, 107]. However, the HFETs show $\alpha \simeq 6.8 \times 10^8$ cm$^{-2} \times {n_s}^{-1}$ for MIS devices w ABS, $\alpha \simeq 7.8 \times 10^9$ cm$^{-2} \times {n_s}^{-1}$ for MIS devices w/o ABS, and $\alpha \simeq 4.4 \times 10^8$ cm$^{-2} \times {n_s}^{-1}$ for Schottky devices, giving D_0 of order 10^{11} cm^{-2}eV^{-1}. In this gate bias regime, AlN/AlGaN interface state energy levels corresponding to the Fermi energy are deep and have extremely long trapping time constants, for example, calculated to be $\sim 5 \times 10^3$ s for 0.7 eV below the AlGaN conduction band bottom [106]. As a result, trapped electrons at the AlN/AlGaN interface states almost freeze and, consequently, hardly contribute to the electron number fluctuation. We consider that, for both the MIS- and Schottky-HFETs, the observed $D_0 \sim 10^{11}$ cm^{-2}eV^{-1} is reasonable for traps in AlGaN close to the AlGaN/GaN interface, which have much shorter time constants.

On the other hand, for 5×10^{11} cm$^{-2} \lesssim n_s \lesssim 1 \times 10^{12}$ cm^{-2}, α decreases rapidly like ${n_s}^{-\xi}$ with $\xi \sim$2-3 for the MIS-HFETs, which is not observed for the Schottky-HFETs. We tentatively assume that this behavior is attributed to the mobility fluctuation specific for the MIS-HFETs. Moreover, we obtain strong increase in $\alpha \propto {n_s}^3$ for $n_s \gtrsim 2 \times 10^{12}$ cm^{-2}. Strong increase in α for large V_G and n_s is also observed in the Schottky-HFETs, sometimes being attributed to large gate leakage currents [83]. However, in the MIS-HFETs, this behavior cannot be attributed to the gate leakage, which is significantly suppressed, but can be related to the fluctuation in the intrinsic gate voltage, which is enhanced for large V_G and n_s by the fluctuation of the voltage across the extrinsic source resistance. According to this, α of the gated region is larger than α_{ug} of the ungated region for the same sheet electron concentration, as confirmed in the Fig. 4.37. Even for the intrinsic gated region, the low-frequency noise can be influenced by the extrinsic part through the fluctuation of the intrinsic gate voltage.

4.4 Summary

We fabricated AlN/AlGaN/GaN MIS devices, i.e., HFETs as well as ungated two-terminal devices. The same sets of AlGaN/GaN Schottky devices, HFETs and ungated two-terminal devices, were fabricated simultaneously. The MIS-HFETs show good insulating properties of the AlN insulator, which may be important for future electronic device applications.

Using the fabricated devices, we systematically investigated low-frequency noise characteristics of the AlN/AlGaN/GaN MIS devices in comparison with the Schottky devices, clarifying the behavior of the intrinsic gated region, and its dependence on the transport properties. In combination with investigation of low-frequency noise in AlGaN/GaN ungated two-terminal devices, we extracted low-frequency noise behaviors of the intrinsic gated region in the MIS- and Schottky-HFETs.

Hooge parameters of the ungated two-terminal devices, estimated from the size dependence of the factor K, are $\sim 2 \times 10^{-4}$ and $\sim 5 \times 10^{-4}$ for MIS and Schottky devices, respectively; and can be attributed to phonon-scattered mobility fluctuations. The intrinsic noise characteristics of gated region of the HFETs were studied by excluding the contribution from the gated part. The Hooge parameter of the intrinsic gated region of the HFETs $\alpha \propto {n_\mathrm{s}}^{-1}$ at low electron concentration $n_\mathrm{s} \lesssim 10^{12}$ cm^{-2}, which can be attributed to electron number fluctuation due to traps near the AlGaN/GaN interface. In addition, $\alpha \propto {n_\mathrm{s}}^{3}$ at high electron concentration $n_\mathrm{s} \gtrsim 10^{12}$ cm^{-2} may be related to the fluctuation in the intrinsic gate voltage, which is enhanced for large V_G and n_s by the fluctuation of the voltage across the extrinsic source resistance. Moreover, for 5×10^{11} cm$^{-2} \lesssim n_\mathrm{s} \lesssim 1 \times 10^{12}$ cm^{-2}, α decreases rapidly like ${n_\mathrm{s}}^{-\xi}$ with $\xi \sim$2-3 only for the MIS-HFETs, which is not observed for the Schottky-HFETs. We tentatively assume that this behavior is attributed to the mobility fluctuation specific for the MIS-HFETs.

Chapter 5

Conclusion and future perspectives

5.1 Conclusion of this work

Low-frequency noise in narrow- and wide-gap III-V compound semiconductors were systematically investigated for InAs (narrow-gap) and GaN (wide-gap) devices. We clarified detailed behaviors of the Hooge parameter depending on the devices.

1. In order to clarify the low-frequency noise characteristics of the III-V compound semiconductor devices, we established a low-frequency noise measurement system with different configurations for two-terminal devices and three-terminal devices. The system is tested and shows:

- A good cut-off frequency of about 0.05 Hz with a good frequency roll-off about -20 dB/decade. These properties ensure no contribution of low-frequency noise from the SMU to the devices.
- A stable and low noise floors, which give lower detectable signal limits for the measurements to be sure that the device signal is not emerged by the system background.
- A good shielding property, which is confirmed by the system noise floors without any unusual peaks or bumps. This property ensures that the measurement results are not affected by the external effects.

2. Using the established low-frequency noise measurement system, we investigated low-frequency noise characteristics of the devices fabricated from InAs films bonded on low-k flexible substrate (InAs/FS) in comparison with those of devices fabricated from InAs films grown on GaAs(001) substrate (InAs/GaAs). Moreover, we systematically investigated low-frequency noise characteristics of AlN/AlGaN/GaN MIS devices including HFETs as well as ungated two-terminal devices, comparing with the Schottky devices, and clarifying the behavior of the intrinsic gated region and its dependence on the transport properties. We observed low-frequency current noise in the devices with various characteristics depending on the devices.

The InAs- and GaN-based devices showed current noise with $1/f$ behavior at frequency ranging from 1 Hz to 10 kHz. The noise power spectrum density S_I satisfies $S_I/I^2 = K/f$ with the current I flowing through the device and a constant factor K depending on the device characteristics. No specific bump suggests no specific high-density electron traps with a specific time constant.

For the InAs-based devices

- $KW \propto L$ for a long range of L, where L and W are device length and width, indicating negligible contribution of the electrode contact.

- Hooge parameter defined as $\alpha = KN = Kn_{\rm s}LW$, where $n_{\rm s}$ is conducting channel sheet electron concentration, is inversely proportional to $\mu n_{\rm s}$ for both InAs/FS and InAs/GaAs.

- For InAs/FS with thickness $d \gtrsim 20$ nm, where μ weakly changes, $\alpha \propto {n_{\rm s}}^{-1}$ is observed and attributed to the carrier-number fluctuation $(\delta N)^2 \sim LWD_{\rm i}k_{\rm B}T$, where the interface state density $D_{\rm i} \sim 10^{12}$ cm^{-2}eV^{-1} is obtained from the data, being consistent with the Coulomb-scattering mobility.

- For InAs/FS with $d \lesssim 20$ nm and InAs/GaAs(001), where $n_{\rm s}$ weakly changes, $\alpha \propto \mu^{-1}$ is observed, which can be related to the mobility fluctuation due to fluctuations in the InAs film thickness.

For the GaN-based devices

- $KW \simeq$ *constant* tendency for small L, indicating significant contribution of the electrode contacts. $K_{\rm c}W \simeq 1.9 \times 10^{-12}$ cm for one contact, which is common for the MIS and Schottky devices because of the same Ohmic process.

- Hooge parameters of the ungated two-terminal devices, estimated from the size dependence of the factor K, are $\alpha_{\rm ug} \simeq 2.2 \times 10^{-4}$ for the MIS devices w ABS, 4.1×10^{-4} for the MIS devices w/o ABS, and 5.0×10^{-4} for the Schottky devices, respectively. The smaller $\alpha_{\rm ug}$ in the MIS devices can be attributed to the lower electron mobility due to additional scattering mechanisms caused by the AlN insulator deposition, where the mobility fluctuation dominates $\alpha_{\rm ug}$ according to the Hooge theory.

- From the ungated-device characterization, LFN behavior in the intrinsic gated region was extracted for the HFETs.

- For the MIS-HFETs with the small $n_{\rm s} \lesssim 5 \times 10^{11}$ cm^{-2}, $\alpha \propto {n_{\rm s}}^{-1}$, also observed for Schottky-HFETs with $n_{\rm s} \lesssim 10^{12}$ cm^{-2}, and is attributed to the carrier-number fluctuation due to electron traps with density $D_0 \sim 10^{11}$ cm^{-2}eV^{-1} in the AlGaN.

- On the other hand, for 5×10^{11} cm$^{-2} \lesssim n_{\rm s} \lesssim 1 \times 10^{12}$ cm^{-2}, the MIS-HFETs show α decreases rapidly like $\alpha \propto {n_{\rm s}}^{-\xi}$ with $\xi \sim$ 2-3, which is not observed for Schottky-HFETs, and tentatively attributed to the mobility fluctuation specific for the MIS-HFETs.

- Moreover, $\alpha \propto {n_{\rm s}}^3$ for both MIS- and Schottky-HFETs with $n_{\rm s} \gtrsim 2 \times 10^{12}$ cm^{-2}, can be attributed to the fluctuation in the intrinsic gate voltage, which is enhanced for large gate voltage and large $n_{\rm s}$ by the fluctuation of the voltage across the extrinsic source resistance.

It is natural to consider that the behavior $\alpha \propto {n_{\rm s}}^{-1}$, which is attributed to the carrier-number fluctuation due to electron traps, should be significantly influenced by the heterostructure interface states in the compound semiconductor devices. This conclusion is clearly discussed in chapter 3 for InAs devices. However, this behavior is not attributed to the trapping/detrapping process due to the interface states in GaN devices (as discussed in chapter 4) even there exist dirty interfaces between AlN/AlGaN with high-density states. In order to consider this contrast, we have to discuss on the time constant of the electron traps as follows. The time constant τ can be given by [106, 108]

$$\tau = \frac{1}{v_{\rm th}\sigma_{\rm e}N_{\rm c}}e^{\beta E_{\rm a}} \tag{5.1}$$

$$= \tau_0 e^{\beta E_{\rm a}}, \tag{5.2}$$

where $v_{\rm th}$ is the electron thermal velocity, calculated to be $\simeq 7.6 \times 10^7$ and $\simeq 2.6 \times 10^7$ cm/s at room temperature for InAs and GaN, respectively, $\sigma_{\rm e}$ is the electron capture cross-section, $N_{\rm c}$ is the effective density of states in the conduction band, calculated to be $\simeq 9.0 \times 10^{16}$ and $\simeq 2.3 \times 10^{18}$ cm^{-3} at room temperature for InAs and GaN, respectively, $E_{\rm a}$ is the activation energy, $\beta = k_{\rm B}T$ with the Boltzmann constant $k_{\rm B} = 1.38 \times 10^{-23}$ J/K and temperature T, and

$$\tau_0 = \frac{1}{v_{\rm th}\sigma_{\rm e}N_{\rm c}}. \tag{5.3}$$

$\tau_0 \simeq 10$ ns was experimentally obtained [106], from which we obtained $\sigma_0 \simeq 2 \times 10^{-18}$ cm^2. Using this cross-section, we plotted the electron trapping time constant as a function of the activation energy as shown in Fig. 5.1.

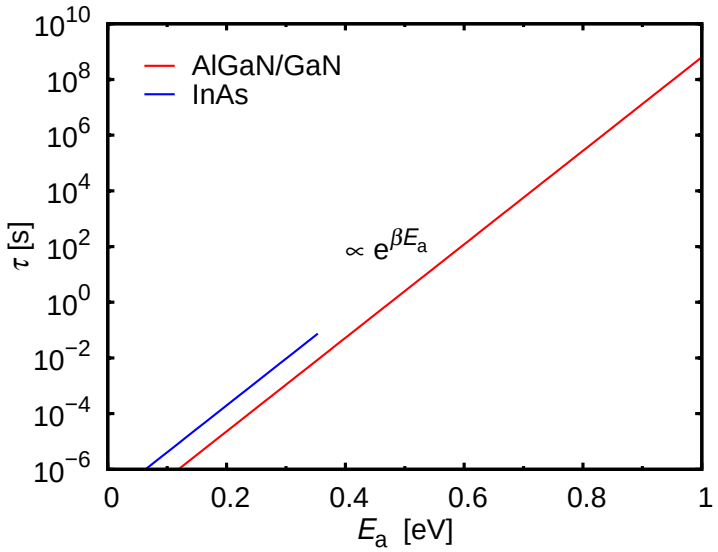

Figure 5.1: The time constant of the electron traps as functions of the activation energy with calculation by using $\sigma_0 = 2 \times 10^{-18}$ cm^2.

InAs/substrate interface state energy levels is less than 0.32 eV (InAs bandgap is 0.32 eV), corresponding to a times constant less than 10^{-2} s order. The interface states with this time constant can contribute to the low-frequency noise with $f : 0 \rightarrow 10^4$ Hz through the carrier-number fluctuation by trapping/detrapping processes. Hence, the low-frequency noise in InAs devices is attributed to carrier-number fluctuation owing to the interface states.

However, the AlN/AlGaN interface state energy levels corresponding to the Fermi energy are deep (due to large bandgap of GaN, 3.4 eV) and have extremely long trapping time constants, for example, calculated to be $\sim 5 \times 10^3$ s for 0.7 eV below the AlGaN conduction band bottom [106]. As a result, trapped electrons at the AlN/AlGaN interface states almost freeze and, consequently, hardly contribute to the electron number fluctuation. We consider that, for both the MIS- and Schottky-HFETs, the observed $D_0 \sim 10^{11}$ cm^{-2}eV^{-1} is reasonable for traps in AlGaN close to the AlGaN/GaN interface, which have much shorter time constants.

5.2 Future perspectives of this work

A good low-frequency noise measurement system was established, and the device low-frequency noise characterization was clarified for room temperature. In the future, we will carry out further investigation for low-frequency noise characteristics of the AlGaN/GaN devices. For example, temperature-dependent low-frequency noise in AlN/AlGaN/GaN MIS-HFETs or low-frequency noise in other AlGaN/GaN MIS devices with different high-k insulators such as AlTiO (an alloy of Al_2O_3 and TiO_2) should be investigated in order to clarify the noise mechanisms as well as to improve the performances of the AlGaN/GaN devices.

Furthermore, this work focuses on the low-frequency noise in the linear regime of the device operation. Although the investigation of the low-frequency noise in the linear regime can give insights into the physics of the devices, almost the devices are operated in the saturation regime. Hence, in near future, we should characterize low-frequency noise in the saturation regime for both InAs and GaN devices.

Appendix A

Systematic errors in a noise measurement system

This appendix A is compiled by using a manual of the SR570 preamplifier originally supplied by the Standford Research. The systematic errors discussed here is the errors inherent from the low-frequency noise measurement system using such amplifier of SR570. The errors include the coupling phenomena, microphonics, and thermocouple effects.

The coupling phenomena include capacitive coupling, inductive coupling and resistive coupling. The capacitive coupling is caused by capacitors. An AC voltage from a nearby piece of apparatus can couple to a detector via a stray capacitance (C-stray). Although C-stray may be very small, the coupled noise may still be larger than a weak experimental signal. This is especially damaging if the coupled noise is synchronous (at the signal frequency). Cures for capacitive noise coupling include: (1) Removing or turning off the noise source. (2) Keeping the noise source far from the experiment (reducing C-stray). Do not bring the signal cables close to the noise source. (3) Installing capacitive shielding by placing both the experiment and detector in a metal box.

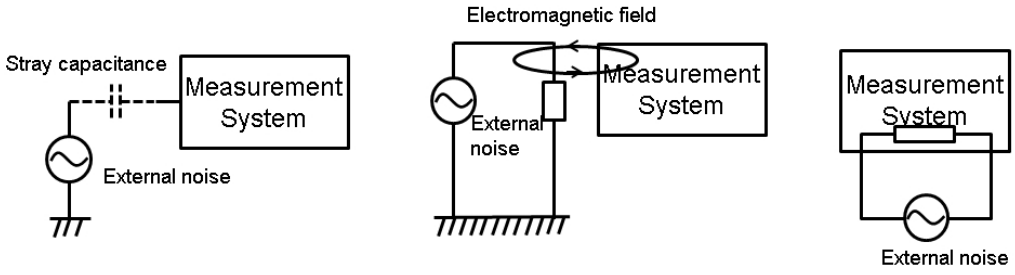

Figure A.1: Coupling phenomena in LFN measurement system: conductive coupling (left), inductive coupling (middle) and resistive coupling (right).

Inductive coupling results from inductance induced in the circuit. An AC current in a nearby piece of apparatus can couple to the experiment via a magnetic field. A changing current in a nearby circuit gives rise to a changing magnetic field which induces an electromagnetic field (emf) ($\mathrm{d}B/\mathrm{d}t$) in the loop connecting the detector to the experiment. This is like a transformer with the experiment-detector loop as the secondary winding. Cures for inductively coupled noise include: (1) Removing or turning off the interfering noise source. (2) Reduce the area of the pick-up loop by using twisted pairs or coaxial

cables, or even twisting the two coaxial cables used in differential connections. (3) Using magnetic shielding to prevent the magnetic field from crossing the area of the experiment. (4) Measuring currents, not voltages, from high impedance detectors.

Resistive coupling or ground loop is originated from the ground through the wire resistance. Currents flowing through the ground connections can give rise to noise voltages. This is especially a problem with signal frequency ground currents. Cures for ground loop problems include: (1) Grounding everything to the same physical point. (2) Using a heavy ground bus to reduce the resistance of ground connections. (3) Removing sources of large ground currents from the ground bus used for small signals.

Microphonics

Not all sources of noise are electrical in origin. Mechanical noise can be translated into electrical noise by microphonic effects. Physical changes in the experiment or cables (due to vibrations for example) can result in electrical noise over the entire frequency range of the amplifier. Some ways to minimize microphonic signals are: (1) Eliminate mechanical vibrations near the experiment. (2) Tie down cables carrying sensitive signals so they cannot move. (3) Use a low noise cable designed to reduce microphonic effects.

Thermocouple effects

The electromagnetic force (emf) created by junctions between dissimilar metals can give rise to many microvolts of slowly varying potentials. This source of noise is typically at very low frequency since the temperature of the detector and experiment generally changes slowly. This effect is large on the scale of many detector outputs and can be a problem for low frequency measurements, especially in the mHz range. Some ways to minimize thermocouple effects are: 1) Hold the temperature of the experiment or detector constant. 2) Use a compensation junction, i.e. a second junction in reverse polarity which generates an emf to cancel the thermal potential of the first junction (both held at the same temperature).

Appendix B

Coulomb scattering

B.1 Scattering matrix elements

Wave function of the unperturbed Hamiltonian is

$$\psi_{\mathbf{k},n}(\mathbf{r},z)=\varphi_n(z)e^{i\mathbf{k}\cdot\mathbf{r}}\equiv\mid\mathbf{k},n\rangle, \tag{B.1}$$

and the unscreened potential energy due to a charge at $\mathbf{r}_i$ and z_i is

$$V_i^0(\mathbf{r},z)=\frac{Z_ie^2}{4\pi\varepsilon_s[(\mathbf{r}-\mathbf{r}_i)^2+(z-z_i)^2]^{1/2}}. \tag{B.2}$$

The matrix elements for scattering is

$$\begin{aligned}
\langle\mathbf{k}',n\mid V_i^0(\mathbf{r},z)\mid\mathbf{k},m\rangle &= \frac{Z_ie^2}{4\pi\varepsilon_s}\int \mathrm{d}\mathbf{r}\mathrm{d}z\varphi_n^*(z)e^{-i\mathbf{k}'\cdot\mathbf{r}}\frac{1}{[(\mathbf{r}-\mathbf{r}_i)^2+(z-z_i)^2]^{1/2}}\varphi_m(z)e^{i\mathbf{k}\cdot\mathbf{r}}\\
&= \frac{Z_ie^2}{4\pi\varepsilon_s}\int \mathrm{d}z\varphi_n^*(z)\varphi_m(z)\int \mathrm{d}\mathbf{r}e^{i\mathbf{q}\cdot\mathbf{r}}\frac{1}{[(\mathbf{r}-\mathbf{r}_i)^2+(z-z_i)^2]^{1/2}}\\
&= \frac{Z_ie^2}{2\varepsilon_s}\int \mathrm{d}z\rho_{mn}(z)\int \mathrm{d}\mathbf{r}e^{i\mathbf{q}\cdot\mathbf{r}}\int \mathrm{d}\mathbf{q}'\frac{e^{-q'(z-z_i)}e^{i\mathbf{q}'\cdot(\mathbf{r}-\mathbf{r}_i)}}{q'}\\
&= \frac{Z_ie^2}{2\varepsilon_s}\int \mathrm{d}z\rho_{mn}(z)\int \mathrm{d}\mathbf{q}'\frac{e^{-q'(z-z_i)}e^{-i\mathbf{q}'\cdot\mathbf{r}_i}}{q'}\int \mathrm{d}\mathbf{r}e^{i(\mathbf{q}+\mathbf{q}')\cdot\mathbf{r}}\\
&= \frac{Z_ie^2}{2\varepsilon_s}\int \mathrm{d}z\rho_{mn}(z)\int \mathrm{d}\mathbf{q}'\frac{e^{-q'(z-z_i)}e^{-i\mathbf{q}'\cdot\mathbf{r}_i}}{q'}\delta(\mathbf{q}+\mathbf{q}')\\
&= \frac{Z_ie^2}{2\varepsilon_s}\int \mathrm{d}z\rho_{mn}(z)\frac{e^{-q(z-z_i)}e^{i\mathbf{q}\cdot\mathbf{r}_i}}{q}\\
&= V_{i,nm}^0(q,z_i)e^{i\mathbf{q}\cdot\mathbf{r}_i},
\end{aligned} \tag{B.3}$$

where $\mathbf{q}=\mathbf{k}-\mathbf{k}'$, $\rho_{mn}(z)=\varphi_n^*(z)\varphi_m(z)$,

$$V_{i,nm}^0(q,z_i)=\frac{Z_ie^2}{2\varepsilon_s}\int \rho_{mn}(z)\frac{e^{-q(z-z_i)}}{q}\mathrm{d}z, \tag{B.4}$$

and we used the Fourier transformation

$$\frac{1}{[(\mathbf{r}-\mathbf{r}_i)^2+(z-z_i)^2]^{1/2}}=2\pi\int \mathrm{d}\mathbf{q}'\frac{e^{-q'(z-z_i)}e^{i\mathbf{q}'\cdot(\mathbf{r}-\mathbf{r}_i)}}{q'}. \tag{B.5}$$

For all impurities in the system, the screened potential including the wavevector dependent dielectric constant, hence

$$V^i_{nm}(q) = \sum_i e^{i\mathbf{q}\cdot\mathbf{r}_i} \frac{V^0_{i,nm}(q,z_i)}{\epsilon_D(q)}, \tag{B.6}$$

where $\epsilon_D(q)$ is scalar dielectric constant.

B.2 Scattering probability

The elastic scattering rate for impurity scattering is given by Fermi golden rule

$$S^i_{nm}(\mathbf{k},\mathbf{k}') = \frac{2\pi}{\hbar} \mid V^i_{nm}(q) \mid^2 \delta(E_{\mathbf{k}'} - E_{\mathbf{k}} + E_n - E_m), \tag{B.7}$$

where

$$\begin{aligned} \mid V^i_{nm}(q) \mid^2 &= \Big(\sum_i e^{i\mathbf{q}\cdot\mathbf{r}_i} \frac{V^0_{i,nm}(q,z_i)}{\epsilon_D(q)}\Big)^* \Big(\sum_j e^{i\mathbf{q}\cdot\mathbf{r}_j} \frac{V^0_{j,nm}(q,z_j)}{\epsilon_D(q)}\Big) \\ &= \Big(\sum_i e^{-i\mathbf{q}\cdot\mathbf{r}_i} \frac{V^{0*}_{i,nm}(q,z_i)}{\epsilon^*_D(q)}\Big)\Big(\sum_j e^{i\mathbf{q}\cdot\mathbf{r}_j} \frac{V^0_{j,nm}(q,z_j)}{\epsilon_D(q)}\Big) \\ &= \sum_i \mid \frac{V^0_{i,nm}(q,z_i)}{\epsilon_D(q)} \mid^2 + \sum_{i\neq j} e^{-i\mathbf{q}\cdot(\mathbf{r}_i-\mathbf{r}_j)} \frac{V^{0*}_{i,nm}(q,z_i) V^0_{j,nm}(q,z_j)}{\mid \epsilon_D(q) \mid^2}, \end{aligned} \tag{B.8}$$

and with assumption that in any give plane parallel to interface that the position of the impurities is completely uncorrelated. Then the second terms cancel on the average, hence

$$\mid V^i_{nm}(q) \mid^2 = \sum_i \mid \frac{V^0_{i,nm}(q,z_i)}{\epsilon_D(q)} \mid^2 . \tag{B.9}$$

The scattering rate becomes

$$\begin{aligned} S^i_{nm}(\mathbf{k},\mathbf{k}') &= \frac{2\pi}{\hbar} \mid V^i_{nm}(q) \mid^2 \delta(E_{\mathbf{k}'} - E_{\mathbf{k}} + E_n - E_m) \\ &= \frac{2\pi}{\hbar} \int \mathrm{d}z_i N_i(z_i) \mid \frac{V^0_{i,nm}(q,z_i)}{\epsilon_D(q)} \mid^2 \delta(E_{\mathbf{k}'} - E_{\mathbf{k}} + E_n - E_m), \end{aligned} \tag{B.10}$$

where $N_i(z_i)$ is the density of impurities as a function of z_i, [cm^{-3}]. The momentum relaxation time (transport scattering rate) is

$$
\begin{aligned}
\frac{1}{\tau_n^i(E)} &= \sum_{\mathbf{k}'} S_{nm}^i(\mathbf{k},\mathbf{k}')(1-\cos\theta) \\
&= \frac{2\pi}{\hbar}\sum_{\mathbf{k}'} \mid V_{nm}^i(q) \mid^2 (1-\cos\theta)\delta(E_{\mathbf{k}'}-E_{\mathbf{k}}+E_n-E_m) \\
&= \frac{2\pi}{\hbar}\sum_{\mathbf{k}'} \int \mathrm{d}z_i N_i(z_i) \mid \frac{V_{i,nm}^0(q,z_i)}{\epsilon_D(q)} \mid^2 (1-\cos\theta)\delta(E_{\mathbf{k}'}-E_{\mathbf{k}}+E_n-E_m) \\
&= \frac{\pi Z_i^2 e^4}{2\hbar\varepsilon_s^2}\sum_{\mathbf{k}'} \int \mathrm{d}z_i \frac{N_i(z_i)}{q^2} \mid \frac{\int \mathrm{d}z\rho_{mn}(z)e^{-q(z-z_i)}}{\epsilon_D(q)} \mid^2 (1-\cos\theta)\delta(E_{\mathbf{k}'}-E_{\mathbf{k}}+E_n-E_m) \\
&= \frac{\pi Z_i^2 e^4}{2\hbar\varepsilon_s^2}\sum_{\mathbf{k}'} \int \mathrm{d}z_i N_i(z_i)\frac{e^{2qz_i}}{q^2\epsilon_D^2(q)}(1-\cos\theta) \mid \int \mathrm{d}z\rho_{mn}(z)e^{-qz} \mid^2 \delta(E_{\mathbf{k}'}-E_{\mathbf{k}}+E_n-E_m) \\
&= \frac{\pi Z_i^2 e^4}{2\hbar\varepsilon_s^2}\sum_{\mathbf{k}'} \int \mathrm{d}z_i N_i(z_i)\frac{e^{2qz_i}}{q^2\epsilon_D^2(q)}\mathcal{F}_n^2(q)(1-\cos\theta)\delta(E_{\mathbf{k}'}-E_{\mathbf{k}}), \qquad \text{(B.11)}
\end{aligned}
$$

where θ is the angle between $\mathbf{k}$ and $\mathbf{k}'$, and

$$
\mathcal{F}_n(q) = \int \mathrm{d}z\rho_{nn}(z)e^{-qz}. \qquad \text{(B.12)}
$$

We have the relation

$$
\sum_{\mathbf{k}'} = \frac{1}{(2\pi)^2}\int_0^{2\pi}\mathrm{d}\theta\int_0^{\infty} k'\mathrm{d}k' = \frac{1}{(2\pi)^2}\int_0^{2\pi}\mathrm{d}\theta\frac{m^*}{\hbar^2}\int_0^{\infty}\mathrm{d}E. \qquad \text{(B.13)}
$$

Equation (B.11) becomes

$$
\begin{aligned}
\frac{1}{\tau_n^i(E)} &= \frac{Z_i^2 m^* e^4}{8\pi\hbar^3\varepsilon_s^2}\int_0^{2\pi}\mathrm{d}\theta\int \mathrm{d}z_i N_i(z_i)\frac{e^{2qz_i}}{q^2\epsilon_D^2(q)}\mathcal{F}_n^2(q)(1-\cos\theta)\int_0^{\infty}\mathrm{d}E\delta(E_{\mathbf{k}'}-E_{\mathbf{k}}) \\
&= \frac{Z_i^2 m^* e^4}{8\pi\hbar^3\varepsilon_s^2}\int_0^{2\pi}\mathrm{d}\theta\int \mathrm{d}z_i N_i(z_i)\frac{e^{2qz_i}}{q^2\epsilon_D^2(q)}\mathcal{F}_n^2(q)(1-\cos\theta), \qquad \text{(B.14)}
\end{aligned}
$$

where the integral with delta function gives $\mid \mathbf{k} \mid = \mid \mathbf{k}' \mid$ and

$$
q = \mid \mathbf{k}-\mathbf{k}' \mid = \sqrt{k^2-k'^2-2kk'\cos\theta} = \sqrt{2k^2(1-\cos\theta)} = 2k\sin\frac{\theta}{2}. \qquad \text{(B.15)}
$$

B.3 Mobility limited by the charged impurities at the interfaces

If we consider impurity scattering due to a two-dimensional (2D) sheet of impurities, $N_i(z_i) = N_{ss}\delta(z_i)$ and we can neglect screening ($\epsilon_D(q) = 1$), Eq. (B.14) becomes

$$
\begin{aligned}
\frac{1}{\tau_n^i(E)} &= \frac{Z_i^2 m^* e^4 N_{ss}}{8\pi\hbar^3\varepsilon_s^2}\int_0^{2\pi}\mathrm{d}\theta\int \mathrm{d}z_i\delta(z_i)\frac{e^{2qz_i}}{q^2}\mathcal{F}_n^2(q)(1-\cos\theta) \\
&= \frac{Z_i^2 m^* e^4 N_{ss}}{8\pi\hbar^3\varepsilon_s^2}\int_0^{2\pi}\frac{\mathcal{F}_n^2(q)}{q^2}(1-\cos\theta)\mathrm{d}\theta. \qquad \text{(B.16)}
\end{aligned}
$$

Mobility limited by the charged impurities at the interfaces is

$$\begin{aligned}\frac{1}{\mu_i} &= \frac{m^*}{e\tau_n^i(E)} \\ &= \frac{Z_i^2 m^{*2} e^3 N_{ss}}{8\pi\hbar^3\varepsilon_s^2}\int_0^{2\pi}\frac{\mathcal{F}_n^2(q)}{q^2}(1-\cos\theta)\mathrm{d}\theta. \end{aligned} \tag{B.17}$$

By using Eq. (B.15), we obtain

$$\begin{aligned}\frac{1}{\mu_i} &= \frac{Z_i^2 m^{*2} e^3 N_{ss}}{8\pi\hbar^3\varepsilon_s^2}\int_0^{2\pi}\frac{\mathcal{F}_n^2(2k\sin\frac{\theta}{2})}{(2k\sin\frac{\theta}{2})^2}(1-\cos\theta)\mathrm{d}\theta \\ &= \frac{Z_i^2 m^{*2} e^3 N_{ss}}{16\pi\hbar^3\varepsilon_s^2 k^2}\int_0^{2\pi}\mathcal{F}_n^2(2k\sin\frac{\theta}{2})\mathrm{d}\theta \\ &= \frac{Z_i^2 m^{*2} e^3 N_{ss}}{8\pi\hbar^3\varepsilon_s^2 k^2}\int_0^{\pi}\mathcal{F}_n^2(2k\sin\frac{\theta}{2})\mathrm{d}\theta. \end{aligned} \tag{B.18}$$

By changing the variable $s = \sin(\theta/2)$, we get

$$\frac{1}{\mu_i} = \frac{Z_i^2 m^{*2} e^3 N_{ss}}{4\pi\hbar^3\varepsilon_s^2 k^2}\int_0^1\frac{\mathcal{F}_n^2(2ks)}{\sqrt{1-s^2}}\mathrm{d}s, \tag{B.19}$$

where

$$\mathcal{F}_n(q) = \int \mid \varphi_n(z) \mid^2 e^{-qz}\mathrm{d}z. \tag{B.20}$$

Appendix C

Fluctuation of two-variable functions

We consider fluctuation of a quantity that equals to product of two independent variables x and y: $z = xy$. If the product does not have statistical properties, i.e. that is simply the product of two quantities, the variance of the fluctuations of z is

$$\begin{aligned}
\sigma_z = (\delta z)^2 = \langle (z - \langle z \rangle)^2 \rangle &= \langle z^2 \rangle - \langle z \rangle^2 \\
&= \langle x^2 y^2 \rangle - \langle xy \rangle^2 \\
&= \langle x^2 \rangle \langle y^2 \rangle - \langle x \rangle^2 \langle y \rangle^2 \\
&= \langle x^2 \rangle \langle y^2 \rangle - \langle x^2 \rangle \langle y \rangle^2 + \langle x^2 \rangle \langle y \rangle^2 - \langle x \rangle^2 \langle y \rangle^2 \\
&= \langle x^2 \rangle \sigma_y + \langle y \rangle^2 \sigma_x \\
&= [\sigma_x + \langle x \rangle^2] \sigma_y + \langle y \rangle^2 \sigma_x \\
&= \sigma_x \sigma_y + \langle x \rangle^2 \sigma_y + \langle y \rangle^2 \sigma_x. \qquad \text{(C.1)}
\end{aligned}$$

Hence,

$$\begin{aligned}
\frac{\sigma_z}{\langle z \rangle^2} &= \frac{\sigma_x}{\langle x \rangle} \frac{\sigma_y}{\langle y \rangle} + \frac{\sigma_y}{\langle y \rangle^2} + \frac{\sigma_x}{\langle x \rangle^2} \\
&\simeq \frac{\sigma_y}{\langle y \rangle^2} + \frac{\sigma_x}{\langle x \rangle^2} \qquad \text{(C.2)}
\end{aligned}$$

if

$$\frac{\sigma_x}{\langle x \rangle} \ll 1, \text{ or } \frac{\sigma_y}{\langle y \rangle} \ll 1 \text{ (the first} - \text{order approximation)}. \qquad \text{(C.3)}$$

If the product has statistical properties, e.g.

$$z = Nx = \sum_{i=1}^{N} x_i \qquad \text{(C.4)}$$

the variance of the fluctuations of z is

$$\sigma_z = \langle z^2 \rangle - \langle z \rangle^2 = \big\langle (\sum_{i=1}^{N} x_i)^2 \big\rangle - \big\langle \sum_{i=1}^{N} x_i \big\rangle^2. \qquad \text{(C.5)}$$

Using Burgess theorem, we obtain

$$\big\langle \sum_{i=1}^{N} x_i \big\rangle = \big\langle \big\langle \sum_{i=1}^{N} x_i \big\rangle_{(x)} \big\rangle_{(N)} = \big\langle \sum_{i=1}^{N} \langle x \rangle \big\rangle_{(N)} = \langle x \rangle \big\langle \sum_{i=1}^{N} 1 \big\rangle_{(N)} = \langle x \rangle \langle N \rangle, \qquad \text{(C.6)}$$

and

$$\big\langle \big(\sum_{i=1}^{N} x_i \big)^2 \big\rangle = \big\langle \sum_{i=1}^{N} x_i^2 + \sum_{i \neq j}^{N} x_i x_j \big\rangle = \big\langle \sum_{i=1}^{N} x_i^2 \big\rangle + \big\langle \sum_{i \neq j}^{N} x_i x_j \big\rangle. \tag{C.7}$$

Similarly to Eq. (C.6), we have

$$\big\langle \sum_{i=1}^{N} x_i^2 \big\rangle = \langle x^2 \rangle \langle N \rangle, \tag{C.8}$$

and

$$\begin{aligned} \big\langle \sum_{i \neq j}^{N} x_i x_j \big\rangle = \big\langle \sum_{i \neq j}^{N} \langle x_i x_j \rangle \big\rangle_{(N)} = \big\langle \sum_{i \neq j}^{N} \langle x_i \rangle \langle x_j \rangle \big\rangle_{(N)} = \big\langle \sum_{i \neq j}^{N} \langle x \rangle^2 \big\rangle_{(N)} &= \langle x \rangle^2 \big\langle \sum_{i \neq j}^{N} 1 \big\rangle_{(N)} \\ &= \langle x \rangle^2 \langle N^2 - N \rangle \end{aligned} \tag{C.9}$$

Hence, Eq. (C.7) becomes

$$\big\langle \big(\sum_{i=1}^{N} x_i \big)^2 \big\rangle = \langle x^2 \rangle \langle N \rangle + \langle x \rangle^2 \langle N^2 - N \rangle. \tag{C.10}$$

And, we can obtain

$$\sigma_z = \langle x^2 \rangle \langle N \rangle + \langle x \rangle^2 \langle N^2 - N \rangle - \langle x \rangle^2 \langle N \rangle^2 = \langle N \rangle \sigma_x + \langle \mu \rangle^2 \sigma_N, \tag{C.11}$$

and

$$\frac{\sigma_z}{\langle z \rangle^2} = \frac{1}{\langle N \rangle} \frac{\sigma_x}{\langle x \rangle^2} + \frac{\sigma_N}{\langle N \rangle^2}. \tag{C.12}$$

For example, an electrical current

$$I = Nev = Ne\mu E = eE \sum_{i=1}^{N} \mu_i \tag{C.13}$$

will give a current fluctuation of which the power spectrum is

$$\frac{S_I}{\langle I \rangle^2} \propto \frac{(\delta I)^2}{\langle I \rangle^2} = \frac{1}{\langle N \rangle} \frac{(\delta \mu)^2}{\langle \mu \rangle^2} + \frac{(\delta N)^2}{\langle N \rangle^2}. \tag{C.14}$$

Appendix D

Some general calculations for fluctuations in electronic devices

D.1 Relative fluctuations

If a physical quantity x can be expressed by a sum of x_1 and x_2, we have

$$\begin{aligned} x &= x_1 + x_2 \\ \langle x^2 \rangle &= \langle (x_1 + x_2)^2 \rangle \\ &= \langle x_1^2 \rangle + \langle x_2^2 \rangle + 2\langle x_1 x_2 \rangle \qquad \text{(D.1)} \\ \langle x \rangle^2 &= \langle x_1 + x_2 \rangle^2 \\ &= (\langle x_1 \rangle + \langle x_2 \rangle)^2 \\ &= \langle x_1 \rangle^2 + \langle x_2 \rangle^2 + 2\langle x_1 \rangle \langle x_2 \rangle \qquad \text{(D.2)} \end{aligned}$$

By using an assumption of the independence

$$\langle x_1 x_2 \rangle = \langle x_1 \rangle \langle x_2 \rangle, \qquad \text{(D.3)}$$

we have

$$\begin{aligned} S_x &= \langle x^2 \rangle - \langle x \rangle^2 \\ &= (\langle x_1^2 \rangle - \langle x_1 \rangle^2) + (\langle x_2^2 \rangle - \langle x_2 \rangle^2) = S_{x_1}^{(1)} + S_{x_2}^{(2)}, \qquad \text{(D.4)} \end{aligned}$$

or

$$\begin{aligned} \frac{S_x}{\langle x \rangle^2} &= \frac{S_{x_1}^{(1)}}{\langle x \rangle^2} + \frac{S_{x_2}^{(2)}}{\langle x \rangle^2} \\ &= \frac{S_{x_1}^{(1)}}{\langle x_1 \rangle^2} \frac{\langle x_1 \rangle^2}{\langle x \rangle^2} + \frac{S_{x_2}^{(2)}}{\langle x_2 \rangle^2} \frac{\langle x_2 \rangle^2}{\langle x \rangle^2}. \qquad \text{(D.5)} \end{aligned}$$

Applying for $x_1 = x_2 = x/2$

$$\frac{S_x}{\langle x \rangle^2} = \frac{S_{x_1}^{(1)} + S_{x_2}^{(2)}}{\langle x_1 + x_2 \rangle^2} = \frac{2S_{x_1}^{(1)}}{4\langle x_1 \rangle^2} = \frac{S_{x_1}^{(1)}}{2\langle x_1 \rangle^2} \qquad \text{(D.6)}$$

D.2 Correlation between current/voltage and conductance/resistance fluctuations

Current I flowing in a conductor with conductance G or voltage V drop between two ends of a resistor with resistance R does not fluctuate itself, it only reflects the resistance/conductance fluctuations. To measure ideally current fluctuation, we keep the voltage constant, hence

$$\frac{S_I}{\langle I\rangle^2} = \frac{\langle I^2\rangle - \langle I\rangle^2}{\langle I\rangle^2} = \frac{\langle V.G^2\rangle - \langle V.G\rangle^2}{\langle V.G\rangle^2} = \frac{S_G}{\langle G\rangle^2}, \tag{D.7}$$

this means that the fluctuation of the current is actually that of the the conductance.

To measure ideally voltage fluctuation, we keep the current constant, hence

$$\frac{S_V}{\langle V\rangle^2} = \frac{\langle V^2\rangle - \langle V\rangle^2}{\langle V\rangle^2} = \frac{\langle I.R^2\rangle - \langle I.R\rangle^2}{\langle I.R\rangle^2} = \frac{S_R}{\langle R\rangle^2}, \tag{D.8}$$

this means that the fluctuation of the voltage is actually that of the the resistance.

On the other hand, in the case of small fluctuations, i.e.,

$$\delta G \to 0,\ \delta R \to 0, \tag{D.9}$$

we have

$$G = \frac{1}{R} \Rightarrow \ln G = -\ln R \Rightarrow \frac{\delta G}{G} = -\frac{\delta R}{R} \Rightarrow \frac{(\delta G)^2}{G^2} = \frac{(\delta R)^2}{R^2}, \tag{D.10}$$

and

$$\frac{S_V}{\langle V\rangle^2} = \frac{S_I}{\langle I\rangle^2} = \frac{S_R}{\langle R\rangle^2} = \frac{S_G}{\langle G\rangle^2}. \tag{D.11}$$

D.3 Correlation between current and voltage fluctuations

D.3.1 Ohmic regime

For Ohmic regime,

$$\begin{aligned} V &= RI \\ I &= GV, \end{aligned} \tag{D.12}$$

where R and G are resistance and conductance, and the equivalent circuit for current noise source and voltage noise source as in Fig. D.1

We have

$$I = GV \tag{D.13}$$

$$S_I = G^2 S_V = \frac{S_V}{R^2}, \tag{D.14}$$

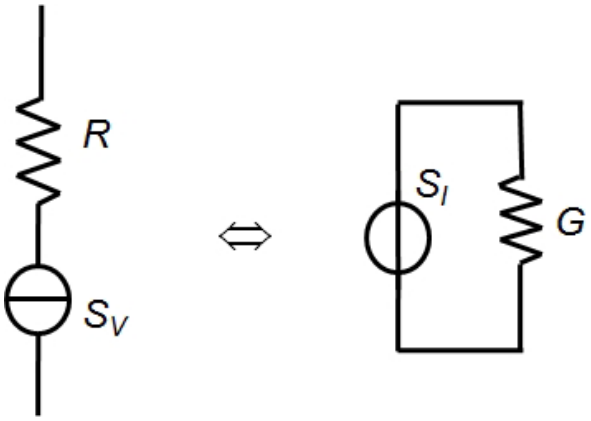

Figure D.1: Equivalent circuit for current noise source and voltage noise source for Ohmic regime

this leads to

$$\frac{S_I}{I^2} = \frac{S_V}{R^2 I^2} = \frac{S_V}{V^2}, \tag{D.15}$$

similar to the Eq. D.11.

For non-Ohmic regime, the equivalent circuit for current noise source and voltage noise source as in Fig. D.2 We have

$$S_I = \left(\frac{\mathrm{d}I}{\mathrm{d}V}\right)^2 S_V, \tag{D.16}$$

this leads to

$$\frac{S_I}{I^2} = \frac{(\mathrm{d}I/\mathrm{d}V)^2 S_V}{I^2}. \tag{D.17}$$

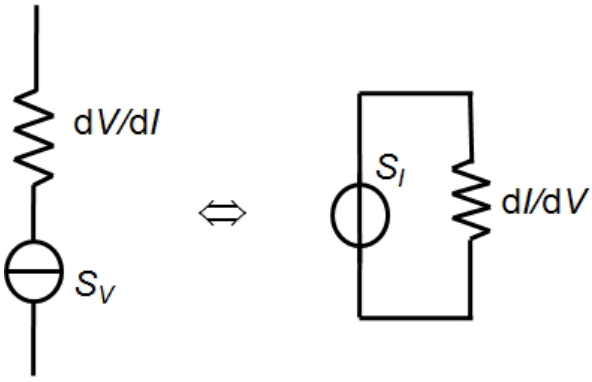

Figure D.2: Equivalent circuit for current noise source and voltage noise source for non-Ohmic regime

In the case of

$$I \propto V^{\beta}, \tag{D.18}$$

leading to

$$\frac{\mathrm{d}I}{\mathrm{d}V} = \beta V^{\beta-1}, \tag{D.19}$$

$$\left(\frac{\mathrm{d}I}{\mathrm{d}V}\right)^2 = \beta^2 V^{2(\beta-1)}. \tag{D.20}$$

We have

$$\frac{(\mathrm{d}I/\mathrm{d}V)^2}{I^2} = \frac{\beta^2}{V^2}, \tag{D.21}$$

leading to

$$\frac{S_I}{I^2} = \frac{(\mathrm{d}I/\mathrm{d}V)^2 S_V}{I^2} = \beta^2 \frac{S_V}{V^2}. \tag{D.22}$$

For $\beta = 1$, Eqs (D.18,D.22) become Eqs (D.12,D.15) for Ohmic regime.

D.4 Size dependence of fluctuations

For conductors in series as in Fig. D.3

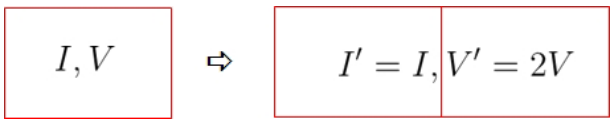

Figure D.3: Conductor with double size in series

From Eq. D.6

$$\begin{aligned} V' = 2V \quad &\Rightarrow \quad \frac{S'_V}{\langle V' \rangle^2} = \frac{S_V}{2\langle V \rangle^2} \\ &\Rightarrow \quad \frac{S'_I}{\langle I' \rangle^2} = \frac{S_I}{2\langle I \rangle^2}. \end{aligned} \tag{D.23}$$

This equation means that although the current following in the device is not changed, the current fluctuation PSD becomes half when the device size is double in series connection.

For conductors in parallel as in Fig. D.4

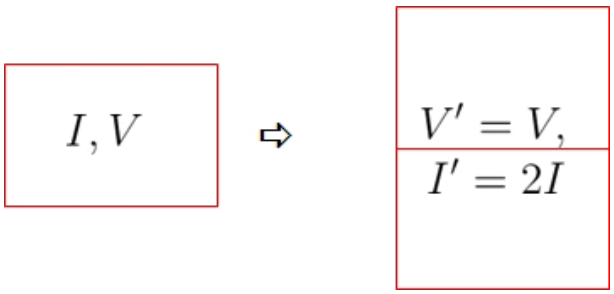

Figure D.4: Conductor with double size in parallel

From Eq. D.6

$$I' = 2I \quad \Rightarrow \quad \frac{S'_I}{\langle I' \rangle^2} = \frac{S_I}{2\langle I \rangle^2} \tag{D.24}$$

$$\Rightarrow \quad \frac{S'_V}{\langle V' \rangle^2} = \frac{S_V}{2\langle V \rangle^2} \tag{D.25}$$

This equation means that although the voltage across the device is not changed, the voltage fluctuation PSD becomes half when the device size is double in parallel connection.

In summary,

$$\frac{S_V}{\langle V \rangle^2} = \frac{S_I}{\langle I \rangle^2} = \frac{S_R}{\langle R \rangle^2} = \frac{S_G}{\langle G \rangle^2} \propto \frac{1}{LW} \propto \frac{1}{N}. \tag{D.26}$$

Appendix E

Fluctuations of occupation probability

E.1 Average probability of the occupation by electrons

The occupation probability of one state is given by the canonical distribution for the state of energy ε

$$P_N = Ce^{-\beta(\varepsilon - N\mu)}, \tag{E.1}$$

where N is particle number in one state, C is a prefactor depending on the normalization, $\beta = 1/k_{\mathrm{B}}T$ with Boltzmann constant k_{B} and temperature T, and μ is chemical potential. Applying this distribution for the case of occupation by one electron $N = 1$ or empty $N = 0$ (according to Pauli exclusion principle),

$$\begin{aligned} P_0 &= Ce^{-\beta\varepsilon} \\ P_1 &= Ce^{-\beta(\varepsilon-\mu)}. \end{aligned} \tag{E.2}$$

The total occupation probability by electrons is

$$\begin{aligned} P_0 + P_1 &= Ce^{-\beta\varepsilon} + Ce^{-\beta(\varepsilon-\mu)} \\ &= 1 \text{ for normalization,} \end{aligned} \tag{E.3}$$

leading to

$$\begin{aligned} C &= \frac{1}{1 + e^{-\beta(\varepsilon-\mu)}} \\ P_1 &= Ce^{-\beta(\varepsilon-\mu)} = \frac{1}{1 + e^{-\beta(\varepsilon-\mu)}} e^{-\beta(\varepsilon-\mu)} = \frac{1}{1 + e^{\beta(\varepsilon-\mu)}}, \end{aligned} \tag{E.4}$$

P_1 is Fermi-Dirac distribution with μ in the meaning of Fermi level, from now we get P instead of P_1 for convenience. Average of the occupation probability or average electron number n in one state

$$\langle n \rangle = P_0 \cdot 0 + P_1 \cdot 1 = \frac{1}{1 + e^{\beta(\varepsilon-\mu)}} = P \tag{E.5}$$

$$\langle n^2 \rangle = P_0 \cdot 0^2 + P_1 \cdot 1^2 = P, \tag{E.6}$$

E.2 Probability fluctuation of the occupation by electrons

The fluctuation of the occupation probability of one state is determined by Eqs. E.5

$$(\delta n)^2 = \langle (n - \langle n \rangle)^2 \rangle = \langle n^2 \rangle - \langle n \rangle^2 = P - P^2 = P(1-P) \tag{E.7}$$

For many states with density D_i, we have to take integration for all over energy levels to obtain the fluctuation of the occupation probability of all states

$$(\delta N)^2 = LW \int (\delta n)^2 D_\mathrm{i} \mathrm{d}\varepsilon = LW \int P(1-P) D_\mathrm{i} \mathrm{d}\varepsilon. \tag{E.8}$$

We have

$$\frac{\partial P}{\partial \varepsilon} = \frac{\partial}{\partial \varepsilon}\left(\frac{1}{1+e^{\beta(\varepsilon-\mu)}}\right) = -\beta \frac{e^{\beta(\varepsilon-\mu)}}{(1+e^{\beta(\varepsilon-\mu)})^2} \tag{E.9}$$

$$= -\beta P(1-P), \tag{E.10}$$

$P(1-P)$ behaves like a delta function around Fermi level, leading to

$$\int P(1-P) D_\mathrm{i} \mathrm{d}\varepsilon \simeq D_\mathrm{i} \int P(1-P) \mathrm{d}\varepsilon \tag{E.11}$$

$$= -D_\mathrm{i} \frac{1}{\beta} \int_{-\infty}^{+\infty} \frac{\partial P}{\partial \varepsilon} \mathrm{d}\varepsilon = D_\mathrm{i} k_\mathrm{B} T. \tag{E.12}$$

Hence

$$(\delta N)^2 = LW D_\mathrm{i} k_\mathrm{B} T. \tag{E.13}$$

Publications

[1] H. Takita, C. T. Nguyen, S. P. Le, M. Akabori and T. Suzuki: "Electron accumulation and carrier recombination at surfaces and interfaces in InAs thin films bonded on low-k flexible substrates", 2011 Topical Workshop on Heterostructure Microelectronics, Gifu, Japan, August 28-31 (2011).

[2] S. P. Le, M. Akabori and T. Suzuki: "Electron mobility anisotropy in InAs thin films on GaAs(001)", The International Seminar on Emerging Nanotechnologies for "More than Moore" and "Beyond CMOS" Era, JAIST, Japan, March 26-29 (2012).

[3] S. P. Le, M. Akabori and T. Suzuki: "Electron mobility anisotropy in InAs/GaAs(001)", The seventeenth International Conference on Molecular Beam Epitaxy, Nara, Japan, September 23-28 (2012).

[4] S. P. Le, T. Q. Nguyen, H.-A. Shih, M. Kudo and T. Suzuki: "Low-frequency noise of intrinsic gated region in AlN/AlGaN/GaN metal-insulator-semiconductor heterojunction field-effect transistors", 46th International Conference on Solid State Devices and Materials, Tsukuba, Japan, September 8-11 (2014).

[5] S. P. Le, T. Q. Nguyen, H.-A. Shih, M. Kudo and T. Suzuki: "Low-frequency noise in AlN/AlGaN/GaN metal-insulator-semiconductor devices: a comparison with Schottky devices", Journal of Applied Physics **116** (2014) 054510.

Bibliography

[1] S. M. Sze and K. K. Ng, *Physics of Semiconductor Devices*. John Wiley & Sons Inc., 2007.

[2] G. E. Moore, "Cramming more components onto integrated circuits," *Electronics*, vol. 8, pp. 114–117, 1965.

[3] I. Ferain, C. A. Colinge, and J.-P. Colinge, "Multigate transistors as the future of classical metal-oxide-semiconductor field-effect transistors," *Nature*, vol. 479, pp. 310–316, 2011.

[4] *International Technology Roadmap for Semiconductors (ITRS), Executive summary*. 2011.

[5] W. Arden, M. Brillouët, P. Cogez, M. Graef, B. Huizing, and R. Mahnkopf, *More than Moore*. http://www.itrs.net/Links/2010ITRS/IRC-ITRS-MtM-v2%203.pdf.

[6] C. A. Mead, "Schottky barrier gate field effect transistor," *Proceedings of the IEEE*, vol. 54, no. 2, pp. 307–308, 1966.

[7] T. Mimura, S. Hiyamizu, T. Fujii, and K. Nanbu, "A new field-effect transistor with selectively doped gaas/n-al$_x$ga$_{1-x}$as heterojunctions," *Jpn. J. Appl. Phys.*, vol. 19, no. 5, p. L225, 1980.

[8] H. Kroemer, "Theory of a wide-gap emitter for transistors," *Proceedings of the IRE*, vol. 45, no. 11, pp. 1535–1537, 1957.

[9] R. N. Hall, G. E. Fenner, J. D. Kingsley, T. J. Soltys, and R. O. Carlson, "Coherent light emission from gaas junctions," *Phys. Rev. Lett.*, vol. 9, pp. 366–368, 1962.

[10] G. Burns and M. Nathan, "P-n junction lasers," *Proceedings of the IRE*, vol. 52, no. 2, p. 770, 1960.

[11] J. I. Pankove, "Tunneling-assisted photon emission in gallium arsenide pn junctions," *Phys. Rev. Lett.*, vol. 9, pp. 283–285, 1962.

[12] H. Kroemer, "Solid state radiation emitters," *US Patent*, vol. 3, no. 2, p. 309, 1967.

[13] I. Vurgaftman, J. R. Meyer, and L. R. Ram-Mohan, "Band parameters for iii?v compound semiconductors and their alloys," *J. Appl. Phys.*, vol. 89, no. 11, pp. 5815–5875, 2001.

[14] I. Vurgaftman and J. R. Meyer, "Band parameters for nitrogen-containing semiconductors," *J. Appl. Phys.*, vol. 94, no. 6, pp. 3675–3696, 2003.

[15] Y. Jeong, M. Shindo, M. Akabori, and T. kazu Suzuki, "Epitaxial lift-off of ingaas/inalas metamorphic high electron mobility heterostructures and their van der waals bonding on aln ceramic substrates," *Appl. Phys. Express*, vol. 1, no. 2, p. 021201, 2008.

[16] S. Kogan, *Electronic noise and fluctuations in solids.* Cambridge University Press, 1996.

[17] F. N. Hooge, "1/f Noise Sources," *IEEE Trans. Electron Devices*, vol. 41, no. 11 Part 1, pp. 1926–1935, 1994.

[18] H. Wong, "Low-frequency noise study in electron devices: review and update," *Microelectron. Reliab.*, vol. 43, no. 4, pp. 585–599, 2003.

[19] J. B. Johnson, "Thermal agitation of electricity in conductors," *Phys. Rev.*, vol. 32, pp. 97–109, 1928.

[20] H. Nyquist, "Thermal agitation of electric charge in conductors," *Phys. Rev.*, vol. 32, pp. 110–113, 1928.

[21] P. Dutta and P. M. Horn, "Low-frequency fluctuations in solids: 1f noise," *Rev. Mod. Phys.*, vol. 53, pp. 497–516, 1981.

[22] M. B. Weissman, "1f noise and other slow, nonexponential kinetics in condensed matter," *Rev. Mod. Phys.*, vol. 60, pp. 537–571, 1988.

[23] L. K. J. Vandamme, X. Li, and D. Rigaud, "1/f Noise in MOS Devices: Mobility or Number Fluctuations?," *IEEE Trans. Electron Devices*, vol. 41, no. 11 Part 1, pp. 1936–1945, 1994.

[24] J. B. Johnson, "The schottky effect in low frequency circuits," *Phys. Rev.*, vol. 26, pp. 71–85, 1925.

[25] W. Schottky, "Small-shot effect and flicker effect," *Phys. Rev.*, vol. 28, pp. 74–103, 1926.

[26] L. Vandamme and F. N. Hooge, "What do we certainly know about 1/f noise in mosts?," *IEEE Trans. Electron Devices*, vol. 55, no. 11, pp. 3070–3085, 2008.

[27] M. J. Deen and O. Marinov, "Noise in advanced electronic devices and circuits," *Proc. Int. Conf. Noise and Fluctuations (ICNF)*, pp. 3–12, 2005.

[28] M. J. Deen and O. Marinov, "Noise in advanced electronic devices and circuits," in *AIP Conf. Proc.*, vol. 780, p. 3, 2005.

[29] L. Kish and C. Granqvist, "Noise in nanotechnology," *Microelectron. Reliab.*, vol. 40, no. 11, pp. 1833–1837, 2000.

[30] L. Vandamme, "Noise as a diagnostic tool for quality and reliability of electronic devices," *IEEE Trans. Electron Devices*, vol. 41, no. 11, pp. 2176–2187, 1994.

[31] R. Landauer, "The noise is the signal," *Nature*, vol. 392, pp. 658–659, 1998.

[32] F. Hooge, "1/f noise is no surface effect," *Physics Letters A*, vol. 29, no. 3, pp. 139–140, 1969.

[33] F. N. Hooge, T. G. M. Kleinpenning, and L. K. J. Vandamme, "Experimental studies on 1/f noise," *Rep. Prog. Phys.*, vol. 44, no. 5, pp. 479–532, 1981.

[34] A. L. McWhorter, *Semiconductor Surface Physics, Edited by R. H. Kingston.* Univ. of Pennsylvania Press, 1956.

[35] F. Hooge, "On the additivity of generation-recombination spectra. part 2: 1/f noise," *Physica B*, vol. 336, no. 3-4, pp. 236–251, 2003.

[36] R. F. Voss and J. Clarke, "Flicker $(1/f)$ noise: Equilibrium temperature and resistance fluctuations," *Phys. Rev. B*, vol. 13, pp. 556–573, 1976.

[37] P. Dutta, P. Dimon, and P. M. Horn, "Energy scales for noise processes in metals," *Phys. Rev. Lett.*, vol. 43, pp. 646–649, 1979.

[38] P. H. Handel, "Quantum approach to 1f noise," *Phys. Rev. A*, vol. 22, pp. 745–757, 1980.

[39] A. U. MacRae, "1/f noise from vacuum-cleaned silicon," *J. Appl. Phys.*, vol. 33, no. 8, 1962.

[40] M. J. Deen, S. Rumyantsev, and J. Orchard-Webb, "Low frequency noise in heavily doped polysilicon thin film resistors," *J. Vac. Sci. Technol., B*, vol. 16, no. 4, pp. 1881–1884, 1998.

[41] B.-H. Leung, W.-K. Fong, C.-F. Zhu, and C. Surya, "Study of low-frequency excess noise in gan thin films deposited by rf-mbe on intermediate-temperature buffer layers," *IEEE Trans. Electron Devices*, vol. 48, no. 10, pp. 2400–2404, 2001.

[42] N. Pala, S. Rumyantsev, R. Gaska, M. Shur, J. Yang, X. Hu, G. Simin, and M. Khan, "Low frequency noise in al0.4ga0.6n thin films," in *High Performance Devices, 2002. Proceedings. IEEE Lester Eastman Conference on*, pp. 164–171, 2002.

[43] C.-T. Sah, R. Noyce, and W. Shockley, "Carrier generation and recombination in p-n junctions and p-n junction characteristics," *Proceedings of the IRE*, vol. 45, pp. 1228–1243, Sept 1957.

[44] C. T. Sah and F. H. Hielscher, "Evidence of the surface origin of the 1f noise," *Phys. Rev. Lett.*, vol. 17, pp. 956–958, 1966.

[45] F. Klaassen, "Characterization of low 1/f noise in mos transistors," *IEEE Trans. Electron Devices*, vol. 18, no. 10, pp. 887–891, 1971.

[46] G. Ghibaudo, O. Roux-dit Buisson, and J. Brini, "Impact of scaling down on low frequency noise in silicon mos transistors," *Physica status solidi a*, vol. 132, no. 2, pp. 501–507, 1992.

[47] J. Zhuge, R. Wang, R. Huang, Y. Tian, L. Zhang, D.-W. Kim, D. Park, and Y. Wang, "Investigation of low-frequency noise in silicon nanowire mosfets," *IEEE Electron Device Lett.*, vol. 30, no. 1, pp. 57–60, 2009.

[48] I. Flinn, G. Bew, and F. Berz, "Low frequency noise in mos field effect transistors," *Solid-State Electron.*, vol. 10, no. 8, pp. 833–845, 1967.

[49] J. Chang, A. Abidi, and C. Viswanathan, "Flicker noise in cmos transistors from subthreshold to strong inversion at various temperatures," *IEEE Trans. Electron Devices*, vol. 41, no. 11, pp. 1965–1971, 1994.

[50] S. Christensson, I. Lundstrom, and C. Svensson, "Low frequency noise in {MOS} transistors: I-theory," *Solid-State Electronics*, vol. 11, no. 9, pp. 797–812, 1968.

[51] S.-Y. Wu, "Theory of the generation-recombination noise in mos transistors," *Solid-State Electron.*, vol. 11, no. 1, pp. 25–32, 1968.

[52] F. Berz, "Theory of low frequency noise in si most's," *Solid-State Electron.*, vol. 13, no. 5, pp. 631–647, 1970.

[53] S. Hsu, "Surface state related $1/f$ noise in {MOS} transistors," *Solid-State Electron.*, vol. 13, no. 11, pp. 1451–1459, 1970.

[54] P. H. Handel, "Nature of 1f phase noise," *Phys. Rev. Lett.*, vol. 34, pp. 1495–1498, 1975.

[55] S. Christensson and I. Lundstrom, "Low frequency noise in {MOS} transistors: Ii-experiments," *Solid-State Electronics*, vol. 11, no. 9, pp. 813–820, 1968.

[56] E. Simoen, A. Mercha, C. Claeys, and N. Lukyanchikova, "Low-frequency noise in silicon-on-insulator devices and technologies," *Solid-State Electron.*, vol. 51, no. 1, pp. 16–37, 2007.

[57] S. Villa, G. D. Geronimo, A. Pacelli, A. Lacaita, and A. Longoni, "Application of 1/f noise measurements to the characterization of near-interface oxide traps in {ULSI} n-mosfets," *Microelectron. Reliab.*, vol. 38, no. 12, pp. 1919 – 1923, 1998.

[58] N. V. Amarasinghe, Z. Celik-Butler, and P. Vasina, "Characterization of oxide traps in 0.15 m2 {MOSFETs} using random telegraph signals," *Microelectron. Reliab.*, vol. 40, no. 11, pp. 1875 – 1881, 2000.

[59] L. Vandamme, "Bulk and surface 1/f noise," *IEEE Trans. Electron Devices*, vol. 36, no. 5, pp. 987–992, 1989.

[60] C. Surya and T. Y. Hsiang, "Theory and experiment on the $1/f\gamma$ noise in p-channel metal-oxide-semiconductor field-effect transistors at low drain bias," *Phys. Rev. B*, vol. 33, pp. 4898–4905, 1986.

[61] C. Surya and T. Y. Hsiang, "Surface mobility fluctuations in metal-oxide-semiconductor field-effect transistors," *Phys. Rev. B*, vol. 35, pp. 6343–6347, 1987.

[62] L. Freeman and W. Dahlke, "Theory of tunneling into interface states," *Solid-State Electron.*, vol. 13, no. 11, pp. 1483–1503, 1970.

[63] O. Jantsch, "Flicker (1/f) noise generated by a random walk of electrons in interfaces," *IEEE Trans. Electron Devices*, vol. 34, no. 5, pp. 1100–1115, 1987.

[64] L. Vandamme and F. Hooge, "On the additivity of generation-recombination spectra part 3: The mcwhorter model for 1/f noise in mosfets," *Physica B*, vol. 357, no. 3-4, pp. 507–524, 2005.

[65] M. Tacano, M. Ando, I. Shibasaki, S. Hashiguchi, J. Sikula, and T. Matsui, "Dependence of hooge parameter of inas heterostructure on temperature," *Microelectron. Reliab.*, vol. 40, no. 11, pp. 1921 – 1924, 2000.

[66] W. Kruppa, M. J. Yang, B. R. Bennett, and J. B. Boos, "Low-frequency noise in alsb/inas high-electron-mobility transistor structure as a function of temperature and illumination," *Appl. Phys. Lett.*, vol. 85, pp. 774–776, 2004.

[67] W. Kruppa, J. Boos, B. Bennett, N. Papanicolaou, D. Park, and R. Bass, "Low-frequency noise in alsb/inas and related hemts," *IEEE Trans. Electron Devices*, vol. 54, no. 5, pp. 1193–1202, 2007.

[68] R. Rupani, S. Ghosh, X. Su, and P. Bhattacharya, "Low frequency noise spectroscopy in inas/gaas resonant tunneling quantum dot infrared photodetectors," *Microelectronics Journal*, vol. 39, no. 3?4, pp. 307 – 313, 2008. The Sixth International Conference on Low Dimensional Structures and Devices LDSD'07.

[69] M. R. Sakr and X. P. A. Gao, "Temperature dependence of the low frequency noise in indium arsenide nanowire transistors," *Appl. Phys. Lett.*, vol. 93, no. 20, p. 203503, 2008.

[70] K.-M. Persson, E. Lind, A. Dey, C. Thelander, H. Sjoland, and L. E. Wernersson, "Low-frequency noise in vertical inas nanowire fets," *IEEE Electron Device Lett.*, vol. 31, no. 5, pp. 428–430, 2010.

[71] H. Takita, N. Hashimoto, C. T. Nguyen, M. Kudo, M. Akabori, and T. Suzuki, "Electron transport properties of inas ultrathin films obtained by epitaxial lift-off and van der waals bonding on flexible substrates," *Appl. Phys. Lett.*, vol. 97, no. 1, p. 012102, 2010.

[72] Y. Jeong, M. Shindo, M. Akabori, and T. Suzuki, "Epitaxial lift-off of InGaAs/InAlAs metamorphic high electron mobility heterostructures and their van der Waals bonding on AlN ceramic substrates," *Appl. Phys. Express*, vol. 1, no. 2, pp. 021201–1–3, 2008.

[73] M. E. Levinshtein, F. Pascal, S. Contreras, W. Knap, S. L. Rumyantsev, R. Gaska, J. W. Yang, and M. Shur, "Low-frequency noise in gan/gaaln heterojunctions," *Appl. Phys. Lett.*, vol. 72, no. 23, pp. 3053–3055, 1998.

[74] M. E. Levinshtein, S. L. Rumyantsev, R. Gaska, J. W. Yang, and M. S. Shur, "Algan/gan high electron mobility field effect transistors with low 1/f noise," *Appl. Phys. Lett.*, vol. 73, no. 8, pp. 1089–1091, 1998.

[75] D. Kuksenkov, H. Temkin, R. Gaska, and J. Yang, "Low-frequency noise in algan/gan heterostructure field effect transistors," *IEEE Electron Device Lett.*, vol. 19, no. 7, pp. 222–224, 1998.

[76] W. Y. Ho, C. Surya, K. Y. Tong, W. Kim, A. Botcharev, and H. Morkoc, "Characterization of flicker noise in gan-based modfet's at low drain bias," *IEEE Trans. Electron Devices*, vol. 46, no. 6, pp. 1099–1104, 1999.

[77] M. E. Levinshtein, S. L. Rumyantsev, D. C. Look, R. J. Molnar, M. A. Khan, G. Simin, V. Adivarahan, and M. S. Shur, "Low-frequency noise in n-gan with high electron mobility," *J. Appl. Phys.*, vol. 86, no. 9, pp. 5075–5078, 1999.

[78] A. Balandin, S. Morozov, G. Wijeratne, S. J. Cai, R. Li, J. Li, K. L. Wang, C. R. Viswanathan, and Y. Dubrovskii, "Effect of channel doping on the low-frequency noise in gan/algan heterostructure field-effect transistors," *Appl. Phys. Lett.*, vol. 75, no. 14, pp. 2064–2066, 1999.

[79] J. A. Garrido, B. E. Foutz, J. A. Smart, J. R. Shealy, M. J. Murphy, W. J. Schaff, L. F. Eastman, and E. Muoz, "Low-frequency noise and mobility fluctuations in algan/gan heterostructure field-effect transistors," *Appl. Phys. Lett.*, vol. 76, no. 23, pp. 3442–3444, 2000.

[80] S. L. Rumyantsev, N. Pala, M. S. Shur, R. Gaska, M. E. Levinshtein, P. A. Ivanov, M. A. Khan, G. Simin, X. Hu, and J. Yang, "Concentration dependence of the 1/ f noise in algan/gan heterostructure field effect transistors," *Semicond. Sci. Technol.*, vol. 17, no. 5, p. 476, 2002.

[81] S. A. Vitusevich, S. V. Danylyuk, N. Klein, M. V. Petrychuk, V. N. Sokolov, V. A. Kochelap, A. E. Belyaev, V. Tilak, J. Smart, A. Vertiatchikh, and L. F. Eastman, "Excess low-frequency noise in algan/gan-based high-electron-mobility transistors," *Appl. Phys. Lett.*, vol. 80, no. 12, pp. 2126–2128, 2002.

[82] A. Vertiatchikh and L. F. Eastman, "Effect of the surface and barrier defects on the algan/gan hemt low-frequency noise performance," *IEEE Electron Device Lett.*, vol. 24, no. 9, pp. 535–537, 2003.

[83] N. Pala, S. Rumyantsev, M. Shur, R. Gaska, X. Hu, J. Yang, G. Simin, and M. Khan, "Low frequency noise in algan/ingan/gan double heterostructure field effect transistors," *Solid-State Electron.*, vol. 47, no. 6, pp. 1099 – 1104, 2003.

[84] S. L. Rumyantsev, N. Pala, M. S. Shur, M. E. Levinshtein, M. Asif Khan, G. Simin, and J. Yang, "Low frequency noise in gan/algan heterostructure field effect transistors in non-ohmic region," *J. Appl. Phys.*, vol. 93, no. 12, 2003.

[85] S. L. Rumyantsev, M. S. Shur, N. Dyakonova, W. Knap, Y. Meziani, F. Pascal, A. Hoffman, X. Hu, Q. Fareed, Y. Bilenko, and R. Gaska, "1?f noise in gan?algan heterostructure field-effect transistors in high magnetic fields at 300k," *J. Appl. Phys.*, vol. 96, no. 7, pp. 3845–3847, 2004.

[86] A. P. Dmitriev, M. E. Levinshtein, S. L. Rumyantsev, and M. S. Shur, "Tunneling mechanism of the 1?f noise in gan?algan heterojunction field-effect transistors," *J. Appl. Phys.*, vol. 97, no. 12, pp. –, 2005.

[87] H. Rao and G. Bosman, "Simultaneous low-frequency noise characterization of gate and drain currents in algan/gan high electron mobility transistors," *J. Appl. Phys.*, vol. 106, no. 10, pp. –, 2009.

[88] C. Kayis, C. Y. Zhu, M. Wu, X. Li, U. Ozgur, and H. Morkoc, "Field-assisted emission in algan/gan heterostructure field-effect transistors using low-frequency noise technique," *J. Appl. Phys.*, vol. 109, no. 8, pp. –, 2011.

[89] T. Roy, Y. S. Puzyrev, E. X. Zhang, S. DasGupta, S. A. Francis, D. M. Fleetwood, R. D. Schrimpf, U. K. Mishra, J. S. Speck, and S. T. Pantelides, "1/f noise in gan {HEMTs} grown under ga-rich, n-rich, and nh3-rich conditions," *Microelectron. Reliab.*, vol. 51, no. 2, pp. 212 – 216, 2011. 2010 Reliability of Compound Semiconductors (ROCS) Workshop Prognostics and Health Management.

[90] H.-C. Chiu, C.-H. Chen, H.-L. Kao, F.-T. Chien, P.-K. Weng, Y.-T. Gau, and H.-W. Chuang, "Sidewall defects of algan/gan {HEMTs} evaluated by low frequency noise analysis," *Microelectron. Reliab.*, vol. 53, no. 12, pp. 1897 – 1900, 2013.

[91] N. Pala, R. Gaska, S. Rumyantsev, M. Shur, M. A. Khan, X. Hu, G. Simin, and J. Yang, "Low-frequency noise in algan/gan mos-hfets," *Electron. Lett.*, vol. 36, no. 3, pp. 268–270, 2000.

[92] S. L. Rumyantsev, N. Pala, M. S. Shur, R. Gaska, M. E. Levinshtein, M. A. Khan, G. Simin, X. Hu, and J. Yang, "Effect of gate leakage current on noise properties of algan/gan field effect transistors," *J. Appl. Phys.*, vol. 88, no. 11, pp. 6726–6730, 2000.

[93] S. L. Rumyantsev, N. Pala, M. S. Shur, R. Gaska, M. E. Levinshtein, M. A. Khan, G. Simin, X. Hu, and J. Yang, "Low frequency noise in gan metal semiconductor and metal oxide semiconductor field effect transistors," *J. Appl. Phys.*, vol. 90, no. 1, pp. 310–314, 2001.

[94] P. Valizadeh, D. Pavlidis, K. Shiojima, T. Makimura, and N. Shigekawa, "Low frequency noise of algan/gan modfets: A comparative study of surface, barrier and heterointerface effects," *Solid-State Electron.*, vol. 49, no. 8, pp. 1352 – 1360, 2005.

[95] Y.-Z. Chiou, Y.-K. Su, J. Gong, S.-J. Chang, and C.-K. Wang, "Noise analysis of nitride-based metal–oxide–semiconductor heterostructure field effect transistors with photo-chemical vapor deposition sio_2 gate oxide in the linear and saturation regions," *Jpn. J. Appl. Phys.*, vol. 45, no. 4B, pp. 3405–3409, 2006.

[96] L.-H. Huang, S.-H. Yeh, and C.-T. Lee, "High frequency and low frequency noise of algan/gan metal-oxide-semiconductor high-electron mobility transistors with gate insulator grown using photoelectrochemical oxidation method," *Appl. Phys. Lett.*, vol. 93, no. 4, pp. –, 2008.

[97] C. Kayis, J. H. Leach, C. Zhu, M. Wu, X. Li, U. Özgür, H. Morkoc, X. Yang, V. Misra, and P. Handel, "Low-frequency noise measurements of algan/gan metal-oxide-semiconductor heterostructure field-effect transistors with hfalo gate dielectric," *IEEE Electron Device Lett.*, vol. 31, pp. 1041–1043, Sept 2010.

[98] Y.-L. Chiou, C.-S. Lee, and C.-T. Lee, "Algan/gan metal-oxide-semiconductor high-electron mobility transistors with zno gate layer and (nh4)2sx surface treatment," *Appl. Phys. Lett.*, vol. 97, no. 3, p. 032107, 2010.

[99] C.-T. Lee, Y.-L. Chiou, and C.-S. Lee, "Algan/gan mos-hemts with gate zno dielectric layer," *IEEE Electron Device Lett.*, vol. 31, no. 11, pp. 1220–1223, 2010.

[100] C.-T. Lee, L.-H. Huang, and Y.-L. Chiou, "Flicker noises of algan/gan metal-oxide-semiconductor high electron mobility transistors," *Journal of The Electrochemical Society*, vol. 157, no. 7, pp. H734–H738, 2010.

[101] M. Ochiai, M. Akita, Y. Ohno, S. Kishimoto, K. Maezawa, and T. Mizutani, "Algan/gan heterostructure metal-insulator-semiconductor high-electron-mobility transistors with si_3n_4 gate insulator," *Jpn. J. Appl. Phys.*, vol. 42, no. Part 1, No. 4B, pp. 2278–2280, 2003.

[102] M. Khan, A. Bhattarai, J. Kuznia, and D. Olson, "High electron mobility transistor based on a GaN-AlGaN heterojunction," *Appl. Phys. Lett.*, vol. 63, p. 1214, 1993.

[103] F. Korndörfer, "1/f noise measurements," *MOS-AK Meeting*, vol. No. 11284, 2007.

[104] C. T. Nguyen, H.-A. Shih, M. Akabori, and T. Suzuki, "Electron distribution and scattering in inas films on low-k flexible substrates," *Appl. Phys. Lett.*, vol. 100, no. 23, p. 232103, 2012.

[105] R. E. Burgess, "Some topics in the fluctuations of photo-processes in solids," *J. Phys. Chem. Solids*, vol. 22, no. 11 Part 1, pp. 371–377, 1961.

[106] H.-A. Shih, M. Kudo, M. Akabori, and T. Suzuki, "Application of sputtering-deposited aln films to gate dielectric for algan/gan metal–insulator–semiconductor heterojunction field-effect transistor," *Jpn. J. Appl. Phys.*, vol. 51, no. 2, p. 02BF01, 2012.

[107] H.-A. Shih, M. Kudo, and T. Suzuki, "Analysis of aln/algan/gan metal-insulator-semiconductor structure by using capacitance-frequency-temperature mapping," *Appl. Phys. Lett.*, vol. 101, no. 4, p. 043501, 2012.

[108] X. Qin, A. Lucero, A. Azcatl, J. Kim, and R. M. Wallace, "In situ x-ray photoelectron spectroscopy and capacitance voltage characterization of plasma treatments for al2o3/algan/gan stacks," *Appl. Phys. Lett.*, vol. 105, no. 1, p. 011602, 2014.